Technische Universität München
Chemie Department
Lehrstuhl für Physikalische Chemie I

Reactivity and dynamics of monodisperse Pd clusters on a periodically wettable boron nitride substrate

Fabian Leonhard Knoller

Vollständiger Abdruck der von der Fakultät für Chemie der Technischen Universität München zur Erlangung des akademischen Grades eines

Doktors der Naturwissenschaften

genehmigten Dissertation.

Vorsitzender: Univ.-Prof. Dr. Ulrich K. Heiz

Prüfer der Dissertation:
1. Priv.-Doz. Dr. Friedrich Esch
2. Univ.-Prof. Dr. Klaus Köhler

Die Dissertation wurde am 11.04.2018 bei der Technischen Universität München eingereicht und durch die Fakultät für Chemie am 07.05.2018 angenommen.

Contents

List of Figures

List of Tables

List of Abbreviations

AES	Auger electron spectrometer
AFM	atomic force microscopy
bw	backward
CEM	channel electron multiplier
CVD	chemical vapor deposition
d	downward
DFT	density functional theory
FAST	fast acquisition of SPM timeseries
fcc	face centered cubic
FFT	fast Fourier transformation
FPGA	field programmable gate array
fw	forward
GUI	graphical user interface
h-BN	hexagonal boron nitride
hcp	hexagonal closed packed
HOPG	highly ordered pyrolytic graphite
LDOS	local density of states
LEED	low energy electron diffraction
MD	molecular dynamics
m/z	mass to charge ratio
NRA	nuclear reaction analysis
PBN	pyrolytic boron nitride
PID	proportional-integral-derivative
STM	scanning tunneling microscopy
S/N	signal to noise ratio
TTL	transistor-transistor logic
TPD	temperature programmed desorption
UHV	ultra-high vacuum
u	upward
XPS	X-ray photoelectron spectroscopy

Abstract

For a comprehensive description of heterogeneously catalyzed processes, the reactivity of supported nanoparticles has to be linked with the specific dynamics – from reactant activation and spillover to diffusion and sintering of active particles. In this work, a supported model catalyst with truly monodisperse clusters is investigated on the integral and local scale. A corrugated monolayer of hexagonal boron nitride (h-BN) on a Rh(111) single crystal serves as a confining support, suppressing ripening of the Pd clusters.

Integral thermal desorption measurements are applied to study catalytic reactivity. For this purpose a highly sensitive temperature programmed desorption setup is implemented and characterized. Initial results on carbon monoxide oxidation and ethene hydrogenation activity are presented, which are complemented by scanning tunneling microscopy (STM) studies. Sintering sets in from 500 K on, however the ripening behaviour is independent of the presence of the reactants.

Local structural dynamics of Pd clusters and atoms are then examined under reaction conditions with enhanced time resolution. Therefore, a commercial variable temperature STM is equipped with a newly developed add-on instrument, reaching imaging rates of up to 8 frames/s. The fast acquisition of STM timeseries (FAST) reveals specific motions of Pd particles within the h-BN/Rh(111) moiré troughs. A small Pd cluster appears to diffuse between six distinct sites within the trough with sixfold symmetry, 2.5 Å lateral distances and two distinct hopping rates. Pd atoms, protected from ripening by deposition by cooling to 118 K, reveal a circular motion upon heating up to 168 K that can be resolved only by FAST measurements, which appears as ring-like structures in conventional, slow STM images.

Altogether, a platform for fundamental studies of size-selected, supported model catalysts could be established that links catalytic activity with fast local structural dynamics.

Kurzzusammenfassung

Für eine umfassende Beschreibung heterogen katalysierter Prozesse muss die Reaktivität von geträgerten Nanopartikeln mit einhergehenden Dynamiken verknüpft werden – von der Aktivierung und dem Spillover der Reaktanden bis hin zu Diffusion und Sintern der aktiven Partikel. In dieser Arbeit wird ein Modellsystem mit vollkommen größenselektierten Clustern auf integraler und lokaler Ebene untersucht. Als Trägermaterial dient ein gewellter, monoatomarer Film aus hexagonalem Bornitrid (h-BN) auf einem Rh(111) Einkristall, welcher Reifungsprozesse der Pd Cluster unterdrückt.

Die katalytische Reaktivität der Nanopartikel wird mit integralen, thermischen Desorptionsmessungen untersucht. In diesem Zusammenhang wird ein hochempfindlicher Messaufbau zur Temperatur-programmierten Desorption implementiert und charakterisiert. Erste Ergebnisse zur Oxidation von Kohlenstoffmonooxid und der Aktivierung von Kohlenwasserstoffen werden zusammen mit Studien am Rastertunnelmikroskop (STM) präsentiert. Die Nanopartikel sintern bereits ab 500 K, jedoch ist das Reifungsverhalten unabhängig von der Präsenz der Reaktanden.

Lokale, strukturelle Dynamiken von Pd Clustern und Atomen werden unter Reaktionsbedingungen mit erhöhter Zeitauflösung untersucht. Zu diesem Zweck wird ein kommerzielles STM mit einem neu entwickelten Instrument erweitert, welches Bildraten von bis zu 8 Bildern pro Sekunde ermöglicht. Durch die schnelle Aufnahme von STM Zeitserien (FAST) können spezifische Bewegungsmuster von Pd Partikeln innerhalb der h-BN/Rh(111) Mulden untersucht werden. Ein kleiner Pd Nanopartikel diffundiert innerhalb einer Bornitrid Mulde zwischen sechs Stellen mit hexagonaler Symmetry, mit lateralen Abständen von 2.5 Å und zwei unterscheidbaren Hüpfraten. Pd Atome, welche durch kühlen auf 118 K während der Deposition vom Sintern abgehalten werden, zeigen eine kreisförmige Bewegung ab 168 K, die nur mit FAST Messungen aufgelöst werden kann. In konventionellen, langsamen STM Messungen werden diese als Ringe wahrgenommen.

Diese Arbeit schafft Rahmenbedingungen für Grundlagenstudien, in welchen die katalytische Aktivität von geträgerten, größenselektierten Clustern mit lokalen Messungen zu Strukturveränderungen und Diffusionsverhalten verknüpft werden kann.

1. Introduction

Prospective environmental impacts and anticipated patterns of future energy use make sustainable development indispensable [1]. Catalysis plays a key role when it comes to the chemical industry, where approximately 85-90% of the products are made by catalytic processes [2]. The science and technology to increase the rates of chemical reactions is therefore an important research field. A catalyst changes the path of a chemical reaction to milder conditions without being expended and may allow to control the selectivity [3]. This field is divided into homogeneous catalysis, where the reacting molecules and the catalyst are in the same phase, or the heterogeneous case, mostly describing the interaction of molecules with the surface of a solid [4]. Heterogeneous catalysis is more relevant for technical reactions, bearing the advantage of catalytic material that does not have to be separated from the products [5, 6]. Therefore, the catalysts are optimised for the highest reaction rate and most importantly the best selectivity, which is still mainly based on the empirical method of trial and error. Even if the broad features of an industrial catalyst are known, most of the reaction mechanisms can not be described in detail [7]. The reason being most heterogeneous catalysts have structures of great complexity, making an investigation of the underlying mechanisms hardly feasible. One approach to tackle this issue is to study simplified model systems with reduced complexity, as for example metal single crystals under controlled ultra-high vacuum (UHV) conditions. The gained knowledge of the fundamental principles enables to expand theory to more complex systems used in practical catalysts [8]. The concept of reductionism to gain an understanding that can ultimately lead to rational catalyst design is valid until nowadays [9]. Experimental studies in combination with ab initio calculations could help to understand some reaction mechanisms of simple molecules with already complex pathways. A prominent example is the nitrogen fixation in the Haber-Bosch process, where the surface science approach is able to give a quantitative description of an industrial reaction. Here, different crystal planes are used to model the active sites of the catalyst [4]. However, these investigations cannot address the size-dependencies of catalytically active metal particles and the influence of the support on their structure, shape and electronic properties [10]. To bridge the shortcomings of single crystal studies, supported model catalysts are introduced [11]. These model systems consist of metal particles supported on single crystals or thin films [10]. On the nanoscale, clusters reveal unique physical and chemical properties, which are not scalable from those of bulk materials [12]. Therefore, more sophisticated studies on size-selected metal clusters are performed with great experimental effort [13, 14, 15]. It turns out that every atom composing a supported cluster counts for the catalytic activity [16, 17]. The effect can be so strong that a certain cluster size is active, whereas the bulk material is unreactive [18, 19]. Ideally, microscopic properties such as atomic composition, electronic and geometric structure should be related to macroscopic properties such as catalytic activity and selectivity [20]. For this reason, also investigations on the local scale are performed on the supported model catalysts up to atomic resolution [21, 22]. Further in situ microscopy studies reveal that also nanoparticle dynamics must be included for the correct description of catalytic behaviour, as for example sintering processes or shape changes [23, 24].

Therefore, a combination of integral measurements on the catalytic properties of metal nanoparticles linked to concomitant dynamics under reaction conditions is desirable. In this work a supported model system with reduced complexity is investigated on the integral and local scale to gain further insights on the catalytic behaviour of nanoparticles under reaction conditions. This consists of size-selected Pd clusters as a catalyst, soft-landed on the well-defined h-BN/Rh(111) moiré superstructure. The utilization of this supported model system bears several advantages:

The moiré superstructure is based on the lattice mismatch of the Rh(111) single crystal and a monoatomic h-BN film. Local studies by STM are benefited due to the relatively flat boron nitride nanomesh with a STM corrugation of 0.8 Å, which is chemically inert to reactive gasses and therefore passivates step edges on the Rh(111) single crystal [25]. Furthermore, the moiré superstructure prevents bulk diffusion and comprises distinct adsorption sites for the nanoparticles, which stabilizes the clusters due to a high activation barrier even at elevated temperatures. The support is periodically wettable, which entails that every size-selected cluster has the same chemical environment. This true monodispersity enables the investigation of stabilised, atomically precise nanoparticles under reaction conditions. Hence, local and integral techniques can be combined.

The investigations focus on Pd nanoparticles, attractive due to their wide-ranging properties as a catalyst. Pd is one of the most versatile metal in promoting or catalysing reactions, many of which are not always easy to achieve with other transition metal catalysts. Most importantly, Pd catalysts offer an abundance of possibilities of carbon-carbon bond formation in organic synthesis with a high tolerance for functional groups such as carbonyl and hydroxyl groups [6, 26]. Furthermore, the hydrogen chemistry [27, 28] and oxidation catalysis [29] is important for the production of fine chemicals. Additionally, Pd finds application as a catalyst in the automotive emissions control [30], electrochemistry [31, 32, 33, 34, 35, 36] and in sensor technologies [37, 38, 39]. The manifold applications are based on the various oxidation states of Pd, with Pd(0) and Pd(II) being the most relevant. Generally speaking, a catalytic cycle starts with the oxidative addition of a carbon-hydrogen, carbon-heteroatom bond or H_2. Intermittently, carbon-carbon or carbon-oxygen double bonds can be inserted. The last step of a catalytic cycle is the reductive elimination, often accompanied by the abstraction of either a β-H, β-heteroatom or β-carbon [26]. Many forms of Pd are used as catalysts, but the truly catalytically active species are mostly still under discussion. Potential breakthroughs are expected by in situ studies of the dynamics of palladium under reaction conditions, which will aid in in the rational design of future generations of catalysts [40].

The catalytic activity of the nanoparticles is investigated with a freshly implemented TPD setup. This device shall be exploited as a screening method to check for cluster reactivity, that can ultimately be investigated in the variable temperature STM under reaction conditions. The complex STM sample holder with a relatively small single crystal of 4.4 mm in diameter and the low cluster coverage, in order to ensure size-selectivity, represent a real sensitivity challenge for the new device. To tackle these issues, a residual gas analyser is equipped with a modified Feulner cone to increase the sensitivity of the device by guiding the desorbing gases to the ionization part of the mass spectrometer and to reduce the UHV background contributions [41]. The TPD measurement is controlled via a LabVIEW program in combination with a proportional-integral-derivative (PID) regulator. In this context, an evaluation routine is established, as well as a consistent calibration with the well-known $\mathrm{Rh(111)\text{-}(1\times 1)\text{-}D}$ and $\mathrm{Rh(111)\text{-}(2\times 2)\text{-}C_2H_3}$ overlayers. Following the implementation of the TPD setup, measurements with unselected Pd clusters on h-BN/Rh(111) are performed, investigating the $C^{18}O$ oxidation. The $C^{18}O_2$ peak at 380 K is in good agreement with literature on Pd(111) [42]. The catalytic activity rises in consecutive TPD runs, which could be explained by an oxygen accumulation, the formation of carbonaceous deposits or cluster ripening. The latter can be confirmed by STM measurements performed before and after the TPD series. Furthermore, the co-adsorption of D_2 and C_2H_4 is studied with size-selected Pd_{19} clusters supported on h-BN/Rh(111). Here, only 20% of the moiré troughs are occupied with a single cluster, which corresponds to less than 0.15% with respect to the Rh surface atoms. The two desorption signals at 180 K and 330 K can be assigned to the hydrogenation reaction and an H-D exchange. A peak evolution takes place during a series of consecutive TPD measurements, meaning a decrease in the hydrogenation activity and an increase of the H-D exchange reaction. The findings are compared with studies on Pd nanoparticles evaporated on Al_2O_3/NiAl(110), showing similar results [43, 44]. STM measurements before and after the TPD series with 13 cycles show subtle ripening of the Pd clusters, comparable to previous annealing experiments to 500 K in our group [45, 46]. The ripening behaviour of the nanoparticles is not altered by potential carbonaceous deposits formed by dehydrogenation as shown with further STM measurements after an additional annealing step at 700 K.

Apart from integral measurements on the catalytic activity of the Pd clusters, also local investigations under reaction conditions could be performed with a variable temperature STM. Two main ripening mechanisms could be derived from size distributions of formerly size-selected clusters. In the Ostwald type, the cluster disintegrates and in most cases single atoms diffuse on the surface, whereas in Smoluchowski ripening the whole cluster moves as an ensemble. A merging of the diffusing particles leads to changes in the size-distributions [45, 46]. In addition, a restructuring and reshaping of the clusters has been observed [46]. Furthermore, it has been shown that adsorbates can lower the barrier for the diffusion of nanoparticles down to atoms [47, 24, 48]. However, mobility of the particles as well as structural changes often occur on time scales not accessible for conventional STMs. In the past, mainly two concepts led to an enhancement of the time resolution with STMs. One being the tracking mode, that enables a time resolution down to the millisecond with low currents and a fast vertical feedback [49, 50]. Most of the previous work with this technique focused on the dynamics of atoms and dimers, but recently also a Pd^{12} cluster could be tracked on graphene/Rh(111) [51]. However, one of the biggest drawbacks of this technique is that only the tracked species is investigated and interactions with neighbouring species that might influence the diffusion behaviour cannot be recognized during the experiment. Therefore, often additional STM images are needed to ensure the interpretation of the investigated diffusion processes. Another way is to generally increase the frame rate [52]. These high speed STMs are specially constructed with a rigid and compact design to achieve high mechanical resonance frequencies and contain high bandwidth I/V and A/D converters in combination with prompt feedback electronics. The biggest benefit of fast STMs compared to the tracking technique is, that an area is imaged, which enables the investigation of parallel events and interactions with the surrounding. However, these measurements typically have to be performed at higher current setpoints in order to achieve the high bandwidths needed with the I/V converter, which increases the chance for tip sample interactions. Part of this work is the implementation of an add-on instrument that enables a conventional variable temperature STM to operate at video rates and beyond [53, 54]. This also includes the development of an evaluation program from scratch. After the characterisation of the FAST module with static surfaces down to atomic resolution on Rh(111), the mobility of Pd clusters and atoms is investigated on h-BN/Rh(111). The diffusion of a particle formed by decomposition of Pd_{12} at 375 K is studied in detail for 3 hours with a time resolution of 125 ms. The residue is caged in a h-BN/ Rh(111) trough. The analysis of the geometric center of the particle per frame reveals a hexagonal pattern with a lattice vector of ~3 Å. A further evaluation of the residence times per site shows, that the six thermodynamically equivalent sites are separated by two distinct activation barriers, resulting in diffusion events on two time scales. Furthermore, potential influences of bias and current setpoint on the particles mobility are investigated in the range from 200 pA to 1000 pA and ±1 V. Thereby, the diffusion behaviour of the residue is not altered. Furthermore, Pd atoms could be soft-landed and immobilised on h-BN/Rh(111) at liquid nitrogen temperatures. STM measurements at 170 K revealed ring-like structure in the h-BN/Rh(111) troughs. The enhanced time resolution of the FAST module can provide the evidence that the apparent rings in the conventional STM measurements are caused by a circular motion of the Pd atoms with an angular frequency of ~2 Hz.

Summing up, the aim of this work is to cross-link catalytic activity of nanoparticles with accompanying dynamics. The insights on the Pd cluster mobility during reaction conditions shall help to understand the dynamics of catalytically active species, which can ultimately be a step towards rational catalyst design.

2. Experimental setup

In the following, a short overview of the utilized UHV setup and its attached devices is given. A schematic drawing of the UHV chamber is depicted in figure 2.1. The setup can be divided in three main parts by gate valves. These are the preparation chamber, representing the centre of the setup, with the STM chamber and the cluster source attached to it. The main chamber is pumped by an ion pump (Varian, VacIon Plus 300) with an included titanium sublimation pump and a turbopump (Pfeiffer Vacuum, HiPace 300 M) with an active magnetic bearing in combination with a multi-stage roots backing pump (Pfeiffer Vacuum, ACP 15). The STM chamber contains an ion pump (Varian, VacIon 150) and a titanium sublimation pump (VACGEN, ST22). The titanium sublimation pumps are only operated directly after a bake out in order to avoid sample contamination. The STM and the preparation chamber are typically operated at a base pressure in the range of $1 \cdot 10^{-10}$ mbar.

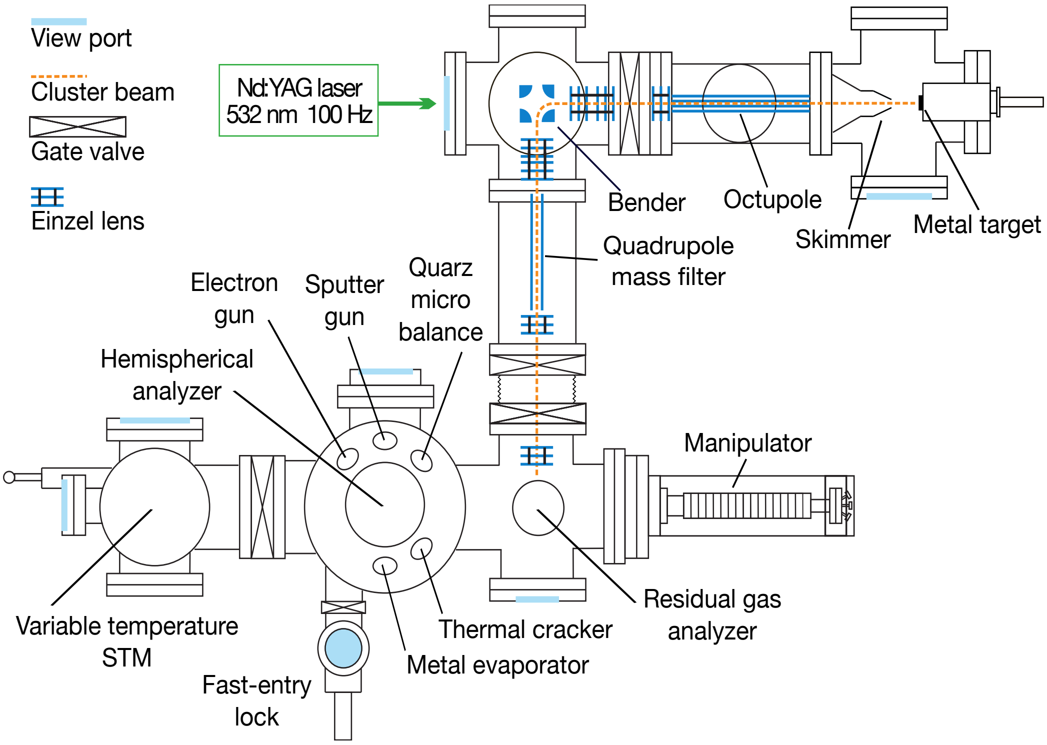

Figure 2.1.: Schematic drawing of the UHV chamber.

The laser evaporation cluster source is based on the design of Heiz et al. [14, 15]. The cluster source of this UHV chamber has already been described earlier by M. Bieletzki and refined by M. König [55, 46]. On the contrary to the STM and preparation chamber, the cluster source is operated at a base pressure in the range of only $2 \cdot 10^{-8}$ mbar at the quadrupole mass filter. The reason for this is that the pumps have to be switched off while measuring with the STM for vibrational reasons. Therefore, the source is always vented with nitrogen after the cluster deposition to prevent long-term pump oil contaminations. In order to ensure an acceptable backpressure and to minimize background contaminations of the produced clusters, the source is always pumped over night before being operated.

The preparation chamber contains several devices for sample preparation and characterization purposes. A sputter gun (Specs, IQE 11/35) is included for sample cleaning. Thin films can be grown on the single crystal surfaces with a metal evaporator (Omicron Nanotechnology, EFM3) in combination with a quartz microbalance (INFICON, SL-A1E40). A thermal cracker (Oxford Applied Research, TC50) can be used to further treat surfaces or metal nanoparticles with radicals. Furthermore, a gas line equipped with leak valves (VACGEN, LVM series/Pfeiffer Vacuum, UDV 046) and the chemicals listed in table 2.1 is available. The borazine is stored in a cooling device below 278 K for stability reasons, as already described earlier by M. König [46]. For integral measurements, the chamber is equipped with a residual gas analyzer (Stanford Research Systems, RGA200), which is used for maintenance reasons and modified for TPD measurements as described in chapter 4. Furthermore, an Auger electron spectrometer (AES) (Omicron Nanotechnology, EA125) is attached to the UHV chamber. A variable temperature microscope (Omicron Nanotechnology, VT-AFM) is installed for local probes, enabling STM as well as atomic force microscopy (AFM) measurements. In the course of this work, the microscope has been equipped with an add-on instrument to enable STM measurements at video rates and beyond in chapter 6. The inward and outward transfer of the samples can be executed via a fast-entry lock, pumped separately by a turbopump (Pfeiffer Vacuum, TC100) in combination with a rotary vane backing pump (Leybold Vacuum, TRIVAC D4B).

Table 2.1.: Cleanliness and origin of the used chemicals in the gas line.

Chemical	Composition	Origin
Hydrogen	99.999%	Westfalen Gas
Deuterium	99.999%	Westfalen Gas
Oxygen	99.998%	Air Liquide
Carbon monoxide	99.97%	Westfalen Gas
Ethene	99.5%	Westfalen Gas
Borazine	99%	KatChem
Argon	99.9999%	Air Liquide
Helium	99.9999%	

The investigated single crystals are mounted on a sample holder and can be controlled in the chamber via a corresponding manipulator head (Dodecon Nanotechnology). A speciality of the UHV setup is that the sample holder already contains the infrastructure for the temperature readout and heating. The design, developed together with W. Stiepany (Max-Planck-Institut für Festkörperforschung, Stuttgart), allows for a rapid and yet precise temperature control. Moreover, the sample holder is securely movable inside of the UHV setup and fits tightly in the manipulator and more importantly in the microscope. The design has to be rigid, so that no mechanical vibrations affect the STM measurements. This has to be the case in a wide temperature range from liquid nitrogen to the annealing temperature of the Rh(111) single crystal at 1253 K. Figure 2.2 shows the complex sample holder design.

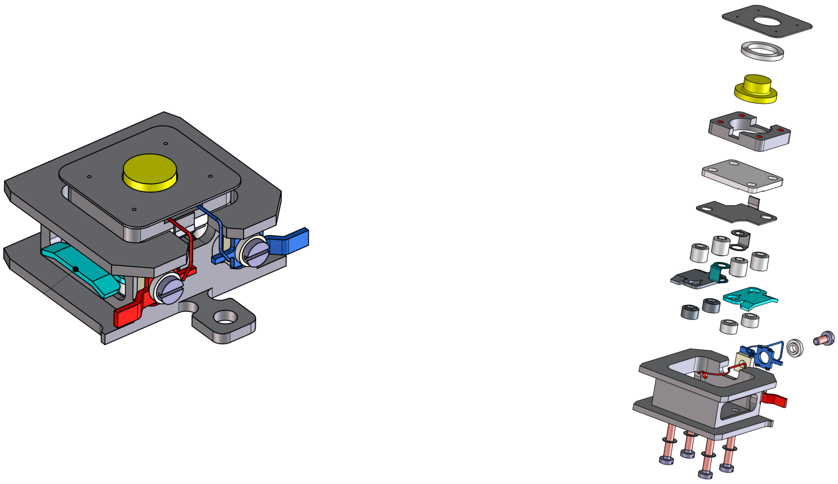

(a) Schematic drawing.

(b) Exploded view.

Figure 2.2.: Sample holder design for Rh(111).

The main body of the sample holder is made of titanium and houses a layered internal structure, that is held together by four long screws. These are initially made of molybdenum and later out of titanium. The reason for this change is an elongation of the molybdenum screws above 1300 K, leading to eigenfrequencies of a loose sample holder disturbing STM measurements. The resistive heating element is a graphite coated pyrolytic boron nitride (PBN) plate, with two contacts out of molybdenum to the side of the sample holder. One of these contacts is the connected with the main body of the sample holder and represents ground. A plate out of titanium is placed underneath the PBN heater, which acts as a radiation shield as well as for stability. The spacing rings are made out of sapphire, which serve for electrical isolation and their temperature dependent thermal resistance is beneficial for heating and cooling [56]. The four molybdenum screws are laser welded after being tightened with the titanium top plate of the sample holder, to ensure that no loosening layered design takes place during repeated annealing cycles. The single crystal fits in a hole of the top plate of the sample holder, is in direct contact to the resistive PBN heating element and is fastened by spot welding a titanium press foil on top of a sapphire spacing ring. The sample has a diameter of 4.4 mm at the top and 7.0 mm at the bottom. The temperature readout is realised by a type K thermocouple. The chromel and alumel wires touch directly the side of the single crystal hat and can be contacted separately by springs at the two handles situated at the hook side of the sample holder. This small hook is used for sample transportation with wobble sticks and transfer rods.

The sample holder fits perfectly in the manipulator head illustrated in figure 2.3 and already described earlier by M. Bieletzki [55]. The resistive PBN heating element of the sample holder can be accessed at B and C in figure 2.3a. The contacts D and E can be used for e-beam heating, G to the ground of the manipulator head and F is the ground of the STM tip stage. Furthermore, figure 2.3b shows three type K thermocouples. The contacts A and B daisy-chain the thermocouple of the sample holder, whereas I and J allow a temperature readout of the main body of the sample holder. The temperature of the manipulator head itself can be monitored with G and H.

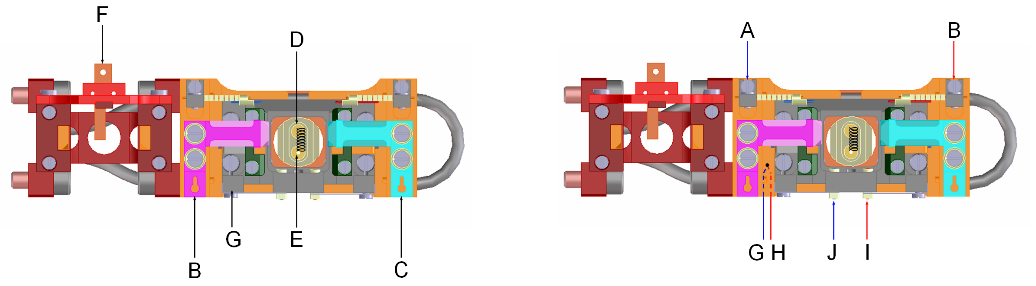

(a) Power & grounding feedthroughs (b) Thermocouple contacts

Figure 2.3.: Schematic drawings of the manipulator head.

How the sample holder fits into in the variable temperature STM, can be seen in figure 2.4. For that purpose, the microscope sample station has been retroactively equipped with Type K contact springs, establishing a direct temperature readout of the sample.

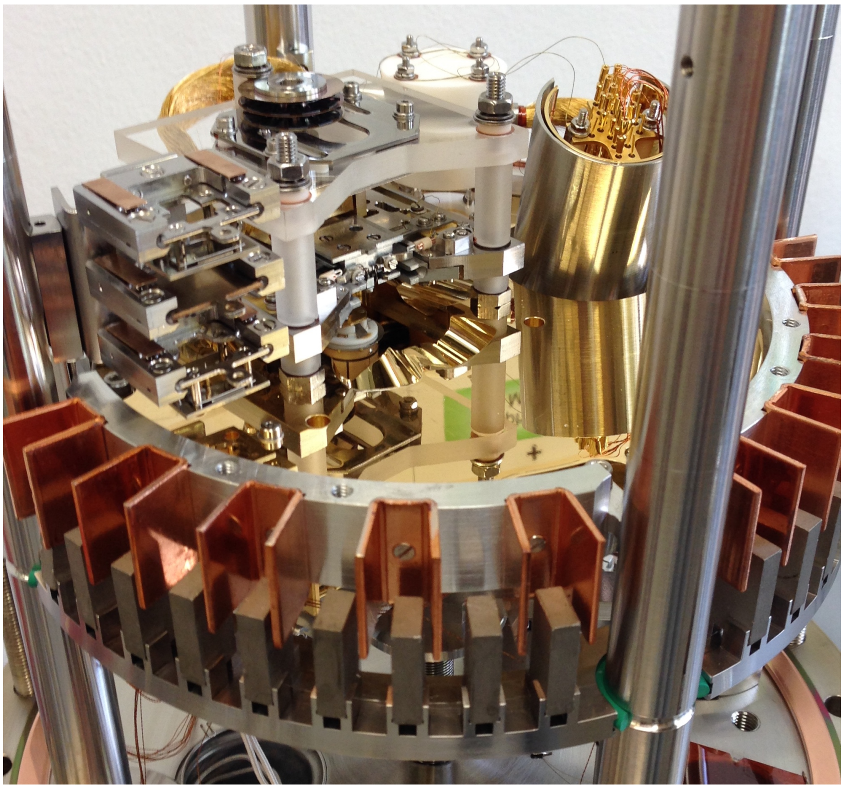

Figure 2.4.: Variable temperature STM with mounted sample holder.

3. Sample preparation

3.1. Growth of h-BN/Rh(111)

The Rh(111) single crystal is always cleaned with the following standard procedure. The surface is sputtered for 10 min with an argon backpressure of $5 \cdot 10^{-6}$ mbar and an acceleration voltage of 1.5 kV. A sputter current of about 300 nA can be measured at the filament normally used for the e-beam heating in the manipulator. The single crystal is annealed subsequently for 10 min at 1253 K. This sputter and anneal procedure is repeated 3 times, however the last annealing step is shortened to 5 min. This way carbon segregation processes from the Rh bulk is reduced. The cleaned Rh(111) single crystal is hold at 1073 K directly in the cool-down of the last annealing step and borazine is dosed for 3 min with a partial pressure of $6 \cdot 10^{-7}$ mbar to grow the h-BN film [57, 58, 59, 60]. The borazine is cleaned by three pump-thaw cycles prior to each synthesis in order to ensure a high quality film growth. In this process, the borazine is frozen with liquid nitrogen and the residual gas phase in the vessel is pumped down with a turbopump. Therefore, first the volume between leak valve and needle valve is evacuated. After closing the leak valve and then opening the needle valve, the residual gas phase over the frozen borazine can be pumped down by opening the leak valve carefully. After closing both valves again the borazine is molten again by removal of the liquid nitrogen. A high borazine quality is crucial to obtain defect free h-BN films. However, borazine is not stable over a long time at room temperature and sensitive for water and ultraviolet light. Therefore, the chemical is transferred in the storage vessel with a Schlenk line under argon atmosphere. The high quality is preserved by a storage in the dark and below 278 K in a cooling device [46]. Figure 3.1 shows STM images of the h-BN/Rh(111) surface, prepared with the above mentioned procedure.

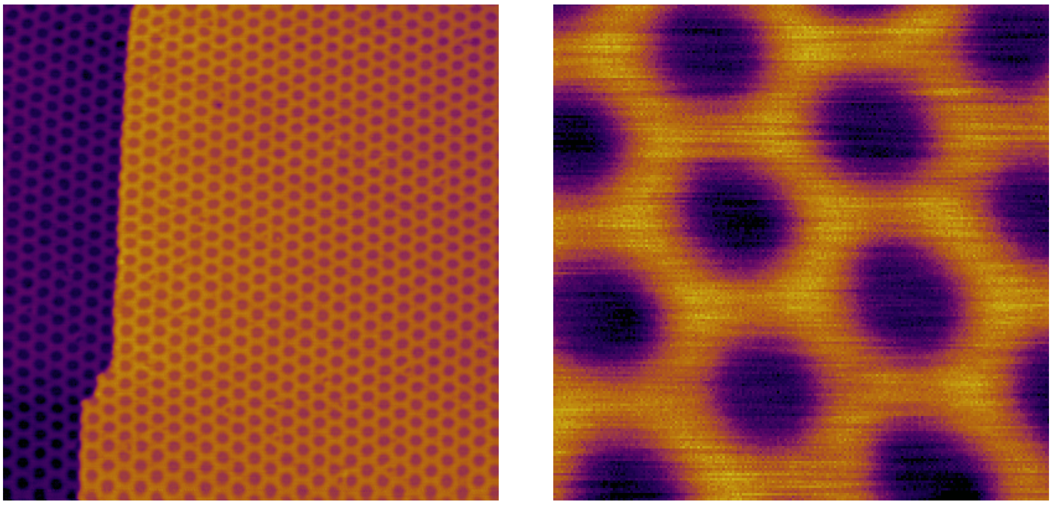

(a) [1 pA, -0.6 V, 100×100 nm^2]

(b) [1 pA, -0.6 V, 10×10 nm^2]

Figure 3.1.: STM images of the h-BN/Rh(111) superstructure.

The moiré superstructure consists of a single but corrugated monolayer of h-BN on Rh(111) [58]. The lattice constants of Rh(111) (268.7 pm) and h-BN (250.4 pm) differ by 6.8%. For this reason, a supercell forms by coincidence of 13×13 h-BN pairs on 12×12 Rh atoms [57, 61, 59]. The highly regular hexagonal structure has a periodicity of 3.22 nm with pores of about 2 nm in diameter. The appearance of the pores can vary depending on the STM tip conformation and is also bias dependent. The pores appear to be higher than the wires at sufficiently high positive biases [62]. The monolayer binds strongly to the underlying metal in the pores, whereas the wire regions are not bonded to the Rh(111) surface but only through strong cohesive forces within the film itself [58, 63, 64]. Ab initio density functional theory (DFT) studies show that the N atom is repelled from the surface, whereas the B atom is attracted to it. The interaction strength depends on their position relative to the underlying Rh atoms. The B attraction dominates the N repulsion only when B occupies fcc or hcp hollow sites and N is located on top sites, then h-BN is bound to the surface [60, 65]. The non-uniform charge transfer from the h-BN layer results in the development of lateral electric dipoles that can trap molecules and atoms [66, 65, 67]. This effect could already be used for Xe atoms [68], Mn, Co and Fe metal adatoms [69], Co clusters [70], water clusters [71, 25], size-selected Pd_{19} clusters [45] C_{60} [57] and naphthalocyanine molecules [58]. As already mentioned before, a defect-free h-BN film requires a high quality borazine, as these can alter the properties of the film on the local scale. The defects are classified in self-interstitials N_i , N_i and vacancies V_N, V_B. The self-interstitials have low formation energies, comparable to the vacancy defects. However, N_i is found to be the most stable defect in h-BN, followed by V_B [72]. Other long-range disorders are caused by domain boundaries where the stacking of the B atoms with respect to the substrate changes from face centered cubic (fcc) to hexagonal closed packed (hcp), as for example seen on Ni(111) [73, 74]. Point defects on h-BN can be quantified by individual Ti atoms, that can adsorb and dissociate hydrogen [75].

3.2. Cluster deposition

For vibrational reasons, the pumps of the cluster source are turned off during STM measurements. To avoid oil contaminations by the pumps, the source is filled with nitrogen while not used. The filling with nitrogen instead of air speeds up the evacuation process significantly, because less water is introduced into the chamber. The cluster source is evacuated over night prior to the deposition of clusters. The backpressure in the quadrupole region is typically in the range of $2 \cdot 10^{-8}$ mbar. Before depositing clusters onto the sample surface, the source is operated for 15 min with a closed gate to the preparation chamber to ensure that clean clusters and no carbon or oxide species are formed. The coverage is controlled by monitoring the cluster current on the manipulator head. Unless otherwise noted, the sample is hold at room temperature while depositing the clusters. For smaller clusters it is necessary to cool the sample down to 130 K during the deposition to suppress cluster ripening. Furthermore, the kinetic energy of smaller clusters and atoms has to be controlled precisely in order to prevent knock-on damages in the h-BN film [46]. The predicted displacement energy for B or N is about 20 eV with electrons [76, 77] and 50 eV with Rb atoms [78]. Figure 3.2 shows STM images of soft-landed, size-selected Pd_{19} clusters and Pd atoms on h-BN/Rh(111).

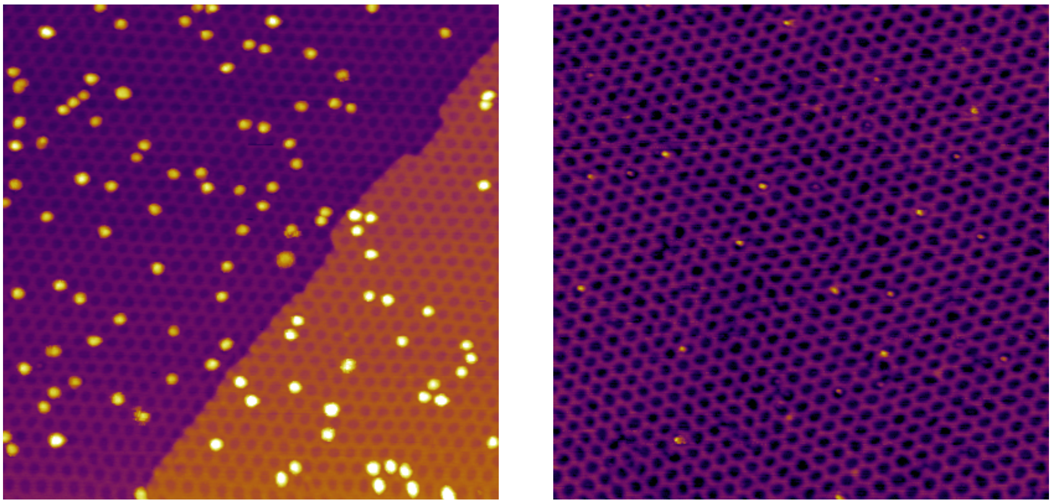

(a) Pd_{19} [1 pA, -0.8 V, 100×100 nm^2] (b) Pd atoms [1 pA, -0.6 V, 100×100 nm^2]

Figure 3.2.: STM measurements of size-selected Pd_{19} clusters and Pd atoms on h-BN/Rh(111).

4. TPD implementation

The main objective of this work is to probe the interplay of catalytic activity of Pd clusters deposited on h-BN/Rh(111) and their dynamics, as measured in detail with a variable temperature STM. Pd is investigated, because of its wide-ranging properties as a catalyst. Particularly noteworthy is the abundance of possibilities in carbon-carbon bond formation in organic synthesis [6, 26], the hydrogen chemistry [27, 28] and the application in oxidation catalysis [29, 30]. A reactivity screening is required in advance, which is not reasonable with time-consuming local probe techniques. However, this screening can efficiently be performed by integral TPD measurements with precise control in an apparatus that has been tuned for maximum accuracy. Here, pre-dosed gases undergo reactions catalysed by the nanoparticles while heating up. The temperature-dependent products are measured via mass spectrometry. The complex sample holder, initially optimised for a variable temperature STM, with a relatively small single crystal of 4.4 mm in diameter, and low cluster coverages to ensure the size-selectivity of the nanoparticles represent a serious sensitivity challenge for the TPD setup.

4.1. Setup

In the following section, the main components and modifications of the TPD setup are described. The sample holder, depicted in figure 2.2, contains type K thermocouples contacted to the side of the top hat shaped crystal for temperature readout and a PBN heating element that is in direct contact to the backside of the crystal. For TPD measurements the linear heating ramp is controlled by a PID regulator (2408, Eurotherm) and the maximum power is limited with a power supply (DCS60-20E, Sørensen). The PID settings are optimised manually for different cooling efficiencies of the manipulator. The cooling is realised by flushing the manipulator with cold gaseous nitrogen, so that a sample temperature down to 130 K can be realised.

The reactants, see table 2.1, are dosed with leak valves at the desired temperatures. While heating up with typically 2 K/s, the reaction products are analysed with an in-house modified residual gas analyser (RGA200, Stanford Research Systems, Inc.), which is already described in previous work of this group [46]. Here a modified Feulner cone [41] is attached to the front end of the mass spectrometer to guide the desorbing gases from the single crystal surface to the ionisation part of the mass spectrometer, see figure 4.1a. At the same time, the modification suppresses background signals caused by various adsorbates desorbing from the extremely complex STM sample holder that heats up during the temperature ramp.

Therefore the inlet of the modified Feulner cone has a smaller diameter of 3 mm, compared to the Rh(111) single crystal with 4.4 mm, ensuring that only molecules in line of sight to the mass spectrometer are detected.

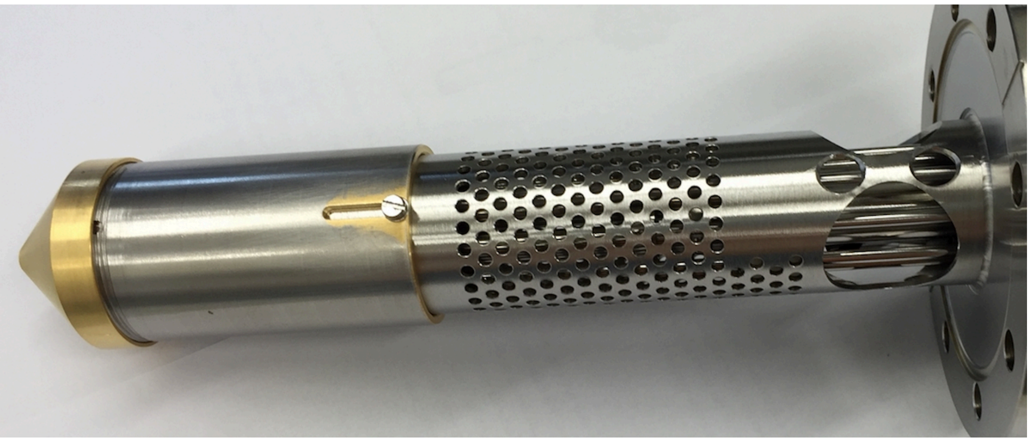

(a) Modified Feulner cone attached to the residual gas analyser

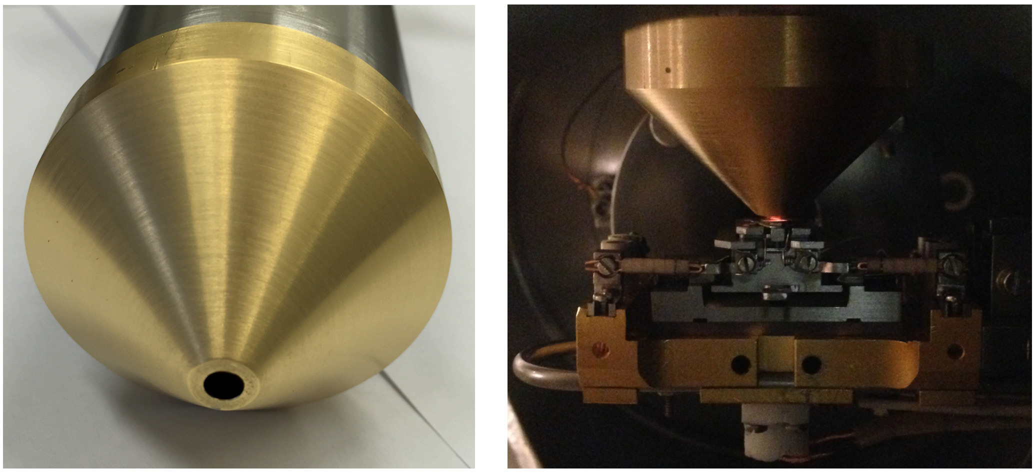

(b) Gas inlet (c) TPD measurement configuration

Figure 4.1.: Modified Feulner cone attached to the front end of the residual gas analyser.

A LabVIEW program controls the temperature ramp, the mass spectrometer and the data acquisition of up to 6 signal traces measured in a sequential, cyclic way. A decrease of the noise floor can be achieved by reducing the bias voltage at the channel electron multiplier (CEM). The result is a better signal to noise ratio (S/N) and therefore a lower detection limit, but also the measurement time per data point is prolonged. The noise floor value is set as low as possible, but still ensuring that at least one data point per kelvin is recorded for each measured trace. The saved log file contains the time, temperature and ion current for the selected mass to charge ratio (m/z) in a tab delimited form. Despite the higher background level of the residual gas analyser compared to high-end mass spectrometers and the broad TPD signals caused by the low pump rate of the Feulner cone, the in-house built modification proves to be a valuable tool to determine reaction parameters for the probed clusters.

4.2. Experimental procedure

In the following, the modus operandi for TPD measurements is described in a general way. To begin with, the single crystal is placed approximately 5 mm in front of the inlet of the Feulner cone and cooled down as far as possible. This is realised by cooling the manipulator head by flushing with a constant flux of cold gaseous nitrogen, which is obtained by pressure build-up in a liquid nitrogen dewar. Here, a constant overpressure of 0.5 bar is set manually, to ensure comparable cooling power for the experiments. This way, the same PID settings for the ideally linear temperature ramps can be used. Sample temperatures down to 130 K can be achieved. Since this cooling process takes around 30 min, a blank TPD run is performed to desorb residual gases from the sample and to check the current PID settings that depend on the cooling power. The ion getter pump in the preparation chamber is turned off during the gas dosages and not turned on again until a base pressure below $1 \cdot 10^{-8}$ mbar is achieved, to ensure a long lifetime of the pump. After the gas exposure and cool down the desired start temperature, the sample is approached to a distance below 1 mm to the entrance of the Feulner cone to minimize background distortions of the multi-material sample holder during the TPD measurements. The actual TPD measurement is started below a base pressure of $2 \cdot 10^{-9}$ mbar with a linear temperature ramp of 2 K/s. Higher heating rates are not reasonable due to limitations of the PBN heating element in the sample holder. Additional data points 30 s before the temperature ramp, 60 s at the end temperature and during cool down to 273 K are recorded, if background corrections are necessary for the data analysis.

4.3. Data analysis

The TPD log files are evaluated with a program based on IGOR Pro (Version 6.73, WaveMetrics, Inc.). A boxcar smoothing algorithm, taking the sliding average of 13 adjacent data points, is applied for noise reduction in the desorption spectra. In the following, all TPD runs are smoothed with this sliding average algorithm.

Often raw TPD traces contain background contributions that hinder the quantitative evaluation of the spectra. These background contributions are determined by evaluating as well the traces before the start of the ramp, a 1 min dwell period at the final temperature of the TPD run and during the cool down phase to room temperature.

4.3.1. Temperature dependent background

The extremely complex STM sample holder, whose layered design includes unavoidable dead volumes, can lead to a temperature dependent background contribution. The background contribution is expected to be linear proportional to the temperature, fitted during the cool down phase after the TPD measurement and then applied for the entire spectrum. This type of background correction is only necessary for TPD spectra of H_2. Figure 4.2a shows an exemplary TPD spectrum of $m/z = 2$ with proposed background correction function and figure 4.2a the corrected graph.

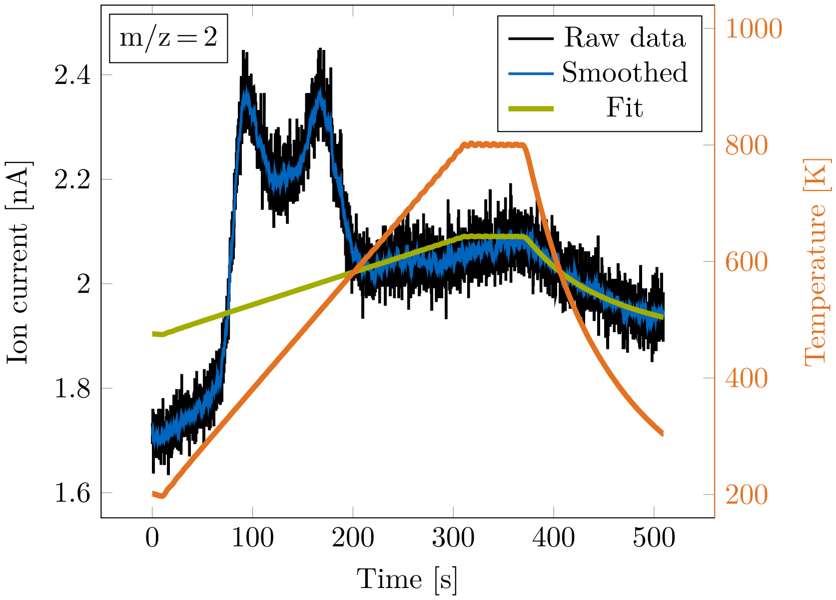

(a) Raw data with background fit

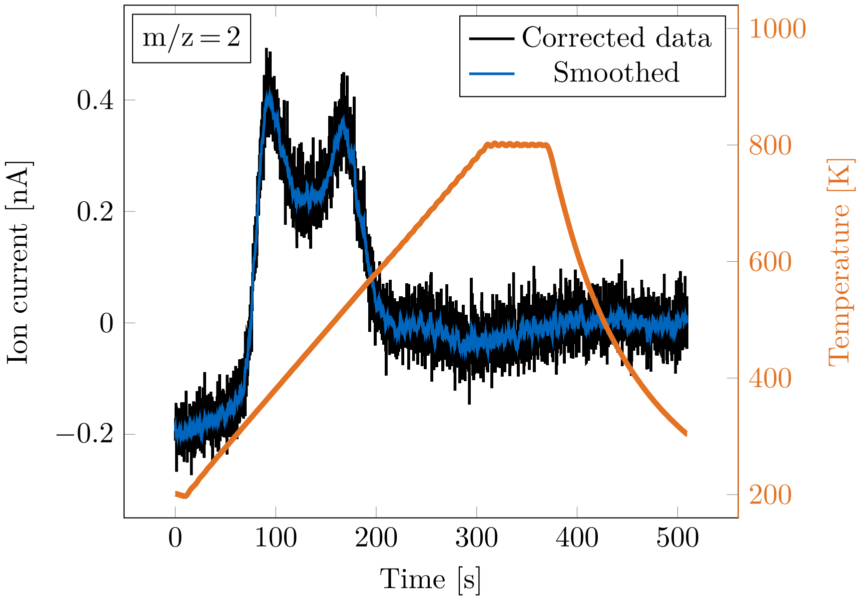

(b) Background corrected TPD spectrum

Figure 4.2.: Blank TPD spectrum, illustrating the temperature dependent background correction.

4.3.2. Time dependent background

A further background contribution is associated with the slow pumping speed of the Feulner cone, pumped only by the surrounding main chamber. For vibrational reasons, only one magnetic turbo pump is attached to the chamber. Therefore gases with a high sticking coefficient are pumped very slowly, which becomes more pronounced with the number of TPD measurements performed that day. To reduce the waiting times for a constant backpressure, a time dependent background correction is implemented. For this purpose a linear function is fitted to the regimes with constant temperature before the start of the TPD measurement and during the 1 min dwell time directly after reaching the final ramp temperature. The background for the entire spectrum can then be calculated for each TPD trace with the previously fitted parameters and subtracted. Figure 4.3a shows a TPD spectrum of $m/z = 29$ after co-adsorption of D_2 and C_2H_4 with proposed linear background function. The linear intensity drop after the temperature ramp is caused by the slow pumping performance of the chamber. The corrected TPD spectrum is depicted in figure 4.3b.

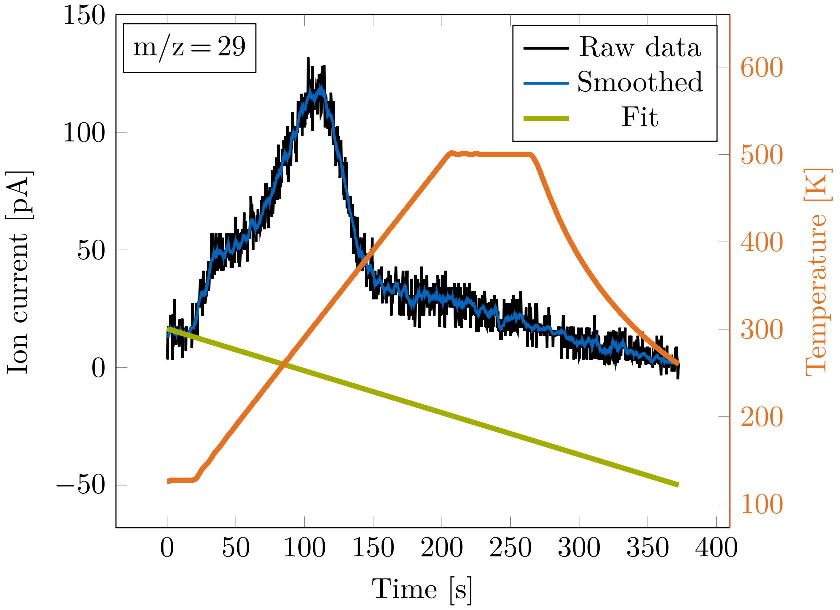

(a) Raw data with background fit

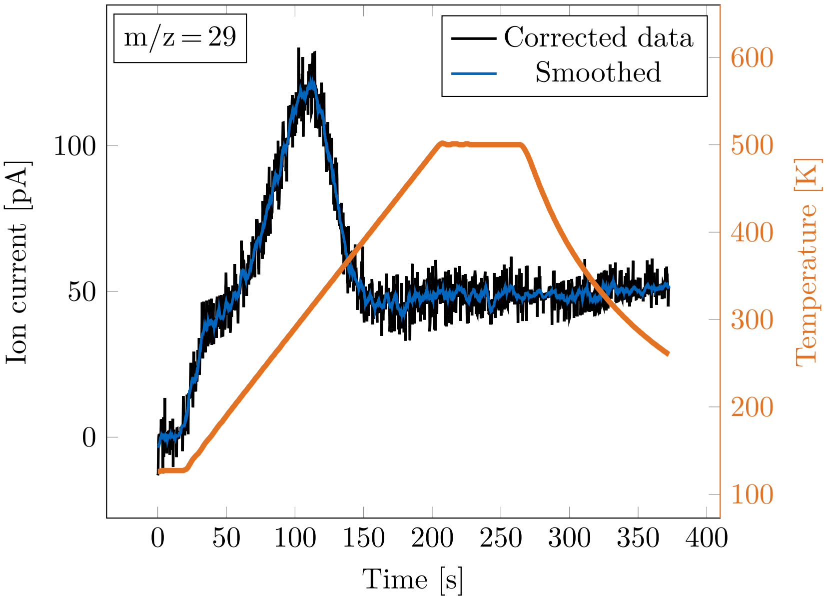

(b) Background corrected TPD spectrum

Figure 4.3.: TPD spectrum after co-adsorption of D_2 and C_2H_4, illustrating the time dependent background correction due to the slow pumping speed of the modified Feulner cone.

4.3.3. Shirley background

An intrinsic problem using the Feulner cone is the accumulation of desorbing species inside of the ionisation part of the residual gas analyser. In this case the background increases proportional to the desorption yield. It was figured out that the Shirley background correction method, originally developed for the evaluation of X-ray photoelectron spectroscopy (XPS) spectra, is suitable for this task [79, 80]. Here the background contribution due to inelastic scattering is proportional to the total peak area for low binding energies [81, 82]. The time-dependent Shirley background function $B_{Shirley}$ can be derived with the equations 4.1 and 4.2.

$$B_{Shirley}(t) = k \cdot \left[\int_{t_{init}}^{t} S(t)dt - \int_{t_{init}}^{t_{start}} S(t)dt \right] + S(t_{start}) \tag{4.1}$$

$S(t)$ is the signal intensity of the trace to be background corrected and t the time with t_{init} the initialisation time, t_{start} at the beginning and t_{stop} at the end of the temperature ramp. The scaling factor k makes sure that the Shirley background fit passes through the point $S(t_{stop})$.

$$k = \frac{S(t_{stop}) - S(t_{start})}{\displaystyle\int_{t_{init}}^{t_{stop}} S(t)dt - \int_{t_{init}}^{t_{start}} S(t)dt} \tag{4.2}$$

This iterative process is repeated 4 times for every TPD trace. Figure 4.4a shows a TPD spectrum of m/z = 2 after co-adsorption of D_2 and C_2H_4 with proposed Shirley background fit. The corrected TPD spectrum is depicted in figure 4.4b.

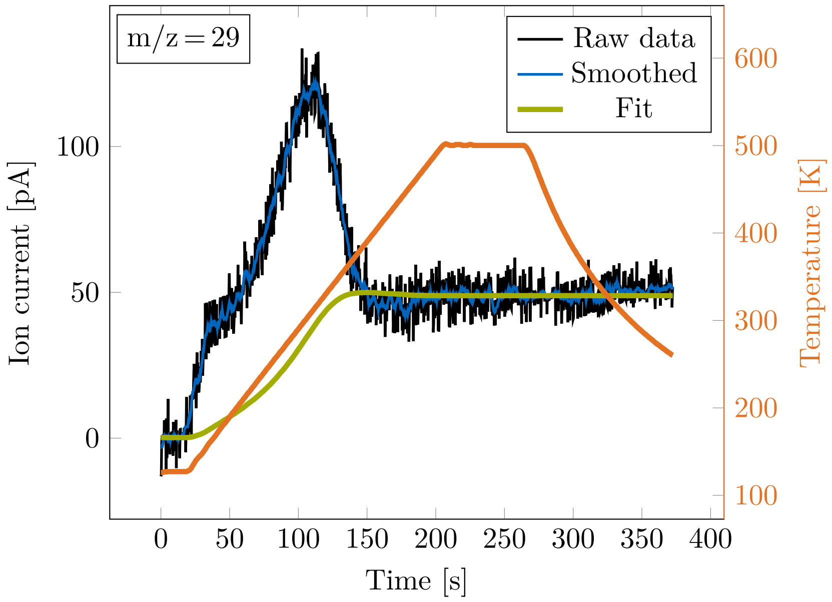

(a) Raw data with background fit

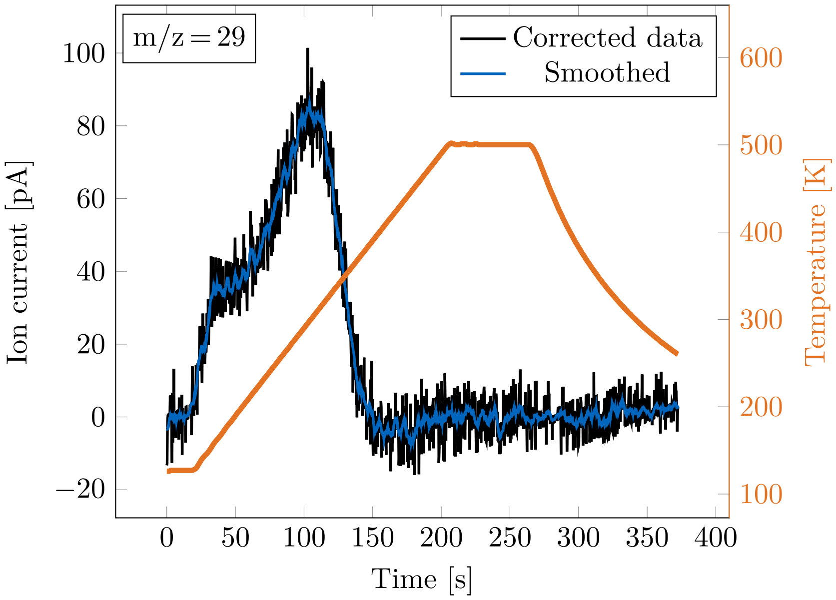

(b) Background corrected TPD spectrum

Figure 4.4.: TPD spectrum after co-adsorption of D_2 and C_2H_4, illustrating the Shirley background correction.

In particular, attention was paid to find a routine that is reproducibly applicable to all of the data and ensures therefore comparable results. Blank measurements show no signals except for m/z = 2, which are caused by the layered design of the extremely complex STM sample holder. This contribution is proportional to the sample temperature and can therefore be eliminated with the fit routine mentioned before. The other TPD traces are only treated with the Shirley background algorithm, that accounts for the accumulation of the species inside the Feulner cone. The linear background correction with time is not used within this thesis, but helpful for screening experiments performed late in the day with accumulated species in the backpressure.

4.4. Quantification of TPD spectra

For quantification of the TPD peaks, the exact knowledge of the relationship of an at first arbitrary TPD signal and the desorbed amount of molecules is needed. The peak areas are determined via numerical trapezoidal integration of the background corrected data points $S(t)$ over time.

$$\int_{t_1}^{t_2} S(t)dt \approx \frac{t_1 - t_2}{2N} \sum_{k=1}^{N} (S(t_k) + S(t_{k+1})) \tag{4.3}$$

It is known from literature that on Rh(111) 1 ML corresponds to $1.58 \cdot 10^{15}$ sites/cm^2 [83]. Therefore the (2×1) - O and (1×1) - D superstructures on Rh(111) are used to calibrate the TPD signals in the following.

4.4.1. Rh(111) - (2 × 1) - O

Exposure of Rh(111) to O_2 at room temperature under clean conditions leads to the formation of a (2×1) - O superstructure, which was confirmed by low energy electron diffraction (LEED) and STM measurements [84, 85, 86]. The other existent (2×2) - O superstructure only forms below 280 K or at substochiometric dosages [84, 86]. The amount of oxygen corresponds to a coverage of 0.5 ML [86]. With an initial sticking probability of 0.2, a saturation exposure of 10 L should be sufficient to form the superstructure [86]. The oxygen desorbs around 900 K (234 kJ/mol) following second order desorption kinetics [87]. This method did not work, but is described for completeness.

The carbon content of the Rh(111) single crystal has to be depleted, since the crystal has been used prior as a template for graphene film formation. Therefore the standard cleaning procedure consisting of 3 consecutive sputter/annealing cycles, see section 3.1, together with an additional oxygen treatment is performed. Here the single crystal is cycled at $2 \cdot 10^{-7}$ mbar O_2 6 times for 10 min at 700 K followed by a dwell time of 5 min at 1173 K. Directly after the last cycle the sample is cooled down to room temperature, while still dosing $2 \cdot 10^{-7}$ mbar O_2. The Rh(111) - (2×1) - O superstructure is confirmed by STM measurements illustrated in figure 4.5.

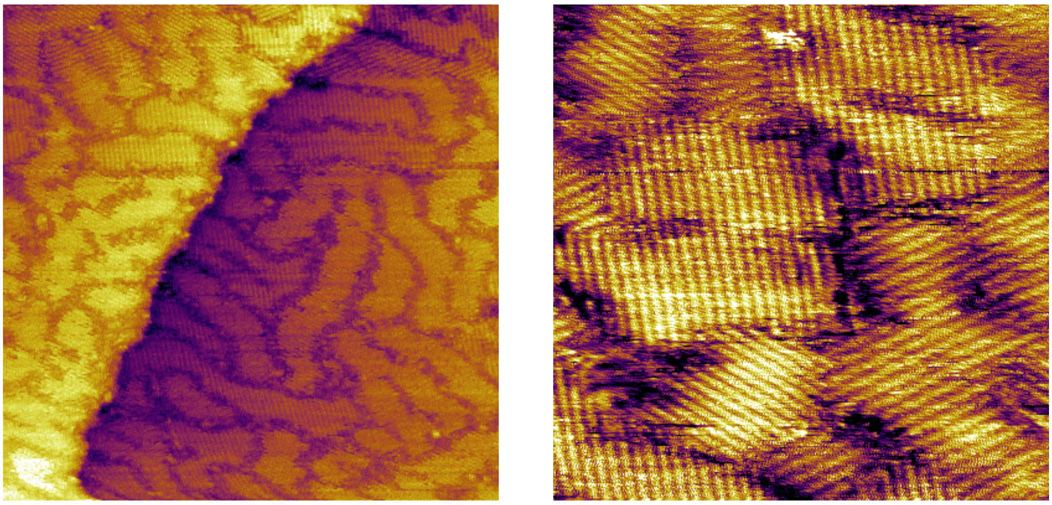

(a) [1 nA, -0.6 V, 100 × 100 nm^2]

(b) [1 nA, -1.3 V, 20 × 20 nm^2]

Figure 4.5.: STM measurements of the Rh(111) - (2 × 1) - O superstructure.

The three domains of the Rh(111) - (2 × 1) - O superstructure, rotated by 120° with respect to each other, are clearly discernible in the STM image in figure 4.5b. The oxygen atoms sit on the threefold hollow sites of the single crystal [86]. Such a structure is not found by H_2 or CO adsorption.

TPD measurements, illustrated in figure 4.6, with 2 K/s are performed right after the STM measurements and show a significant CO formation instead of the expected desorption of O_2. The intensity fluctuations in the desorption signals are caused by non-optimal PID settings for the temperature control.

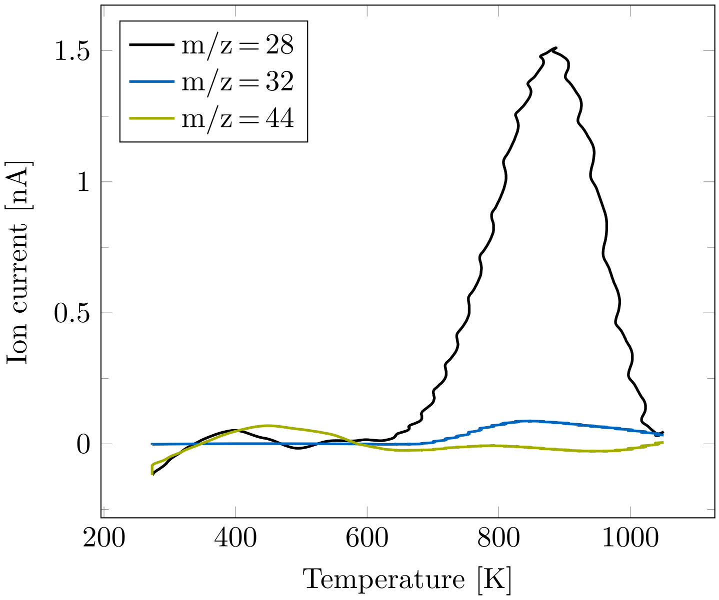

Figure 4.6.: TPD spectrum of Rh(111) - (2 × 1) - O.

This finding leads to the assumption that carbon segregation from the bulk still takes place while heating up. The CO desorption signal on clean Rh(111) is expected at 500 K [88]. However the measured desorption peak for m/z = 28 is detected at 900 K, which is the desorption temperature for Rh(111) - (2 × 1) - O [89, 87]. This indicates that the desorbing CO is formed by reaction of oxygen with remaining carbon in the Rh(111) single crystal. Thus the carbon content in the Rh(111) single crystal could not be depleted enough and the desorption of the (2 × 1) - O structure is not reasonable to calibrate the TPD setup. The oxygen almost reacts quantitatively to CO. TPD measurements without the carbon depletion procedure lead to additional desorption peaks at 160 K, 400 K, 900 K and 1000 K.

4.4.2. Rh(111) - (1 × 1) - D

After the unsuccessful calibration the the (2 × 1) - O superstructure on Rh(111) due to residual carbon impurities of the single crystal, another attempt is performed with the (1 × 1) - D structure, which is well known from LEED and helium scattering studies [90, 91, 92]. This structure is formed by dissociative adsorption of D_2 at 160 K, which takes places at the fcc threefold hollow site, as determined by LEED intensity analysis [92]. Furthermore, nuclear reaction analysis (NRA) shows a saturation coverage of 0.84 ± 0.12 ML, explained by the hindrance of dissociative adsorption close to a fully saturated surface [92]. In this work, D_2 is used instead of H_2, to lower the background contribution and to enhance the S/N. A saturation coverage of 1 ML is assumed for the calculations.

The preparation of the (1 × 1) - D structure on Rh(111) is realised as follows. The single crystal is sputtered at room temperature for 10 min and subsequently annealed in $2 \cdot 10^{-7}$ mbar O_2 at 973 K for 10 min for carbon depletion. Subsequently the sample is flashed to 1253 K, to remove adsorbed O_2 from the surface. A fast cool-down minimizes carbon segregation from the bulk. This procedure is repeated 3 times. Finally the (1 × 1) - D structure is formed by exposure of the Rh(111) single crystal directly after the last flash to $1 \cdot 10^{-5}$ mbar D_2 during cool-down.

The TPD spectra are performed with 2 K/s in the temperature range from 130 K to 550 K and lead to a broad desorption signal between 200 K and 400 K with a peak maximum at 275 K. An exemplary TPD spectrum is illustrated in figure 4.7. The peak position and width is in good agreement with literature [91].

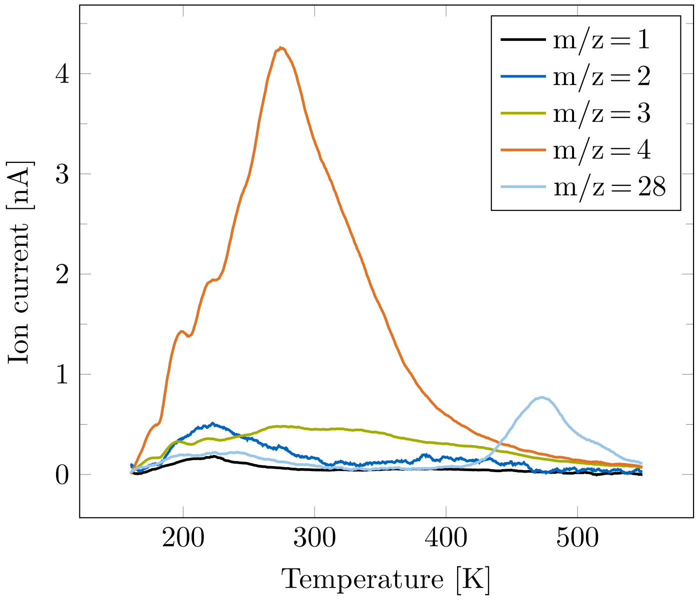

Figure 4.7.: TPD spectrum of Rh(111) - (1 × 1) - D.

The major peak with m/z = 4 belongs to D_2, but also small amounts of HD and H_2 are detected with the respective traces with m/z = 2 and 3. The H_2 originates from the background of the UHV chamber and HD is formed by recombination of dissociatively bound H_2 and D_2. Furthermore, a small amount of m/z = 28 is detected at 475 K, which can be assigned to carbon monoxide from the UHV background, as is in good agreement with literature [88]. Experiments dosing D_2 at 130 K showed the same signals, but higher amounts of H_2 and CO. A cool-down in D_2 reduces the background contribution of those species.

The desorption signals in the temperature range from 160 K to 550 K are considered for the calibration. In addition to the the main signal with m/z = 4, the traces of m/z = 2, 3 and 28 are also taken into account, to correct for adsorbed species from the UHV background. The fragmentation patterns for the respective gases are listed in table 4.1. It is assumed that HD and D_2 show the same fragmentation pattern as H_2.

Table 4.1.: Fragmentation patterns for H_2, HD, D_2 and CO for the RGA 200 [93].

m/z	1	2	3	4	28
H_2 [%]	4.76	95.24	-	-	-
HD [%]	2.38	2.38	95.24	-	-
D_2 [%]	-	4.76	-	95.24	-
CO [%]	-	-	-	-	91.58

Furthermore, the device specific sensitivity of the detection system, consisting of a quadrupole and an electron multiplier, has to be taken into account for the calibration of the modified TPD setup. The applied sensitivity factors, listed in table 4.2, are provided from the manufacturer of the mass spectrometer and normalised to be 1.0 for N_2. The sensitivity factor of HD is assumed to be in between of H_2 and D_2.

Table 4.2.: Sensitivity factors for H_2, HD, D_2 and CO [93].

Gas	Sensitivity factor
H_2	0.46
HD	0.41
D_2	0.35
CO	1.05

For the calibration of the TPD setup, first the peak areas for the traces with $m/z = 2$, 3, 4 and 28 are determined, which correspond to the respective main signal components for H_2, HD, D_2 and CO. Subsequently these areas have to be fragmentation corrected. In the case of $m/z = 2$ the share with the fragments of HD and D_2 are subtracted and then corrected for the fragmentation. Then the areas are set in relation to N_2 with the respective sensitivity factors in table 4.2.

Still the small amounts of carbon monoxide adsorbed from the UHV background have to be taken into account. CO forms different structures on Rh(111), which are the (2×2), the split (2×2) or the $(\sqrt{3} \times \sqrt{3})R30°$ [89]. If one assumes that every CO molecule blocks two binding sites on the Rh(111) surface and therefore two deuterium atoms forming one D_2 molecule, each CO molecule can be seen as an equivalent to a D_2 molecule. Further calculations are carried out with this assumption. The possible error by misconception is rather small, since the CO signal is only 3% of the overall sensitivity corrected peak area. The step-by-step calculation is illustrated in table 4.3.

Table 4.3.: Calculation step-by-step for the calibration of the TPD setup.

Species	H_2	HD	D_2	CO
Integrated peak area [As]	$2.07 \cdot 10^{-8}$	$4.55 \cdot 10^{-8}$	$2.58 \cdot 10^{-7}$	$2.95 \cdot 10^{-8}$
Fragmentation corrected peak area [As]	$7.70 \cdot 10^{-9}$	$4.78 \cdot 10^{-8}$	$2.71 \cdot 10^{-7}$	$3.22 \cdot 10^{-8}$
Sensitivity corrected peak area [As]	$1.67 \cdot 10^{-8}$	$1.17 \cdot 10^{-7}$	$7.74 \cdot 10^{-7}$	$3.07 \cdot 10^{-8}$
Sum [As]	$9.38 \cdot 10^{-7}$			

The sum of all corrected peak areas is $9.38 \cdot 10^{-7}$ A and corresponds to the sensitivity corrected ion current of 1 ML of adsorbed deuterium atoms, that recombine to D_2. Thus the total ion current, assuming one molecule N_2 desorbing per binding site, is $1.88 \cdot 10^{-6}$ A. The top hat shaped single crystal with a diameter of 4.4 mm has $9.60 \cdot 10^{14}$ sites in total, so that each binding site leads to an sensitivity corrected N_2 ion current of $1.96 \cdot 10^{-21}$ A.

4.4.3. Graphene growth

Another experiment verifies the calibration described before: Ethene chemisorbs on Rh(111) with its C-C bond perpendicular to the surface as an ethylidine species between 230 and 250 K. LEED measurements show the formation of a (2×2) superstructure, depicted in figure 4.8 [94].

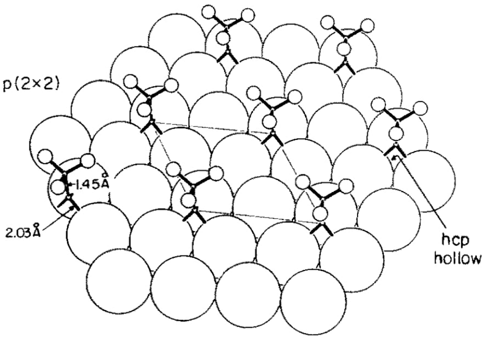

Figure 4.8.: Real space structure of the Rh(111) - (2×2) - C_2H_3 overlayer [95].

TPD experiments with 2 K/s lead to the polymerisation of the hydrocarons forming ultimately graphene [46]. The H_2 trace formed by the dehydrogenation of the hydrocarbons can then be used to verify the calibration results obtained with the Rh(111) - (1×1) - D superstructure.

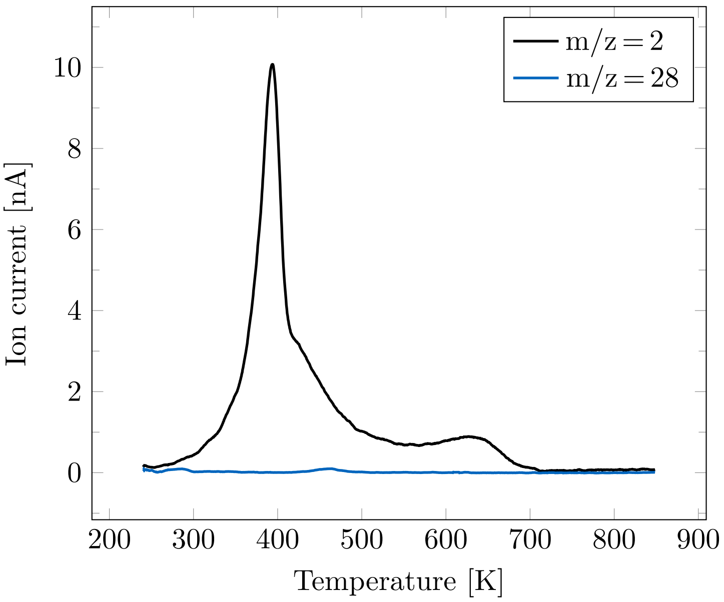

Figure 4.9.: TPD measurement of ethene saturated Rh(111) during graphene formation.

Figure 4.9 shows a TPD measurement performed after the adsorption of 12 L ethene on Rh(111) at 240 K. The (2×2) superstructure covers 0.25 ML with respect to the Rh surface atoms and each ethylidine species contains three cleavable hydrogen atoms. Thus, full dehydrogenation leads to the formation of 0.375 ML H_2 during the TPD experiment of Rh(111) - (2×2) - C_2H_3.

The small desorption signal caused by CO adsorbed from the UHV background is also taken into account. As pointed out above, CO forms $(\sqrt{3} \times \sqrt{3})$R30°, (2×2) or split (2×2) superstructures on Rh(111) [89]. It is assumed that every CO molecule blocks the binding site for one ethelydine species and therefore the formation of 1.5 H_2 molecules. The corrected peak area is $1.76 \cdot 10^{-6}$ As and differs only by 7% from the calibration with deuterium. This finding backs up the preceding calibration and gives an estimation for the accuracy of the modified TPD setup.

5. Reactivity of Pd clusters on h-BN/Rh(111)

The reactivity of Pd clusters supported on h-BN/Rh(111) can now be investigated systematically with the improved and calibrated TPD setup. The corrugated monolayer, on which the nanoparticles are deposited, is grown via chemical vapor deposition (CVD) on the Rh(111) single crystal. The h-BN builds a highly regular hexagonal superstructure on Rh(111) with a periodicity of 3.22 nm and pores of about 2 nm in diameter [58]. The moiré forms by the coincidence of 13×13 h-BN units on 12×12 Rh lattice spacings [61]. The clusters are trapped in the troughs of h-BN/Rh(111) and ripening is suppressed to a large extent [66, 45, 46]. On the nanomesh, each cluster has the same chemical environment and therefore integral measurements like the TPD experiments can be linked to local probes with the STM.

Integral measurements of cluster reactivities challenge the sensitivity of the modified TPD setup. The investigation of size-selected clusters requires low coverages of the nanoparticles. The nanoparticles show a transient mobility upon cluster deposition, leading inevitable to the formation of a certain amount of agglomerates that can be predicted by Poisson statistics. Thus, a cluster coverage of $\leq$5% of the moiré cells leads already to the formation of $\leq$2.4% of agglomerates [46]. Additionally keeping in mind that one moiré cell spans over 144 Rh atoms, the sensitivity of the modified TPD setup has to be at least 3 magnitudes higher for experiments with size-selected clusters compared to measurements on single crystals.

In the following, a fresh h-BN film is prepared for each measurement series and checked with the STM. Furthermore, the number of nanoparticles and their height distribution is monitored right after the cluster deposition and after each TPD measurement series to document the ripening behaviour of the nanoparticles under reaction conditions.

5.1. CO oxidation on $Pd_{\approx 19}$/h-BN/Rh(111)

The first experiments on the reactivity of Pd clusters with the modified TPD setup can be seen as proof of principle measurements. At that time, the detection limit of the apparatus is unknown, so that a familiar reaction with a high desorption yield in combination with a huge amount of clusters is investigated. Unselected $Pd_{\approx 19}$ clusters are investigated, which can be deposited faster in large amounts and thus leading to higher desorption signals. The unselected nanoparticles are generated by a special mode of the quadrupole mass filter, applying only the AC and no DC voltage. In this "RF only" mode the quadrupole acts as a high pass filter, theoretically allowing only particles above 7/9 of the selected mass to pass. In reality this value is closer to one, due to inevitable discrepancies between theory and practice [96, 97]. Additionally the bender of the cluster source operates as a notch filter depending on the settings. With the specific cluster source settings used, clusters from Pd_7 to Pd_{42} were able to pass the source. This means that in the case of unselected $Pd_{\approx 19}$, clusters in the range from Pd_{15} to Pd_{42} are deposited. In the proof of principle measurements, the unselected $Pd_{\approx 19}$ clusters are used as a catalyst for the well-known CO oxidation. The reaction is highly exothermic and achieves high yields, further simplifying the measurements. In the following TPD experiments investigating the coadsorption of O_2 and CO on $Pd_{N\approx 19}$/h-BN/Rh(111) are carried out and compared with literature. The CO oxidation is one of the most thoroughly studied reactions and follows a Langmuir-Hinshelwood mechanism [42, 98].

5.1.1. Literature

TPD and IRAS studies on the CO adsorption on Pd(111) show that weakly bonded linear or atop CO species desorb first, resulting in a broad TPD signal between 100 K and 300 K. With decreasing CO coverage, the remaining molecules occupy the more favorable bridge and threefold hollow sites, from which they desorb at 470 K on Pd(111) [99]. The CO oxidation on Pd(111) shows an even more complex dependence on the oxygen and carbon monoxide coverages. At moderate coverages, oxygen is compressed from a $p(2 \times 2)$ to a $(\sqrt{3} \times \sqrt{3})R30°$ structure, which reduces the activation energy from 105 kJ/mole to 59 kJ/mole [98]. Thus coverage dependent desorption signals for CO_2 are observed on Pd(111), ranging from 380 K to 490 K [42]. Additionally the underlying substrate has an influence. For example the CO desorption temperature is 70-100 K lower for single layer Pd(111) islands evaporated on a thin FeO(111) film grown on Pt(111) compared to Pd(111) [100].

The reactivity of evaporated Pd nanoparticles is even more complex than on single crystalline surfaces. Whilst the CO desorption behaviour is the same for Pd(111) and 27 nm Pd nanoparticles evaporated on alumina with a signal around 500 K, smaller 2.5 nm particles show a double peak structure with signals at 370 K and 470 K. Furthermore the CO adsorption capacity is reduced during repeated adsorption/desorption cycles due to CO dissociation and accumulation of surface carbon, which reduces the activation energy of the desorption state with higher binding energy [101]. Besides weaker bound CO adsorption states, the smaller particles are also more reactive concerning the CO oxidation. In molecular beam studies the 2.5 nm particles have an activation energy of 20 kJ/mole compared to 64 kJ/mole for Pd(111). Also a slower decrease in the CO_2 production is observed for the smaller Pd nanoparticles compared to Pd(111), which is explained by the reversible formation of subsurface oxygen [102].

The CO oxidation on Pt-group metals has long been considered as structure insensitive [7]. However, gas phase reaction kinetic measurements combined with first-principles calculations on Pd_2-Pd_7 show that the catalytic activity is tunable by changing the number of constituent atoms [103]. Furthermore, investigations on size-selected Au, Pt, Pd and Rh clusters with sizes ranging from 1-20 atoms supported on thin MgO(100) films grown on Mo(100) show structure sensitivity. CO combustion on Pd_8 clusters takes place below 300 K, whereas Pd_{13} and Pd_{20} react above 400 K. Furthermore the reactivity of Pd_8 is higher on defect-rich MgO(100) films and thus depending on the support [17].

5.1.2. Experimental procedure

20 L of O_2 are dosed at room temperature on $Pd_{\approx 19}$/h-BN/Rh(111) with a pressure of $5 \cdot 10^{-7}$ mbar. The thermal energy is sufficient to overcome the activation barrier for the O_2 dissociation [104]. Atomic oxygen blocks the binding sites for H_2 and thus the main component of the UHV background [105]. Additional 15 L of $C^{18}O$ are dosed with $1 \cdot 10^{-7}$ mbar after a cool-down to 130 K. The isotope-labeled $C^{18}O$ is used to distinguish from CO out of the UHV background. O_2 is dosed prior to $C^{18}O$, because the latter blocks the adsorption sites of O_2, but not vice versa [104]. After reaching a backpressure lower than $2 \cdot 10^{-9}$ mbar, the TPD experiments are carried out with 2 K/s in the temperature range from 130 K to 600 K, recording $m/z = 28$, 30, 32, 44 and 46. The desorption of O_2 is not investigated, which takes place around 800 K [106]. At these high temperatures the investigated cluster sizes show a pronounced ripening, making consecutive TPD experiments incomparable [45, 46]. A blank TPD temperature ramp is always performed directly before dosing the reactants to remove adsorbed gases.

5.1.3. Results

The sensitivity of the in-house modified TPD setup is sufficient to detect the $C^{18}O$ oxidation on $Pd_{\approx 19}$/h-BN/Rh(111). Two consecutive $C^{18}O$ oxidation measurements with the modified TPD setup are shown in figure 5.1. The quadrupole mass spectrometer changed the amplification twice during the TPD runs, because the h-BN/Rh(111) surface is almost completely covered with $Pd_{\approx 19}$ clusters and the CO oxidation has typically a very high yield. The intermediate regions are fitted and illustrated by dashed lines. This problem does not affect future TPD measurements, because the amount of nanoparticles will be less in the case for size-selected clusters.

The TPD experiments concerning the co-adsorption of O_2 and $C^{18}O$ on $Pd_{\approx 19}$/h-BN/Rh(111) show a desorption peak at 380 K for $C^{18}O_2$. The experiments are difficult to compare with literature in every detail. Many parameters as the CO coverage, the cluster-size, the support have an impact on the investigated reaction. The temperature range is in good agreement with CO oxidation experiments on Pd(111) [42].

The intensity ratio of m/z=44 to 46 is about 1/3. Thus roughly 1/3 of the CO_2 desorption signal arises from oxidized CO or adsorbed CO_2, both from the UHV background. Since the ratio of the m/z=28 and 30 traces is also about 1/3, the m/z=44 signal is most probably caused by oxidation of CO from the UHV background and only minor amounts of CO_2 are adsorbed. The m/z=44 trace for CO_2 formation with CO from the UHV background shows an additional signal with a magnitude of 50 pA at the very beginning of the temperature ramp, which is not existent for for m/z=46. This is most probably a contribution of the extremely complex STM sample holder, which contains small dead volumes due to the layered design and can therefore be neglected.

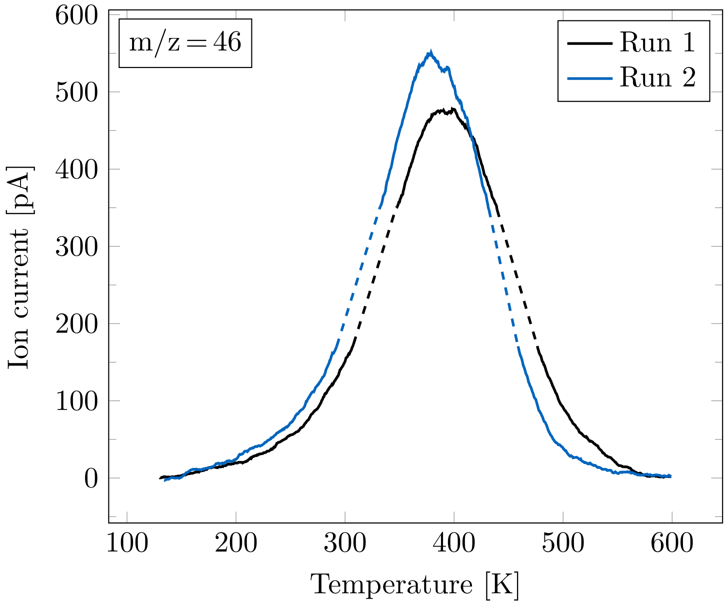

Figure 5.1.: TPD spectra of co-adsorbed O_2 [295 K, 20 L, $5 \cdot 10^{-7}$ mbar] and $C^{18}O$ [130 K, 15 L, $1 \cdot 10^{-7}$ mbar] on $Pd_{\approx 19}$/h-BN/Rh(111).

Blank measurements of the h-BN/Rh(111) surface without Pd clusters also show a low reactivity for the CO oxidation compared to measurements with $Pd_{\approx 19}$ clusters, as illustrated in figure 5.2. The reactivity increases with the number of TPD runs, as in the case with $Pd_{\approx 19}$/h-BN/Rh(111) samples. The peak integral of the second run reaches about 25% of the signal achieved with $Pd_{\approx 19}$ clusters, which means that most of the catalytic activity is still induced by the nanoparticles. The catalytic activity of the h-BN nanomesh on Rh(111) may be explainable by a progressive destruction of the film by O_2 or CO, so that the underlying Rh(111) surface can promote the oxidation. Theory predicts, in contrast to the inert free standing h-BN, that on h-BN/Ni(111) the adsorption of O_2 leads to an elongation of the O-O bond. This activated state of the O_2 molecule leads to a spontaneous formation of CO_2 with an incoming CO molecule in an Eley-Rideal mechanism, because CO adsorption on h-BN/Ni(111) is unfavourable [107].

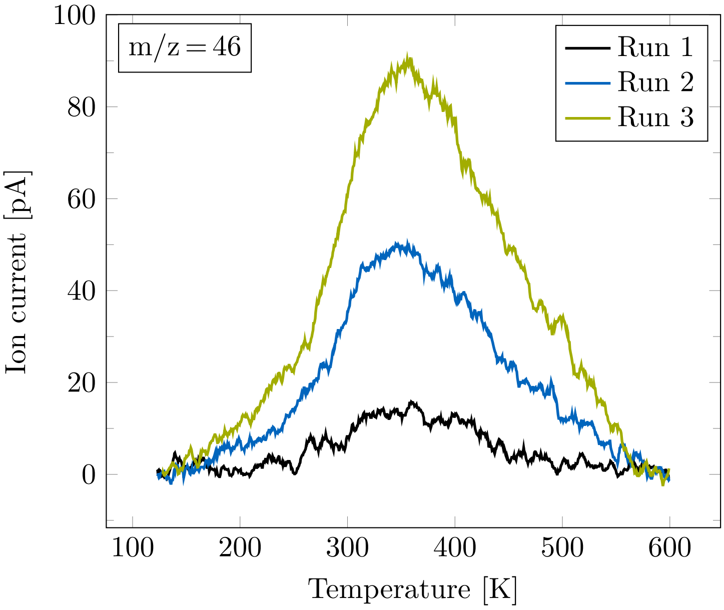

Figure 5.2.: TPD spectra of co-adsorbed O_2 [295 K, 20 L, $5 \cdot 10^{-7}$ mbar] & $C^{18}O$ [130 K, 15 L, $1 \cdot 10^{-7}$ mbar] on h-BN/Rh(111).

The peak position in figure 5.1 shifts to lower temperatures with consecutive TPD measurements. This finding is in agreement with literature, where the CO adsorption capacity is reduced on evaporated 2.5 nm Pd particles on alumina during repeated CO adsorption/desorption experiments due to CO dissociation and subsequent accumulation of surface carbon [101]. The measured catalytic activity rises with each run until saturation at run 2. This can be seen by an increase in signal intensity for $m/z = 46$ and a decrease of the CO desorption trace with $m/z = 30$. From there on, the catalytic activity remains unchanged. Various explanations could be possible for this observed behaviour:

Oxygen accumulation

While the desorption of CO on Pd(111) is complete until 500 K, oxygen species do not desorb until 800 K [99, 106]. The TPD experiments herein are performed in the temperature range from 130 K to 600 K and thus an accumulation of oxygen species takes place, which could be a possible explanation for the pronounced CO_2 production in consecutive TPD runs. This would indicate that the initial oxygen dosage is not sufficient to saturate the clusters. The high oxygen uptake could be explained by the reversible formation of subsurface oxygen, as already reported for 2.5 nm Pd particles evaporated on alumina [102].

Carbonaceous deposits

2.5 nm Pd nanoparticles on alumina show a decay of the CO adsorption capacity caused by accumulation of surface carbon in repeated adsorption/desorption cycles due to the dissociation of CO. This effect is only observed for 2.5 nm particles and not the case for 27 nm particles and Pd(111). The dissociation process occurs most probably at low coordinated sites, which are more likely on the surface of smaller particles [101]. The pronounced CO_2 formation may be explained by the oxidation of surface carbon species.

Cluster ripening

The increased CO_2 production could also be caused by cluster ripening processes. Pd_{19} clusters are known to ripen on h-BN/Rh(111) in the temperature range between 500 K and 700 K [45, 46]. Also a change in the morphology of the clusters may affect their catalytic activity, which is not easily understood. STM measurements before and after a TPD measurement series are depicted in figure 5.3. Both STM images have to be interpreted with caution due to the high cluster coverage. Figure 5.3a contains 677 visible clusters. Though, taking into account the measured cluster current during the cluster deposition, 2070 clusters should be located on the 100×100 nm^2 surface area. This means that either the clusters are stacked in multilayers or merged together after deposition. Most probably both scenarios have taken place, since bigger agglomerates as well as various layers can be distinguished. This becomes even more reasonable, since there are only 965 moiré cells expected per 100×100 nm^2 surface area. Figure 5.3b contains only 415 clusters. The nanoparticles appear bigger than before, which leads to the assumption that a further agglomeration of the nanoparticles has taken place.

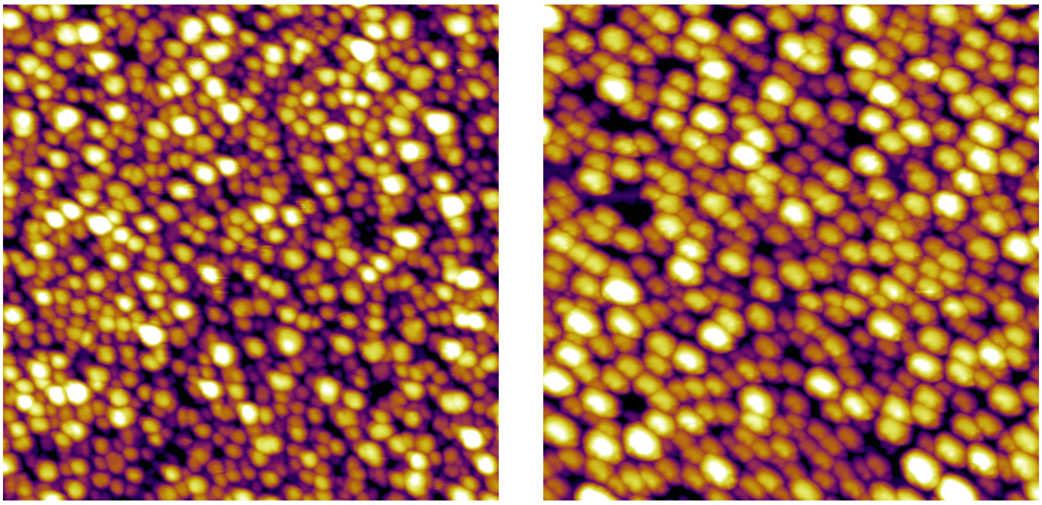

(a) [1 pA, -0.6 V, 100 × 100 nm^2] (b) [1 pA, -0.6 V, 100 × 100 nm^2]

Figure 5.3.: STM images before (a) and after (b) a TPD measurement series.

5.2. Co-adsorption of D_2 and C_2H_4 on Pd_{19}/h-BN/Rh(111)

After the first experiments with the modified TPD setup, investigating the CO oxidation on $Pd_{\approx19}$/h-BN/Rh(111), further studies focus on the more elaborate co-adsorption of D_2 and C_2H_4 on size-selected Pd_{19} clusters. In order to ensure the size-selectivity of the Pd_{19} clusters, the particle density has to be reduced by one magnitude in comparison to the preceding measurements with unselected $Pd_{\approx19}$. Thus only 20% of the moiré cells are occupied with a cluster, which is less than 0.15% with respect to the Rh surface atoms. The low cluster coverage represents a sensitivity challenge for the modified TPD setup.

5.2.1. Literature

Ethene adsorbed on Pd(111), Pd(100) and Pd(110) single crystal surfaces desorbs with two features in TPD measurements, a main desorption peak around 300 K with a small shoulder at 220 K [108, 109, 110]. The main component desorbs with an activation energy of 80 kJ/mol at low coverages on Pd(111), but strong intermolecular lateral interactions reduce the desorption temperature gradually at higher coverages [111]. 40 L of ethene are necessary to saturate the Pd(111) surface at 300 K [111]. TPD experiments with C_2H_4 on evaporated Pd nanoparticles with a mean particle size of 2.5 nm on Al_2O_3/NiAl(110) show similar desorption features, as depicted in figure 5.4, though the main desorption signal is at 220 K.

C_2H_4 adsorbs at low temperatures in two geometries, π-ethene and the stronger bound di-σ-ethene. The π-ethene desorbs intact at 220 K, whereas the di-σ-ethene can either desorb intact at 300 K or dehydrogenate above 550 K, producing carbonaceous deposits. After a number of TPD cycles, the carbon containing species block the active sites for the dehydrogenation reaction and ethene desorbs predominantly intact [112].

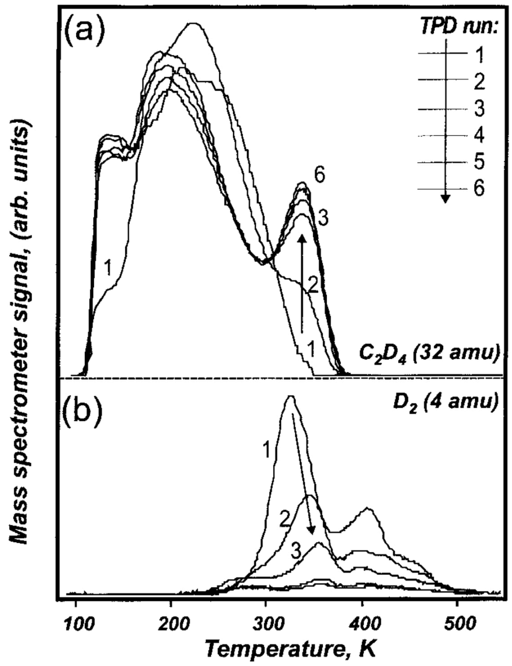

Figure 5.4.: Consecutive TPD spectra after adsorption of 1 L C_2D_4 at 100 K on Pd nanoparticles supported on Al_2O_3/NiAl(110) with a mean particle size of 2.5 nm [112].

The ratio of π- and di-σ-ethene is dependent on the particle size, which makes this an attractive system to be investigated with size-selected clusters. Di-σ-ethene is predominantly formed on single crystals or larger particles [43]. XPS measurements of the Pd 4d state show, that the Fermi energy of the Pd particles moves upward in energy with increasing particle size. Therefore the donation of electrons from the metal to the antibonding π^*-orbital of ethene is enhanced with increasing particle size. The result is a weakening of the C=C double bond. Thus, the sp^3-hybridisation is more favoured on bigger particles than the sp^2-hybridisation, which means a gradual transition from π-ethene to di-σ-ethene is occuring [113]. Additionally, the development of more extended facets on the larger particles favours the formation of di-σ-bonded ethene [43].

Experiments with 1.5 L C_2H_4 dosed at 133 K on unselected $Pd_{\approx 38}$ clusters supported on h-BN/Rh(111) show similar features with the modified TPD setup, as illustrated in figure 5.5. The two desorption signals at 190 K and 330 K can be attributed to π- and di-σ-ethene. Furthermore, the weaker bound π-ethene signal is the main desorbing component, in accordance with evaporated Pd nanoparticles on Al_2O_3/NiAl(110) [112].

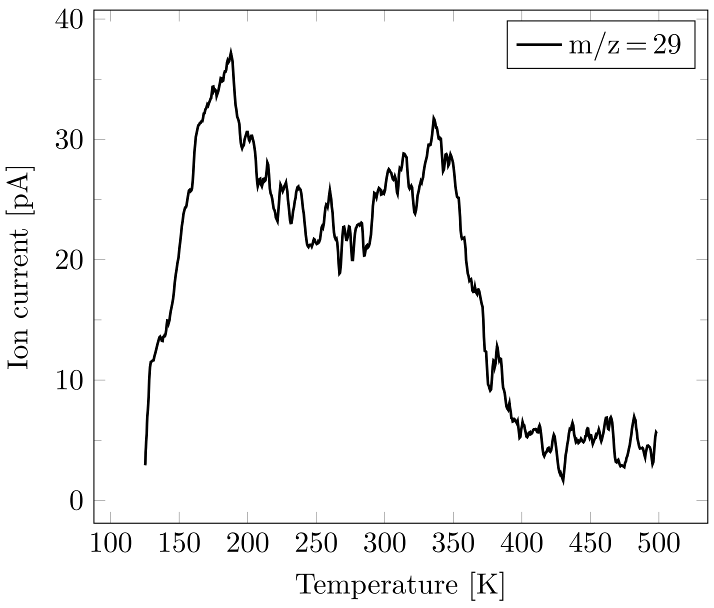

Figure 5.5.: TPD spectrum of C_2H_4 [133 K, 1.5 L, $1 \cdot 10^{-7}$ mbar] on $Pd_{n\approx38}$/h-BN/Rh(111).

Di-σ-bonded ethene on Pd(110) undergoes self-hydrogenation in small amounts above 300 K, meaning the reaction of ethene with hydrogen adatoms produced by dehydrogenation of other ethene molecules. The ethane formation can be increased by a factor of 50 with a pre-coverage of Pd(110) with H_2 [110]. Ethane is predominantly formed by reaction with π-bonded ethene [111]. The addition of the first hydrogen atom to ethene, which forms an ethyl species, is the rate-limiting step [114].

Furthermore, C_2H_4 undergoes extensive H-D exchange on D_2 pre-adsorbed Pd(111), whereas only small amounts are fully hydrogenated to $C_2H_4D_2$. Despite the D_2 pre-coverage on Pd(111), a small amount of C_2H_4 is still dehydrogenated [44]. 1-alkenes, including ethene, undergo efficient H-D exchange reactions below 300 K on Pd(100) and Pd(111) on all C-H bonds, but again next to no alkane formation is observed. The stronger bound di-σ-ethene is the precursor for the H-D exchange reaction of ethene, as found on Pd(100) and Pd(110) [115, 110]. It is proposed that the H-D exchange reaction occurs via the reversible hydrogenation of the adsorbed alkene to a half-hydrogenated intermediate. Due to the stronger metal-hydrogen bond on Pd than on other catalytically active metals, the further hydrogenation of the half-hydrogenated intermediate is prevented [115, 116]. Less than 1% of the adsorbed ethene reacts with the pre-adsorbed hydrogen on Pd(111) [111].

The ethane formation takes place with even higher yields on hydrogen precovered Pd nanoparticles evaporated on Al_2O_3/NiAl(110) and around 80 K lower in temperature compared to studies on single crystals. Furthermore the hydrogenation and dehydrogenation reactions proceed more readily than on the single crystal surfaces [43]. Hydrogen pre-coverage favours the formation of π-bonded ethene on Pd(111) and Pd nanoparticles evaporated on Al_2O_3/NiAl(110). The proportion of π-bonded ethene increases with the hydrogen coverage, because the formation of di-σ-ethene is inhibited by hydrogen adatoms sitting in the hollow sites and sterically hindering the di-σ-bonding [43, 117, 111]. Thus, the more weakly π-bound ethene is favoured on the residual top-sites [43]. It has been proposed that the formation of weakly bound subsurface hydrogen is the key factor to promote the hydrogenation reaction, which is enhanced in the case of the nanoparticles [118, 44]. However, the discrimination of surface and subsurface hydrogen is not straightforward by TPD measurements, due to the very small energy differences between those two states, as calculated e.g. for Pd(111) [119].

Ethene adsorbed on Pd nanoparticles decomposes to some extent at elevated temperatures. The resulting carbonaceous deposits are preferentially formed on larger particles with several nanometers in size. In this case, the development of more extended facets favours the formation of di-σ-bonded ethene, shifting the reaction pathway to the dehydrogenation reaction [43]. Therefore, the reactivity of ethene depends on the particle morphology. It is noteworthy that only a few percent of a monolayer dehydrogenate on Pd(111) per TPD run, because the rate of the ethylene dehydrogenation is negligibly slow in UHV [120]. Nanoparticles with well-ordered (111) facets appear to be less active [43]. Local rearrangements of the nanoparticles at 400 K most probably lead to the formation of more extended facets, as when used directly after deposition at low temperatures [121, 122, 43]. The activity of Pd nanoparticles in the 1-3 nm range evaporated on Al_2O_3/NiAl(110) is independent on particle size [43]. Though, experiments with Pd nanoparticles supported on SiO_2 and TiO_2 at atmospheric pressures, illustrated in figure 5.6, show significant size-effects for the hydrogenation reaction of ethene [123].

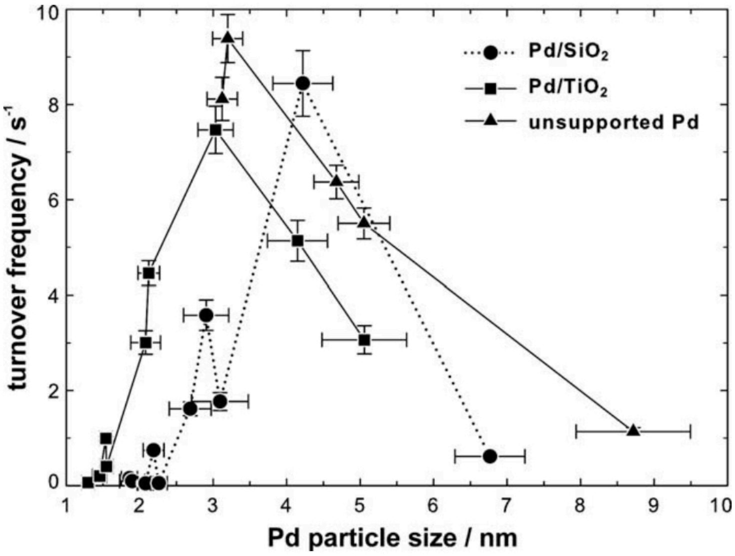

Figure 5.6.: Size-dependent ethene hydrogenation on Pd particles carried out at atmospheric pressures at a reaction temperature of 293 K with H_2 and C_2H_4 concentrations of 8.6×10^{-4} mol l^{-1} [123].

5.2.2. Experimental procedure

The experimental procedure described in the following is oriented on literature [43, 44]. 300 L of D_2 are dosed with $1 \cdot 10^{-5}$ mbar at 200 K, which is the onset temperature for the dissociative adsorption of D_2 on Pd. In this way the adsorption of H_2 from the UHV background is prevented during further sample cool down [124, 125, 126, 127]. D_2 is dosed prior to C_2H_4, because the latter blocks the binding sites for hydrogen [43]. A saturation of the clusters is ascertained by a high D_2 exposure of 300 L [128]. Deuterium atoms can migrate into the bulk upon dissociative adsorption, which is facilitated at elevated dosing pressures [129, 43]. In order to discriminate H/D exchange from hydrogenation reactions, supplemental experiments with H_2 instead of D_2 are performed. After a further cool-down to 130 K, additional 1.5 L of C_2H_4 are dosed with $1 \cdot 10^{-7}$ mbar on the D_2 pre-covered Pd_{19} clusters. Further experiments with exposures of 10 L C_2H_4 are performed, leading to higher desorption signals, but also longer waiting times to reach an acceptable backpressure of at least $2 \cdot 10^{-9}$ mbar before starting the TPD measurement in regard to the high sticking coefficient of ethene. This backpressure problem could not be improved by a reduction of the C_2H_4 dosing pressure below $1 \cdot 10^{-7}$ mbar. The experiments with 10 L of C_2H_4 show similar results, besides a higher signal intensity. It is noteworthy that C_2H_4 does not adsorb in multilayers on Pd particles [122, 43]. The TPD measurements are performed with a temperature ramp of 2 K/s in the range from 130 K to 500 K and the m/z = 2/4, 28, 29, 30, 31 and 32 traces are recorded. The m/z = 2 and 4 are chosen for the respective experiments with H_2 and D_2. A blank TPD run is always carried out prior to the gas exposures to remove adsorbates from the UHV background. Table 5.1 lists the fragmentation patterns for C_2H_4 and C_2H_6, as provided from the manufacturer of the mass spectrometer [93]. The numbers for $C_2H_4D_2$ are only a crude approximation based on the assumption that H and D detach with the same probability.

Table 5.1.: Fragmentation patterns for C_2H_4, C_2H_6 and $C_2H_4D_2$ for the RGA [93].

m/z	26	27	28	29	30	31	32
C_2H_4 [%]	23.98	25.15	38.68	0.85	-	-	-
C_2H_6 [%]	10.87	15.60	47.28	9.93	12.29	-	-
$C_2H_4D_2$ [%]	4.82	8.92	13.24	28.34	22.22	6.62	12.29

5.2.3. Results

Prior to performing the first TPD experiments with size-selected clusters and the modified setup, the monodispersity and cluster density has to be confirmed via STM measurements. In the following, Pd_{19} clusters supported on h-BN/Rh(111) are investigated. Figure 5.7 shows an exemplary STM image measured straight after deposition with height histogram of the clusters.

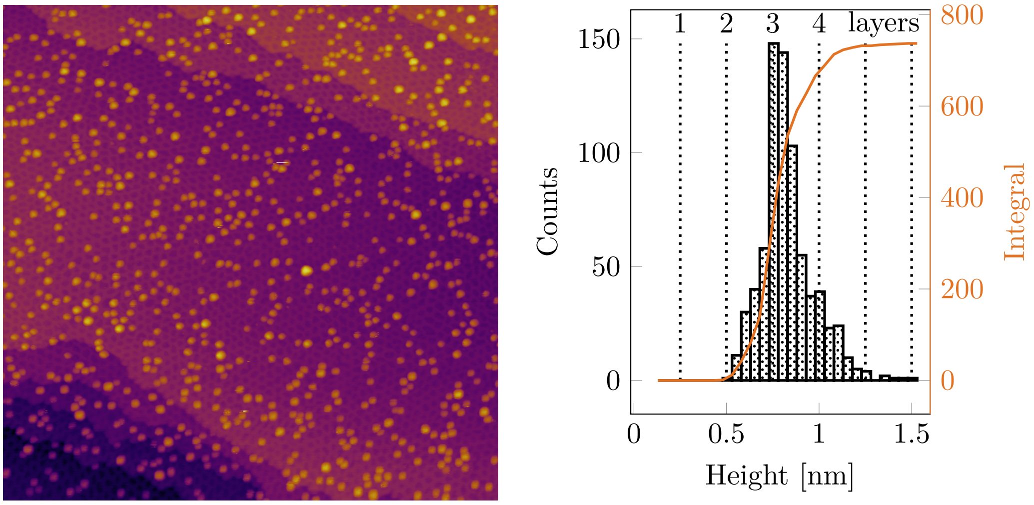

(a) [1 pA, -0.6 V, 200 × 200 nm^2]

(b) Corresponding height histogram

Figure 5.7.: STM image with height distribution of Pd_{19}/h-BN/Rh(111) before a TPD measurement series.

It can be easily seen that soft-landing conditions accompanied by size-selectivity of the clusters could be achieved, as already described in previous publications of this group [130, 45, 46, 51]. The 200 × 200 nm^2 STM image in figure 5.7 contains 830 clusters. The cluster density is decreased by one magnitude in comparison to the TPD experiments with unselected clusters. The individual height of the clusters is determined by removing the background around each particle and measuring the height profile on the maximum of the particle. An upshift of 1.3 Å in the height values is required to compensate the depth of the h-BN troughs, which is larger than the calculated corrugation of the moiré superstructure of 0.6 Å by using ab initio DFT. This discrepancy is supposed to be related to electronic effects [45, 59]. In the following, all cluster heights are corrected with this upshift. The majority of the Pd_{19} clusters is two layers high, but also some 3 layer clusters are present. Pd_{19} clusters are investigated, because their temperature dependent ripening behaviour on the h-BN/Rh(111) support is already well-known from previous work [45]. This enables the comparison of strictly temperature induced ripening with the ripening behaviour under reaction conditions during the TPD measurements.

It is still not known, if the sensitivity of the modified TPD setup is sufficient for the detection of the reaction products catalysed by a lower amount of size-selected clusters. Co-adsorption experiments with D_2 and C_2H_4 on Pd_{19}/h-BN/Rh(111) ultimately prove the usability of the device. Thus, the modification is a powerful tool to check for cluster reactivity. Figure 5.8 shows the m/z = 31 traces of 4 consecutive runs in a TPD measurement series. An evolution of the main desorption signal from 180 K to 330 K with increasing number of TPD cycles is observable.

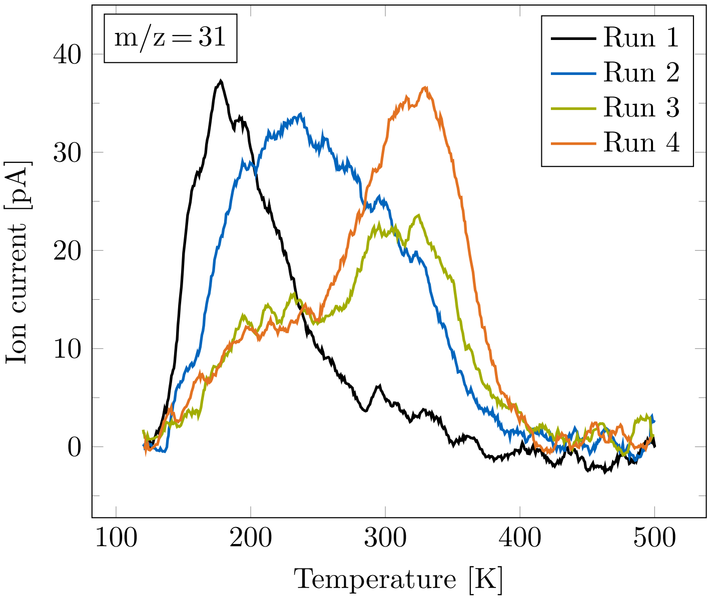

Figure 5.8.: TPD spectra of D_2 [200 K, 300 L, $1 \cdot 10^{-5}$ mbar] & C_2H_4 [130 K, 10 L, $1 \cdot 10^{-7}$ mbar] on Pd_{19}/h-BN/Rh(111).

Co-adsorption experiments on bare h-BN/Rh(111) with 300 L of D_2 and 1.5 L of C_2H_4 show next to no catalytic activity for ethene, see figure 5.9. There is only little sample holder contribution at the very beginning of the TPD ramp for m/z = 4, which is again inevitable due to the complex sample holder design. The main desorbing component is unreacted D_2.

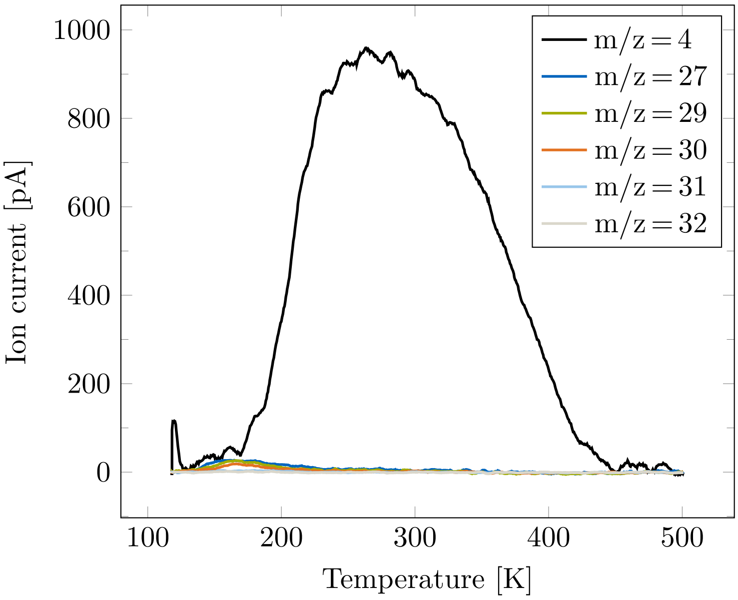

Figure 5.9.: Blank TPD spectrum of D_2 [200 K, 300 L, $1 \cdot 10^{-5}$ mbar] & C_2H_4 [130 K, 1.5 L, $1 \cdot 10^{-7}$ mbar] on h-BN/Rh(111).

In the following, the reactivity of Pd_{19}/h-BN/Rh(111) is further investigated concerning the co-adsorption of D_2 and C_2H_4 and compared with literature. In particular, the evolution of the main desorption signal during a TPD measurement series will be discussed.

Discrimination of H-D exchange and hydrogenation reaction

Possible reaction products in figure 5.8 with m/z = 31 can be either formed by hydrogenation or H-D exchange. Former studies with Pd nanoparticles evaporated on Al_2O_3/NiAl(110) show that the hydrogenation reaction occurs at 200 K in co-adsorption experiments with D_2 and C_2D_4 [43]. Further experiments on the same system with D_2 and C_2H_4 reveal H-D exchange reactions around 300 K [44]. In order to validate these findings for the investigated Pd_{19}/h-BN/Rh(111) system, 4 consecutive TPD experiments with alternating pre-coverages of H_2 and D_2 are performed. Figure 5.10 shows the respective m/z = 30 and 31 traces.

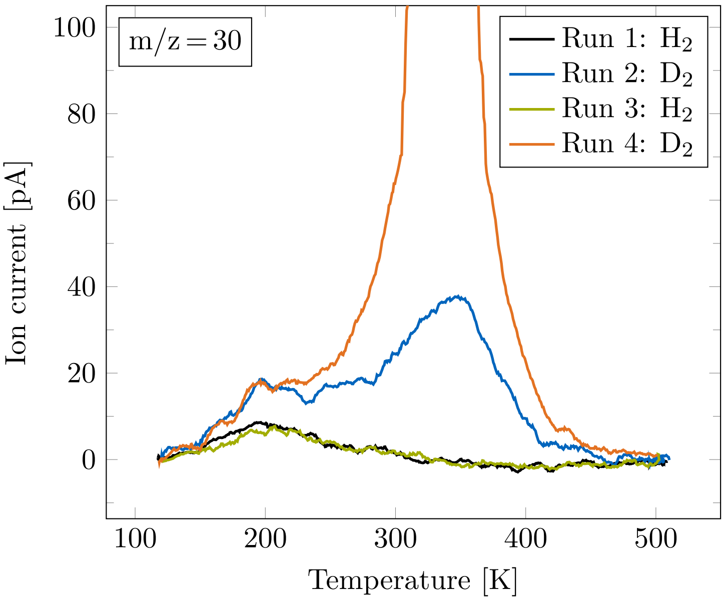

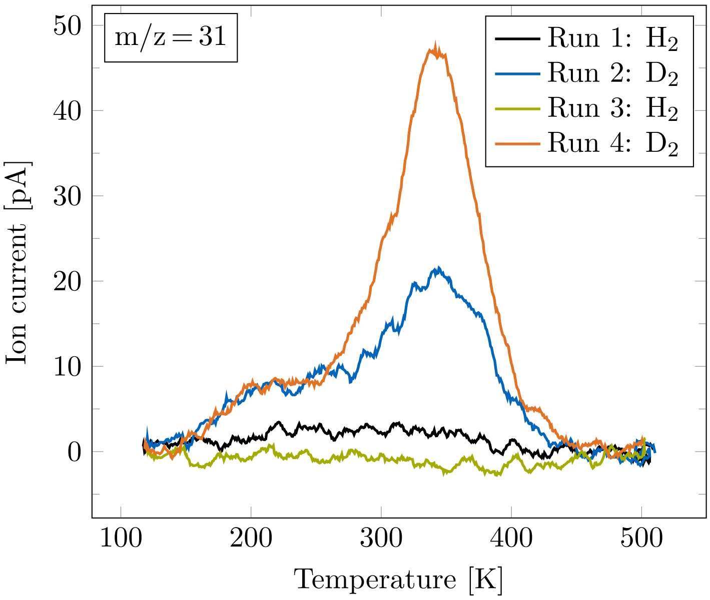

Figure 5.10.: TPD spectra with alternating co-adsorption of H_2/D_2 [200 K, 300 L, $1 \cdot 10^{-5}$ mbar] and C_2H_4 [130 K, 1.5 L, $1 \cdot 10^{-7}$ mbar] on the Pd_{19}/h-BN/Rh(111) system.

The m/z = 30 traces show the hydrogenation products C_2H_6 or $C_2H_4D^*$ at 180 K. It is noteworthy, that the signal intensity of the fully hydrogenated C_2H_6 in the case of H_2 pre-dosage is lower than the half-hydrogenated intermediate product $C_2H_4D^*$ with D_2. The desorption signal at 330 K could only be achieved with a pre-dosage of D_2, which is an evidence for the H-D exchange reaction to $C_2H_2D_2$. However, this signal could also relate to the half-hydrogenated intermediate $C_2H_4D^*$. This is nevertheless unlikely, because then the fully hydrogenated C_2H_6 for H_2 pre-covered Pd_{19} clusters should be formed as well to a low extent at 330 K.

In addition, no desorption signals can be detected for the m/z = 31 traces with H_2 pre-dosage. This is reasonable, because the fully hydrogenated C_2H_6 has only a mass of 30 amu and no H-D exchange can occur without the presence of deuterium atoms. This fact in combination with the varying signal intensities of the desorption signal at 180 K for the m/z = 30 traces, proves that the reaction occurring at 180 K is the hydrogenation. In the case of D_2 pre-dosage, the hydrogenation product $C_2H_3D_2{}^*$ as well as the H-D exchange product $C_2H_1D_3$ are detected. This further proves that the reaction occurring at 330 K is the H-D exchange. These findings are in good agreement with literature on evaporated Pd nanoparticles on Al_2O_3/NiAl(110) [43, 44].

Peak evolution

During a series with consecutive TPD measurements, illustrated in figure 5.8, the signal intensity for the hydrogenation reaction at 180 K decreases, whereas the desorption yield of the H-D exchange at 330 K increases. The position and signal intensity of the desorption peaks remain constant after 6 TPD cycles. A gradual deactivation of the catalytic activity concerning the hydrogenation reaction is also known of Pd particles in the size range from 1-1.5 nm supported on MgO [131]. The presence of carbon deposits, gradually formed in consecutive TPD runs by dehydrogenation of ethene, alters the catalytic performance of Pd nanoparticles evaporated on Al_2O_3/NiAl(110). The desorption signal of π-bonded C_2D_4 at 200 K changes only to a minor extent, whereas the intensity above 300 K for the di-σ-bonded C_2D_4 rises with increasing cycle number, as illustrated in figure 5.4. At the same time, the corresponding hydrogen evolution decreases, which leads to the assumption that the dehydrogenation of di-σ-bonded ethene above 300 K is gradually hindered by the increasing amount of carbonaceous deposits. However, the adsorption of ethene is not prevented by the dehydrogenation products. The carbon species block the highly coordinated sites and suppress the formation of hydrogen ad-atoms. Thus, the reactivity for carbon-covered Pd particles is significantly reduced, caused by the lower number of highly coordinated sites available on the surface for hydrogen ad-atoms. One should nevertheless also consider the possible steric effects of the carbon deposits on the hydrogenation reaction [112].

The highly coordinated sites on the Pd nanoparticles can also be blocked by CO, hindering the formation of hydrogen ad-atoms and therefore the dehydrogenation reaction [112]. This holds also for Pd_{19} clusters supported on h-BN/Rh(111), as illustrated in figure 5.11. The TPD experiments are performed after reaching a steady-state yield of the H-D exchange reaction. The CO does not react with the carbon deposits formed by dehydrogenation of ethene, as no further reaction products can be observed and the spectra could be reproduced many times as for Pd nanoparticles evaporated on Al_2O_3/NiAl(110) [112]. CO exposure after a dosage of C_2H_4 on D_2 pre-treated Pd_{19} clusters does not lead to a significant change in reactivity and implies that no further highly coordinated binding sites are required for the H-D exchange than the ones already occupied by C_2H_4 and hydrogen adatoms. However, a dosage of 10 L CO on the D_2 pre-treated Pd_{19} clusters prior to the exposure of C_2H_4 reduces the yield of deuterated products by a factor of 2. This can be understood by a blocking of the binding sites for C_2H_4. The H-D exchange reaction cannot be further inhibited by increasing the amount of CO to 100 L.

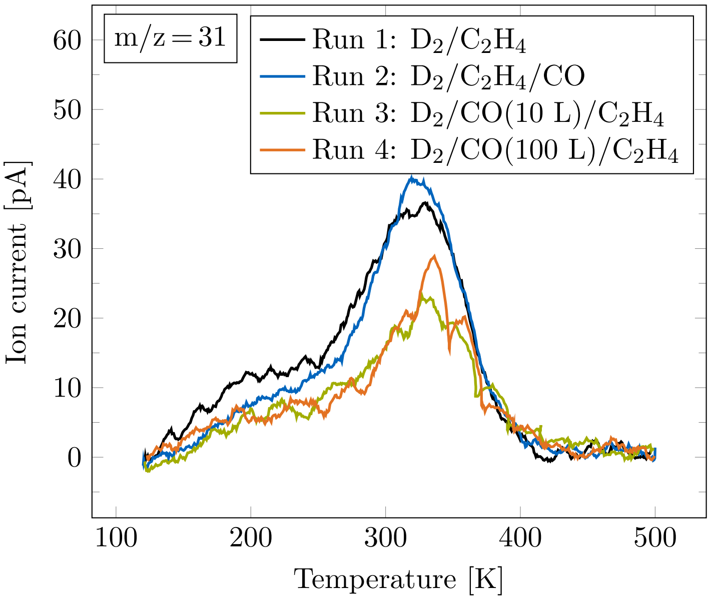

Figure 5.11.: Poisoning experiments using CO during co-adsorption experiments with D_2 [200 K, 300 L, $1 \cdot 10^{-5}$ mbar] and C_2H_4 [130 K, 1.5 L, $1 \cdot 10^{-7}$ mbar] on Pd_{19}/h-BN/Rh(111).

Cluster ripening

Complementing to the integral TPD measurements on the Pd_{19}/h-BN/Rh(111) system concerning the co-adsorption of D_2 and C_2H_4, also a microscopic characterization on the local scale is carried out to check if the change in reactivity is induced by ripening. For this purpose an additional STM image after a TPD measurement series with 13 experiments is shown in figure 5.12, together with the corresponding height histogram of the clusters.

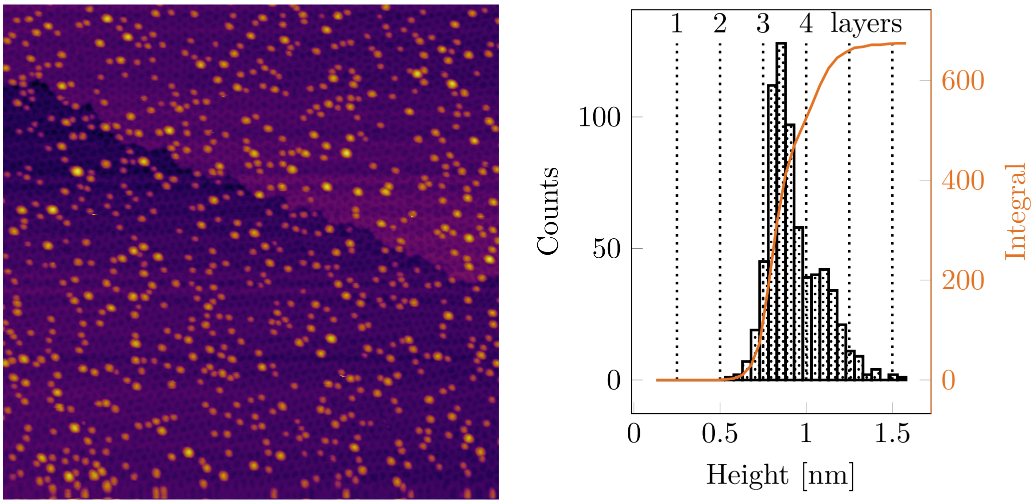

(a) [1 pA, -0.6 V, 200×200 nm^2]

(b) Corresponding height histogram

Figure 5.12.: STM image with height distribution of Pd_{19}/h-BN/Rh(111) after a TPD measurement series with 13 cycles.

This STM image can now be compared with figure 5.7, which belongs to the same TPD measurement series. Figure 5.12 contains 722 clusters compared to 830 clusters prior to the 13 TPD experiments. The decrease in the cluster density can be explained by subtle ripening processes, which become also visible in the height histogram by the development of a small shoulder for 3 layer clusters. However, the width and shape of the height distribution matches with annealing experiments to 500 K in our group [45, 46]. Therefore, it can be concluded that the stability of the Pd_{19} clusters on h-BN/Rh(111) is not affected by the repeated co-adsorption of D_2 and C_2H_4 in TPD experiments to 500 K. A pronounced ripening of the particles is not induced. In order to confirm this finding, a subsequent temperature induced cluster ripening is performed with the same sample. After annealing for 1 min at 700 K, the surface is again monitored by STM to investigate a potentially different ripening behaviour of the Pd nanoparticles due to the carbon deposits. Figure 5.13 shows the STM image with corresponding height histogram of the clusters.

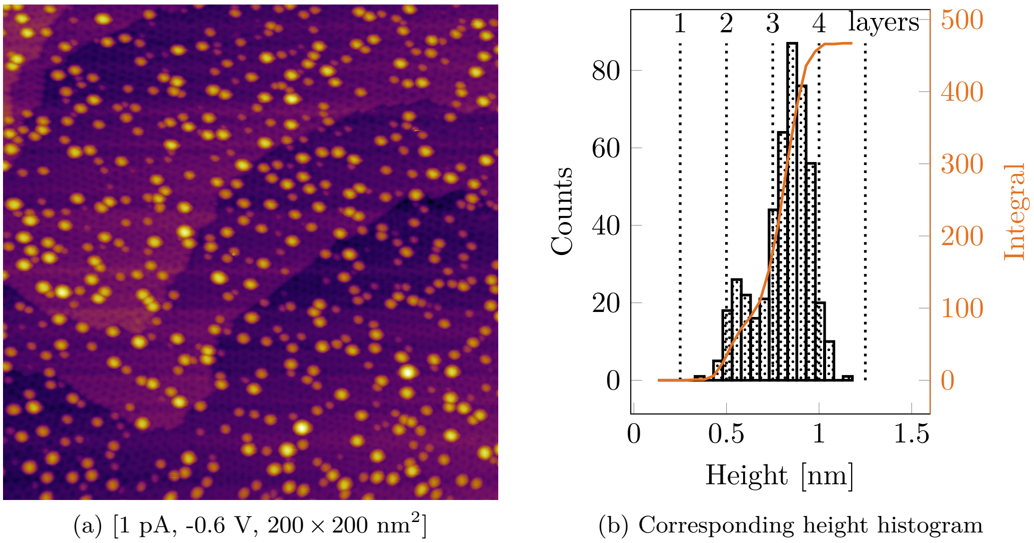

(a) [1 pA, -0.6 V, 200×200 nm^2]

(b) Corresponding height histogram

Figure 5.13.: STM image with height distribution of Pd$_{19}$/h-BN/Rh(111) after a TPD measurement series with 13 cycles and additional annealing for 1 min at 700 K.

The particle density decreased to 503 clusters per 200×200 nm^2 surface area after annealing for 1 min to 700 K. Moreover, the maximum of the height distribution shifted from 2 to 3 layer clusters. It is known from previous work that the strong interactions between cluster and support favour Ostwald ripening, the detachment of atoms from the clusters that subsequently diffuse on the surface and form by chance bigger clusters [45, 46]. This can be confirmed, because 1 atomic layer high clusters appeared after the annealing to 700 K. These findings are in agreement with the ripening behaviour of pristine Pd$_{19}$ clusters on h-BN/Rh(111) [45, 46]. Therefore, the carbonaceous deposits do not significantly alter the ripening behaviour of the Pd clusters.

6. FAST implementation

The catalytic activity of size-selected clusters can now be investigated in the present UHV chamber with the successful implementation of the modified TPD setup as described in chapter 4 and 5. While integral methods, such as the mentioned before, can help to screen temperature regimes of catalytic activity, the investigation of dynamics on the local atomic scale is particularly demanding. A high spatial and temporal resolution down to the milliseconds timescale have to be achieved. Only little is known about most of the underlying catalytic processes, especially for particles in the non-scalable size regime, as the investigated size-selected clusters. This also applies for dynamics accompanying catalysis, e.g. transport phenomena or structural changes of the nanoparticles. In addition to the integral measurements performed by TPD, local probes shall shed light on these issues. For this purpose, a conventional variable temperature STM is modified to investigate the clusters with enhanced temporal resolution at reaction conditions.

6.1. State of the art

The introduction of the STM by Binnig et al. in 1982 allows feasible real-space investigations in the nanoscale [132, 133, 134]. The principle of operation is to probe the interaction between a conductive sample surface and a sharp metal tip, while either of them is scanned laterally in the area of interest. By applying a bias voltage, electrons can tunnel through the vacuum barrier. The resulting tunnelling current is a function of tip position, bias voltage and local density of states (LDOS). The two main operation principles are the constant current and the constant height mode. In the first case, the tunnelling current is held constant by a feedback loop that alters the vertical position between the sample and the tip. In the latter only the variation of the tunnelling current is recorded. The main advantage of the high spatial resolution is diminished by the limited temporal resolution typically in the time scale of minutes per image. In the mid-1990s almost all components of the STM were well matched and pushed close to their limits. Any further improvement would entail the replacement of almost every system component.

Pioneering work by Bryant et al. in 1986 achieves images in real time with atomic resolution on highly ordered pyrolytic graphite (HOPG) in the constant height mode at line frequencies above 20 kHz [52]. Post processing of the images is necessary, because low resonance frequencies of the tip cause a phase shift of the scanning motion. Since then, the STM technology is pushed forward by several groups in order to generally increase the imaging rate [135, 136, 137, 138, 139, 140]. These high speed STMs are constructed with a rigid and compact design in order to achieve high mechanical resonance frequencies. In addition, high bandwidth I/V converters, fast A/D converters and prompt feedback electronics are used [141, 142]. The temporal resolution of 20 images per second achieved by Ludwig et al. in 1992 is often sufficient to investigate dynamics, especially if the measurement can be performed at low temperatures [136]. However, processes that require an activation energy cannot be slowed down by cooling. With the implementation of a hybrid mode between the constant height and constant current mode, the scan speed could be further increased up to 200 images per second in 2005 [143]. Only a handful of groups emerge in the field of high speed STM until nowadays. In the following a brief overview of their main achievements is given.

Besenbacher et al. measure dynamics in surface reconstructions on Cu(110) caused by reactions with O_2 [144] and discuss the diffusion of Pt adatoms, dimers and one-dimensional clusters on Pt(110)-(1 $\times$ 2) [145, 146, 147, 148]. The mobility of the Pt adatoms can be enhanced by the adsorption of H_2 [47]. Furthermore the diffusion of N adatoms on Fe(100) is investigated, where lattice distortions, caused by the presence of other strongly bound N adatoms, lead to an anisotropy in the diffusion behaviour. Meanwhile, the group constructs a fast-scanning, low- and variable-temperature STM [149] and also a fast-scanning high-pressure STM [150]. Moreover O_2 molecules are observed on TiO_2(110) in fast STM movies, diffusing in Ti troughs and jumping across OH defects [151, 152, 153].

Frenken et al. study step and kink dynamics on Au(110), Pb(111) and Ag(115) [154, 155, 156, 157, 158]. Moreover, indium atoms incorporated in Cu(001) are used as tracer particles for temperature dependent measurements of the mobility of surface vacancies [159, 160, 161, 162, 163, 164].

Wintterlin et al. investigate the diffusion of O atoms on Ru(0001) in real time [165, 166]. Furthermore, the co-adsorption phases of CO and O_2 on Pd(111) are measured with enhanced time resolution [167].

Magnussen et al. are focussing on high-speed electrochemical STM, studying dynamic processes on model electrodes. Transport phenomena like the addition or the removal of atoms at step edges on Cu(100) are investigated [168, 169, 170, 171, 172], as well as reconstructions of Cu(100) depending on potential and pH value during the hydrogen evolution reaction [173, 174]. In addition, the reconstructions on Cu(100) can also be formed by thiolates [175, 176, 177]. Sulfur atoms on Cu(100) show an enhanced mobility in the close vicinity of other sulfur adatoms [178, 179]. Quantitative studies of sulfur and methyl thiolate adsorbates on c(2 $\times$ 2)Cl covered Cu(100), Ag(100) and Au(100) investigate the influence of the chloride co-adsorbate layer on the adsorbate diffusion. Pb adsorbates on Cu(100) are studied in detail with enhanced time resolution [180, 181]. Moreover, the diffusion processes of Au atoms and Cl adlayers on Au(100)-(1 $\times$ 1) are also investigated [182, 183, 184, 185].

An alternative to the high speed STMs is the tracking mode, proposed in 1988 by Pohl and Möller, which enables a time resolution down to the millisecond with low currents and fast vertical feedback [49]. The first implementation of the tracking mode with a STM is realized by Swartzentruber in 1996 [50]. Additionally to the work of Swartzentrubers team, which focusses on the diffusion processes of Si atoms/dimers and SiGe dimers on Si(001) [186, 187, 188, 189] as well as Pd atoms on a Pd/Cu(001) surface alloy [190], other groups apply this technique to investigate Si dimers and hydrogen on the Si(001) surface [191, 192] and Si atoms on Si(111)-(7×7) [193]. Furthermore, this technique can also be used for tip control and drift compensation [194, 195, 196]. A high temporal resolution down to the millisecond can be achieved with the tracking mode. However, one of the biggest drawbacks of this technique is that only the feature of interest is investigated. Interactions with neighbouring species, that might influence the diffusion, cannot be recognized during the experiment. To ensure the interpretation of the investigated diffusion processes, it is important to additionally measure STM images with a high frame rate, where also changes in the surrounding surface area are captured [141].

The investigation of cluster dynamics during catalysis requires an enhanced temporal resolution compared to a standard STM. Therefore, the present variable temperature STM is modified by an add-on instrument to increase the temporal resolution to video rates and beyond. In the following, this is referred to as FAST, whose development is done in collaboration with the group of Africh and Comelli in Trieste together with Dri from ELETTRA [53, 54]. This add-on instruments enables high speed STM as well as tracking measurements. Hitherto, experiments with the FAST module enabled for example the investigation of the water formation on (10×2)-O/Rh(110) with a time resolution of 33 ms/image [197]. Furthermore, the graphene formation on Ni(111) and Rh(111) could be examined with a time resolution of up to 17 ms/image [198, 199, 46]. Additionally the diffusion of a Pd_{12} cluster on graphene/Rh(111) is observed with the Tracking technique [51].

6.2. Hardware

The commercial variable temperature STM system is expanded by an in-house built additional board, installed right before the last amplification stage with APEX PA141 operational preamplifiers. This enables the user to add voltages in the X- and Y-direction of the STM scanner piezo with two distinct filter options. One low pass input for slower AC voltages and a band pass filtered input for faster AC voltages in each direction. These filtered input signals are added symmetrically with opposite signs for quadrants facing each other on the piezo tube to the offset voltages controlled by the standard hardware of the variable temperature STM. This modification enables the fast motion in the X-Y plane.

The fast scan motion in X-direction is driven by a sinusoidal function and the slower Y-direction with a triangular shape. Higher Fourier components in the conventionally triangular shaped driving voltage could excite resonance frequencies of the STM. This can be avoided by using a pure sine wave as an excitation signal for the fast scan direction. Here, a smooth change between the forward and backward tip motion is preventing the excitation of higher harmonics [165, 53]. The waveform generation and signal acquisition is performed on the National Instruments FlexRIO platform together with the NI-6221 board and the the NI-5781 module. The first board is responsible for the generation of the triangular shaped driving voltages in the slow scanning direction and is capable to read-in a transistor-transistor logic (TTL) signal for controlling purposes. The latter is able to generate pure excitation sine waves in the fast scan direction and has a fast inline processing combined with a PXI-FPGA module. All National Instrument cards and modules are housed in a PXI-1033 chassis.

The standard Z-controller of the variable temperature STM is not fast enough to correct for an inclination of the sample in the fast scanning direction, if the tip moves in kHz range. Therefore, in parallel to the standard Z-regulator, an additional sine shaped AC voltage is added to the Z component of the piezo tube via an existing connection of the commercial system for an external Z voltage typically used for dI/dZ spectroscopy experiments. The superimposition of both sine modulations in X- and Z-direction results in a linear tip movement in space, inducing the tip to follow the sample inclination. The amplitude of the AC voltage in Z-direction controls the corrected slope. Additionally, the phase between the modulation in X- and Z-direction has to be fine adjusted, because of different path lengths in the electronics or weak resonance frequencies of the STM. This requires an adequate amplitude and phase of the AC voltage. In particular, the phase adjustment needs fine tuning at elevated scan frequencies, when the vicinity of scanner eigenfrequencies is reached.

Basically, it should be possible to measure at any desired scan speed with the FAST module. However, certain frequency ranges have to be avoided due to intrinsic eigenfrequencies of the commercial variable temperature STM. Figure 6.1 shows the characteristic resonance frequencies of the present system. The lock-in signal of the tunneling response during excitation sweeps in all scanning directions is plotted. Resonance frequencies in the X- and Y-direction lead to a distortion of the images, whereas disturbances in Z-direction introduce noise. Therefore, FAST measurements can be performed in off-resonant regions, for example below 800 Hz, but also around 1.1 kHz and 1.8 kHz. Besides, the preamplifier acts as an integrator, when the pixel frequency is higher than the bandwidth of 80 kHz. This phenomenon already shows up for 50 pixels with a scan frequency of 800 Hz in the fast scanning direction. Therefore, extensive studies with driving voltages at higher frequencies were not performed. The effect of the integrating preamplifier can be partially removed by calculating the gradient of the data points in the time domain.

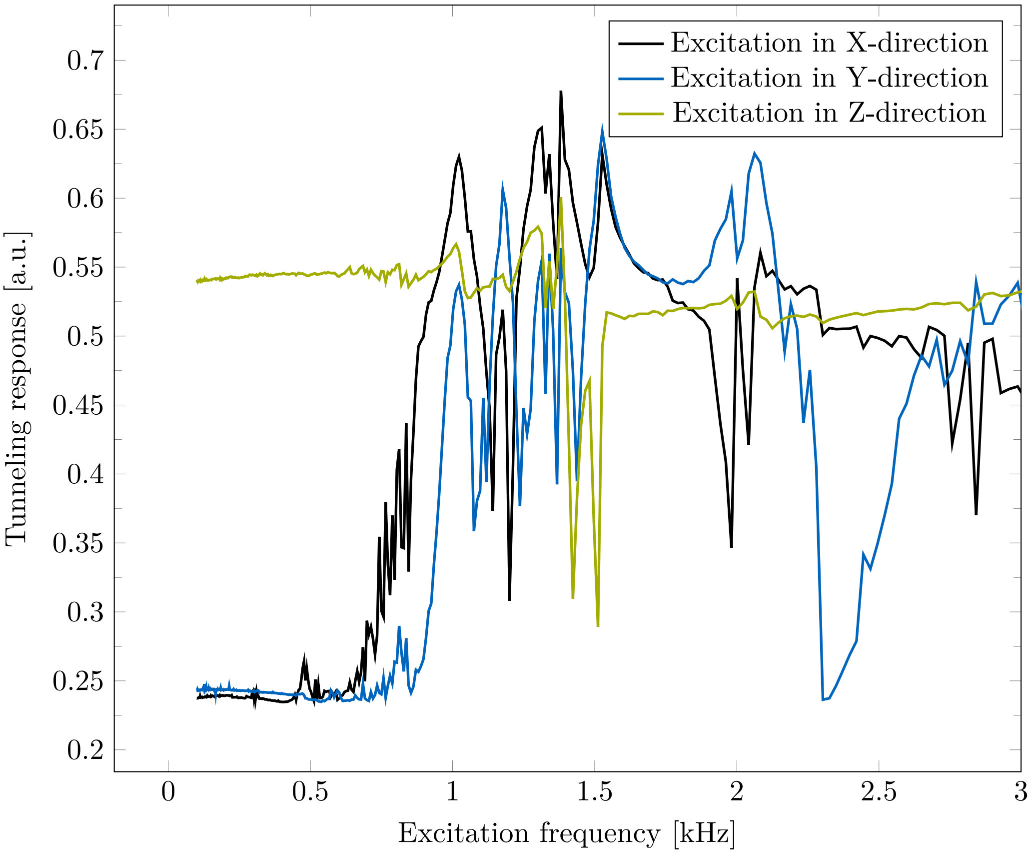

Figure 6.1.: Eigenfrequencies of the variable temperature STM.

The current signal is extracted from the commercial system directly after the last amplification stage PRE 4, which has a separate output IT MON for maintenance reasons. Using this separate buffered output leads to a significant noise reduction compared to a BNC T-piece prior to the A/D converter of the commercial STM. No filter options are built-in by default, because the IT MON output is typically used for troubleshooting purposes of the STM. However, the current signals read in by the commercial variable temperature STM are filtered by default prior the the A/D converter. To gain comparable data sets, the IT MON output of the PRE 4 has been modified to apply the same filter options as the commercial variable temperature STM for the read out of the current signals during FAST measurements. The filter options are dependent on the selected amplification factor of the PRE 4. The two possible options at the last preamplification stage are the 3.3 nA and 330 nA range with bandwidths of 800 Hz or 80 kHz respectively. The 330 nA range with a lower amplification factor has always to be selected for FAST measurements, because of the higher bandwidth of 80 kHz.

Subsequently, the exponential decaying current signals are transformed with a logarithmic amplifier into a linear scale and then digitized within the NI-5781 module. This logarithmic amplifier induces some noise, but equals the height sensitivity on the full height range. The connection diagram for the LabVIEW box with the commercial STM is depicted in figure 6.2. This box, which is controlled via LabVIEW and responsible for the FAST tip motions, the A/D converting and saving of the data, in combination with the additional board, can be considered as an add-on instrument that can drive commercial STMs in the FAST mode.

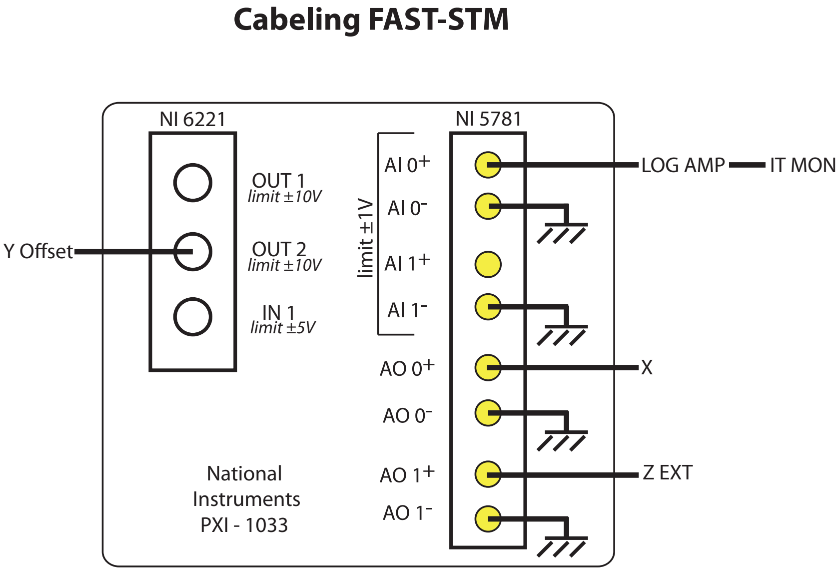

Figure 6.2.: Connection diagram for FAST measurements.

A typical FAST measurement starts with a slow scan of the sample surface with the conventional STM. The user then relocates the tip at the point of interest. The voltages at the scanner piezo tube for the X- and Y- direction are now static, whereas the Z-position is still regulated in the constant current mode. After defining the scanning parameters via a graphical user interface (GUI) in LabVIEW, including the frame rate and image dimensions, the phase in X-direction and the tilt compensation have to be set. Once the optimum setting is found, a switch back and forth between conventional STM and FAST measurements can be performed without readjustment. The procedure to optimize the parameters is described in the following section.

6.3. Software

The FAST experiments are controlled by a field programmable gate array (FPGA), which is accessible via a LabVIEW GUI depicted in figure 6.3, which was developed in collaboration with Giulia Troiano. The program is responsible for the data acquisition and the synchronized motion of the driving voltages.

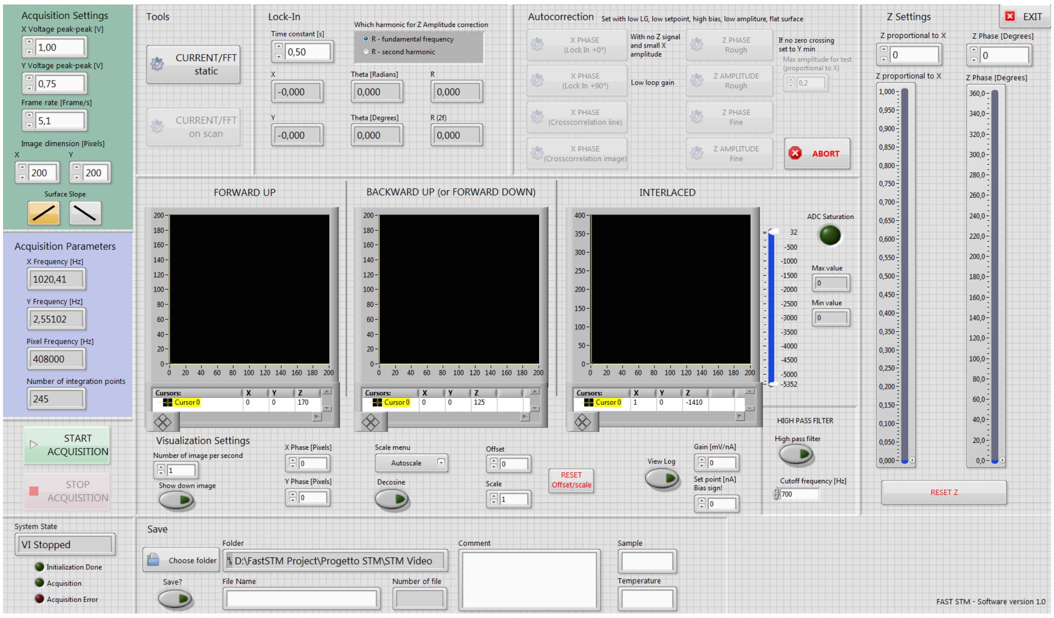
Acquisition Settings
X Voltage peak-peak [V]: 1,00
Y Voltage peak-peak [V]: 0,75
Frame rate [Frame/s]: 5,1
Image dimension [Pixels] X: 200
Image dimension [Pixels] Y: 200

Acquisition Parameters
X Frequency [Hz]: 1020,41
Y Frequency [Hz]: 2,55102
Pixel Frequency [Hz]: 408000
Number of integration points: 245

Lock-In
Time constant [s]: 0,50
Which harmonic for Z Amplitude correction: ● R - fundamental frequency ○ R - second harmonic
X: -0,000
Y: -0,000
Theta [Radians]: 0,000
Theta [Degrees]: 0,000
R: 0,000
R (2f): 0,000

Autocorrection Set with low LG, low setpoint, high bias, low ampliture, flat surface
With no Z signal and small X amplitude
Low loop gain
If no zero crossing set to Y min
Max amplitude for test (proportional to X): 0,2

Z Settings
Z proportional to X: 0
Z Phase [Degrees]: 0

FORWARD UP – Cursors: Cursor 0, X 0, Y 0, Z 170
BACKWARD UP (or FORWARD DOWN) – Cursors: Cursor 0, X 0, Y 0, Z 125
INTERLACED – Cursors: Cursor 0, X 1, Y 0, Z -1410

Max value: 0
Min value: 0

Visualization Settings
Number of image per second: 1
X Phase [Pixels]: 0
Y Phase [Pixels]: 0
Scale menu: Autoscale
Offset: 0
Scale: 1
Gain [mV/nA]: 0
Set point [nA] Bias sign!: 0

HIGH PASS FILTER
Cutoff frequency [Hz]: 700

System State: VI Stopped

Save
Folder: D:\FastSTM Project\Progetto STM\STM Video

Figure 6.3.: LabVIEW interface for FAST measurements.

The main parameters defining the FAST measurement are the AC voltages in X- and Y-direction, which specify the scan area. The frame rate in combination with the number of pixels per image in X- and Y-direction determine the pixel frequency for the A/D converter and the scan speed. The X- and Y-frequencies correlate with the frame rate by the following relationships.

$$\text{X-frequency} = \text{frame rate} \times \text{Y-dimension} \tag{6.1}$$

$$\text{Y-frequency} = \text{frame rate} \times 0.5 \tag{6.2}$$

Live images are displayed in the LabVIEW GUI, after initializing the FAST module, allowing an optimization of the scan parameters. Thus the user can choose whether to see forward and backward images of the up motion or the up and down images of the forward motion. There is an additional interlaced image displayed with alternating X-rows of the two selected images and therefore twice the pixel density in Y-direction. The latter facilitates the phase correction in X-direction. The following options only alter the appearance of the three displayed images in the LabVIEW program and do not change the raw data saved during the FAST measurements. The color range can be scaled automatically or set manually. The displayed data can be logarithmized digitally, when no logarithmic amplifier is used and there is also an option for digital high pass filtering. Moreover, the images can be corrected for the deformation resulting from the sinusoidal excitation voltage in the fast scanning direction. The various preview image options also help to adjust the amplitudes and phases of the driving voltages while scanning and define metadata, which are indispensable for the subsequent data treatment.

The magnitude and phase of the sinusoidal AC voltage added in Z-direction have to be optimized for the slope correction in the fast scanning direction. Therefore several algorithms are implemented in the LabVIEW program to help the user optimizing the parameters for Z-phase and Z-amplitude, as listed in table 6.1. All algorithms minimize the magnitude R of the digitally computed lock-in signal. It can be chosen whether the first or second harmonic signal is taken into account. The inclination for the slower motion in Y-direction is corrected automatically by the feedback of the commercially variable temperature STM.

Table 6.1.: Optimization algorithms for the amplitude and phase settings in Z-direction.

Name	Description
Z phase rough	Varies Z phase from 0° to 360° with 5° increments in time intervals of 100 ms
Z amplitude rough	Varies Z amplitude to a given maximum in steps of 0.01% to the X amplitude in time intervals of 100 ms
Z phase fine	Varies Z phase in the range of ±2.5° around the current value with 0.1° increments in time intervals of 100 ms
Z amplitude fine	Varies Z amplitude in the range of ±10% around the current value with increments of 0.01% referred to X amplitude in time intervals of 100 ms

After correcting the slope of the sample, the reversal point of the tip between forward and backward motion has to be determined. This information is required, because the tip motion follows the driving voltage with a delay, comparable to a driven damped harmonic oscillator close to resonance. The saved data points are always referenced to the driving voltage in X-direction. The number of pixels, that have to be discarded from the beginning of the experiment, are written in the metadata for the subsequent evaluation. This number is determined by comparing the live preview of the forward and backward images. The raw data is saved in the HDF5 file format, which is optimized for large multidimensional arrays of a homogeneous type and allows the storage of user-defined metadata.

6.4. Data treatment

The FAST raw data is saved in the form of a simple one dimensional array with consecutive intensity values, including metadata about the scan parameters in the header. Data processing, extracting single images and creating videos is performed with a self-written program in python (Version 2.7, Python Software Foundation). The code uses the command line tools of the FFmpeg multimedia framework in the back end with their video codec and container libraries. The program is focused on the compatibility of the three common operating systems: Microsoft Windows, macOS and Linux. Equipped with an optional GUI, see figure 6.4, this program is also executable for a wide range of users.

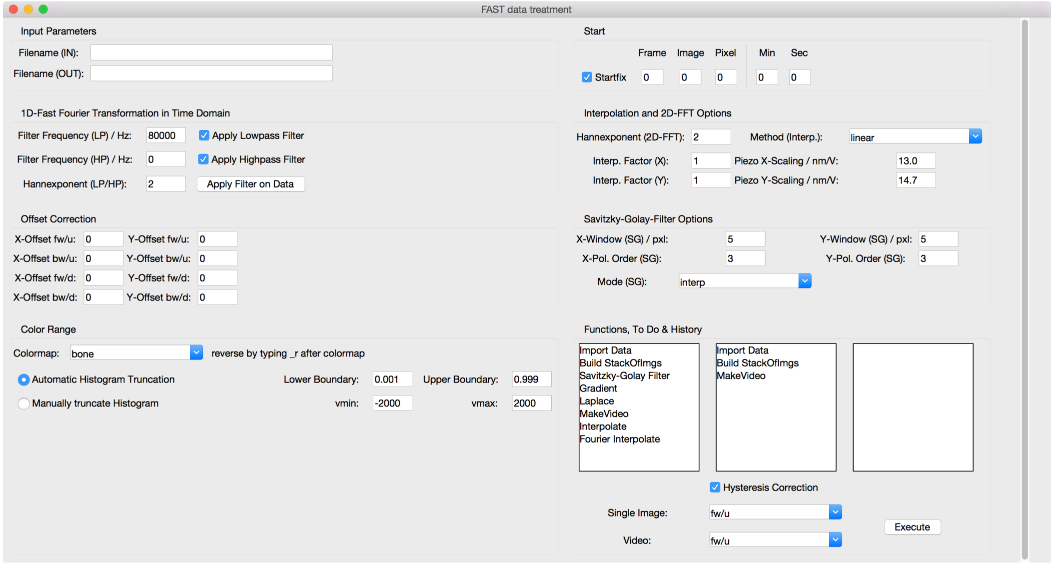

Input Parameters
Filename (IN):
Filename (OUT):

1D-Fast Fourier Transformation in Time Domain
Filter Frequency (LP) / Hz: 80000 ☑ Apply Lowpass Filter
Filter Frequency (HP) / Hz: 0 ☑ Apply Highpass Filter
Hannexponent (LP/HP): 2

Offset Correction
X-Offset fw/u: 0 Y-Offset fw/u: 0
X-Offset bw/u: 0 Y-Offset bw/u: 0
X-Offset fw/d: 0 Y-Offset fw/d: 0
X-Offset bw/d: 0 Y-Offset bw/d: 0

Color Range
Colormap: bone reverse by typing _r after colormap
● Automatic Histogram Truncation Lower Boundary: 0.001 Upper Boundary: 0.999
○ Manually truncate Histogram vmin: -2000 vmax: 2000

Start
Frame Image Pixel Min Sec
☑ Startfix 0 0 0 0 0

Interpolation and 2D-FFT Options
Hannexponent (2D-FFT): 2 Method (Interp.): linear
Interp. Factor (X): 1 Piezo X-Scaling / nm/V: 13.0
Interp. Factor (Y): 1 Piezo Y-Scaling / nm/V: 14.7

Savitzky-Golay-Filter Options
X-Window (SG) / pxl: 5 Y-Window (SG) / pxl: 5
X-Pol. Order (SG): 3 Y-Pol. Order (SG): 3
Mode (SG): interp

Functions, To Do & History

Import Data
Build StackOfImgs
Savitzky-Golay Filter
Gradient
Laplace
MakeVideo
Interpolate
Fourier Interpolate

Import Data
Build StackOfImgs
MakeVideo

☑ Hysteresis Correction
Single Image: fw/u
Video: fw/u

Figure 6.4.: Python GUI for FAST data treatment.

6.4.1. Metadata & frequency analysis

The user can display the meta data of the file, containing the scanning parameters to provide an overview. The meta data contains, inter alia, the AD converter sampling rate, the samples per pixel, the number of frames and images, the beginning of the first frame, the pixel dimensions in X and Y, the respective scanner frequencies and amplitudes, as well as time and date. All operations performed during the data treatment are saved automatically in a log file in the .txt format with the same name chosen for the output of the video .mp4 file. After initialization, the program deletes all data points until the start of the first forward up image. These pixels have to be discarded, because the tip motion is lagging behind the phase of the driving voltage in the fast X-direction, which is the reference for the data saving. The cutting of the data until the first forward up image is performed automatically with the present information in the meta data. Optionally, the user can manually choose the first data point by pixel number or time.

Subsequently, the trimmed one dimensional array of data points can be analysed with the help of discrete Fourier analysis, because all data points are equispaced in time. Thus, internal and external frequencies, disturbing the measurement, become apparent in a spectrum. These frequencies can optionally be filtered out by eliminating contributions in the frequency domain prior to the inverse Fourier transformation back to the original time domain.

6.4.2. Image reconstruction

The one dimensional array of data points has to be rearranged to be depictable and to enable further image processing. The trimmed raw data is still a vector with consecutive upward (u) and downward (d) images, subdivided in alternating rows of forward (fw) and backward (bw) motion. This datavector is now reshaped into a three dimensional array in the form of [Ny, Nx, Nimgs], where Ny and Nx are the number of pixels for each of the Nimgs images, as illustrated in figure 6.5. The images are arranged in the cyclic order fw/u, bw/u, fw/d and bw/d, which is referred to a set of images in the following. The images still differ in the scanning direction in which they were recorded. For that reason all bw images have to be mirrored along the Y-axis and all d images along the X-axis. Finally all images have now the same orientation.

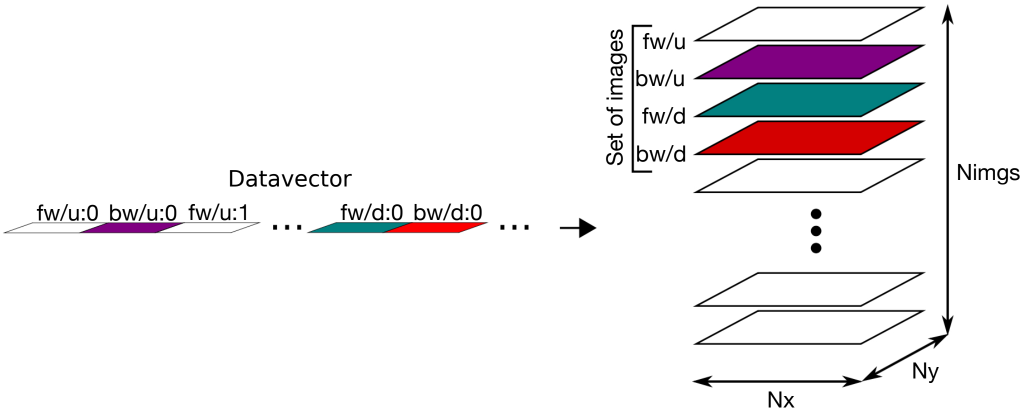

Figure 6.5.: Illustration of the rearrangement of the FAST raw data to a three dimensional array.

6.4.3. Illustration & filter options

Fine adjustments can be performed for each combination of fw/bw and u/d in both X- and Y-direction by cutting data points at the rims of the images. Thus, the smallest common area for the images can be obtained for movies containing images of different scanning directions. In this case the frames are sometimes slightly shifted with respect to each other due to small tip artefacts or inexact phase corrections during the FAST measurement. Nonetheless, these corrections rarely exceed one pixel per image, but have a huge impact on the smooth transition of the moving images.

Various color maps of the matplotlib package can be chosen to present the data in the best way possible, as illustrated in appendix A.1. To exclude outliers that would lead to distorted images, the data points can be truncated either manually by choosing absolute minimum and maximum values or by percentages of the intensity histogram for a lower and an upper boundary to be cut.

Although the images are now oriented in the same way, they are still distorted in the fast scanning X-direction due to the sinusoidal driving voltage applied to the scanner piezo, resulting in a tip motion comparable to a pendulum as depicted in figure 6.6. Hence, the data points are equispaced in time, but not in space.

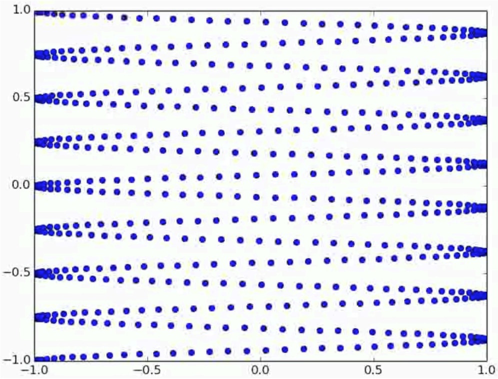

Figure 6.6.: Visualisation of the tip motion during FAST measurements.

For this reason, the sorted data points can be plotted by a meshgrid, which is a two dimensional grid with coordinates that accounts for the sinusoidal tip motion in the fast scanning direction. Even though the visualization via meshgrid is the neatest solution for the untreated data, further processing is rather cumbersome and the advantage of already existing python libraries can not be exploited to a full extent. Therefore the data points can be fitted onto a regular grid in the fast scanning direction, if further data treatment is wanted. The interpolation can be performed with a linear/cubic function or the nearest data point. The default option is the linear interpolation.

Another function implemented in the evaluation program is a filter introduced by Savitzky and Golay [200]. Successive sub-sets of adjacent data points are fitted with a low-degree polynomial. The smoothed signal is then extracted from the central point of each sub-set. In the implemented option the number of pixels per sub-set and the degree of the polynomial can be chosen.

Two dimensional fast Fourier transformation (FFT) leads to the corresponding images in the reciprocal space. Periodic spatial features in the FAST measurements become visible and can be further analysed. In addition, the inverse transformation back in the real space can be exploited for interpolation by zero-filling. Although, the zero-filling does not add any information, the apparent spatial resolution of the images is improved. For edge detection also a gradient and a Laplace filter are implemented by exploiting the inverse FFT.

6.4.4. Image & movie creation

The output of the program can be either .mp4 movie or .png image files. Next to the standard images, options can be chosen that increase the pixel density in the slow scanning direction, as listed in table 6.2.

Table 6.2.: Image output options.

Combined images	Description
fw/u bw/u fw/d bw/d	Single image
fw/u + bw/u fw/d + bw/d	Alternating rows of backward and forward image with the same slow scanning direction
fw/u + fw/d bw/u + bw/d	Alternating rows of up and down image with the same fast scanning direction
fw/u + bw/u + fw/d + bw/d	Alternating rows of a set of images

Multiple options are available for the movie creation. One possibility is to include only images with the same scanning direction. The pixel density in the slow Y-direction can be doubled by combining the fw and bw images of the u or d motion. A combination of a full set of images leads to a quadruplication of this pixel density. All of the options mentioned before have the same frame rate and just increase the pixel density in the slow scanning Y-direction. The frame rate and the pixel density in the slow Y-direction can be doubled by combining images with alternating rows of fw and bw motion with the same slow scanning direction. There is also an option to create a movie containing all 4 images of a stack. This does not make sense in terms of the frame rate, because the fw and bw images are basically measured at the same time, but is a helpful tool to analyze the data. Table 6.3 lists all possible options.

Table 6.3.: Video output options.

Used images	Description	#
fw/u bw/u fw/d bw/d	Only one image per set of images	1
fw/u + bw/u fw/d + bw/d	Alternating rows of backward and forward image with the same slow scanning direction	1
fw/u + bw/u + fw/d + bw/d	Alternating rows of a set of images	1
fw/u + bw/u & fw/d + bw/d	Alternating rows of backward and forward for each slow scanning direction	2
fw/u & bw/u & fw/d & bw/d	Movie including every image	-

6.5. First FAST measurements with static surfaces

The h-BN/Rh(111) superstructure serves as a flat and symmetric surface with a known, long range periodicity for the implementation of the FAST module. The quasi constant height mode in the FAST measurements favours a flat surface. The present symmetry is important to check for resonance frequencies disturbing the tip motion, phase maladjustments and if amplitude corrections are necessary. The large features are easier to detect, which helps during the implementation process. Additionally, the well known long range h-BN superstructure on Rh(111) allows to correlate the FAST settings with the image dimensions. Figure 6.7 illustrates a typical FAST measurement of the beforehand mentioned surface with the scanning parameters listed in table 6.4.

Table 6.4.: Scan parameters on h-BN/Rh(111).

Bias:	-0.6 V	X amplitude:	1.00 V
Current:	1 nA	Y amplitude:	0.75 V
Pixel dimensions:	100×100	X frequency:	800 Hz
Samples per pixel:	625	Y frequency:	4 Hz

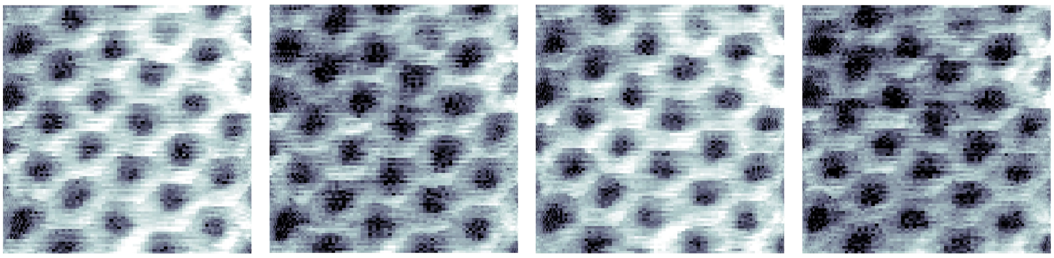

(a) fw/u (b) bw/u (c) fw/d (d) bw/d

Figure 6.7.: Raw data comparison of the 4 scanning directions with the FAST on the h-BN/Rh(111) surface.

The hexagonal moiré superstructure can easily be identified in figure 6.7. The overall image size is determined to be 14×14 nm^2, based on the unit cell of h-BN/Rh(111) with a periodicity of 3.2 nm [61]. The image is not distorted, which can be checked by means of two dimensional FFT, shown in figure 6.8. The six bright blue spots in hexagonal arrangement around the center represent the h-BN lattice, whereas the red spot in the middle of the image can be ascribed to higher frequency noise. The two brighter spots left and right of the center red point are a result of a hysteresis in Z-direction, which is also recognizable in figure 6.7. The fw images appear brighter and therefore the tip is closer to the sample surface than in the bw motion. This can be explained by the evaluation program that takes all data points into account to set the color range, independent of the scanning direction, in order to make all images comparable to each other. In this measurement a small hysteresis in Z-direction is occurring, so that the tip is further away from the sample surface in the bw motion compared to the fw motion. The hysteresis is a result of a maladjustment in the Z-amplitude or an eigenfrequency of the setup. The slow feedback of the conventional STM tries to correct the slope in the fast scanning direction, causing the hysteresis. This shows the effectiveness of the sinusoidal driving voltages for the fast scanning movements, which are only faintly visible in the two dimensional FFT.

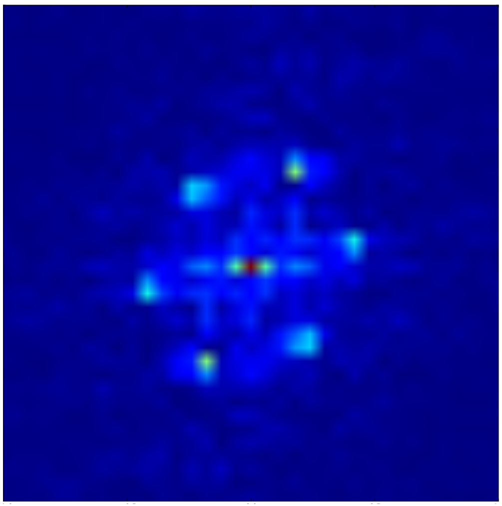

Figure 6.8.: 2D-FFT of the h-BN/Rh(111) surface measured with FAST.

As already described earlier in section 6.4, images of different scanning directions can be combined in order to increase the pixel density in the slow Y-direction. The four possible options are depicted in figure 6.9. The combination of the fw and bw motion in the same slow scanning direction is reasonable, since the lines are measured one after each other. No time resolution in terms of frames per second is lost since for example the fw/u and the bw/u images are recorded basically at the same time. However, the appearance of the images is enhanced by doubling the pixels in Y-direction. Occasionally, the combination of the fw and bw images of the same slow scanning directions is not reasonable with the raw data, because the images are displaced slightly due to tip artefacts or a maladjustment of the X-phase during the measurement. Therefore, the user can cut the images at the rims to compensate for the offset, as already described in section 6.4.

This problem does not occur, when plotting alternating rows of the u and d images of the same fast scanning direction. This option is only reasonable to increase the pixel density of a single image, since the time resolution in terms of frames per second is reduced by a factor of two. The same occurs for the option to combine all 4 different scanning directions. Here, the number of pixels is quadrupled in the slow scanning direction. Figure 6.9 illustrates 4 possible image combinations to increase the pixel density.

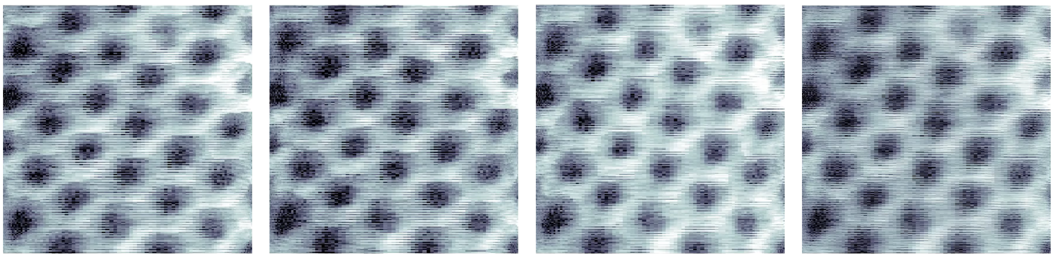

(a) fw/u + bw/u (b) fw/d + bw/d (c) fw/u + fw/d (d) all 4 scan directions

Figure 6.9.: Raw data combination of various scanning directions to increase the pixel density on the h-BN/Rh(111) surface.

Since the FAST measurements are performed in quasi constant height mode and at higher currents in the range of several 100 pA up to nA, in order to be able to measure with the highest possible bandwidth of the standard STM preamplifier, it has to be checked if it is still possible to measure protrusions like step edges or nanoparticles with the add-on instrument. Therefore, a step edge on the h-BN/Rh(111) surface is measured with the same FAST settings as listed in table 6.4 and shown in figure 6.10. The step edge is clearly identifiable and also the troughs of the h-BN/Rh(111) structure can still be seen on both terraces, despite of the use of the logarithmic preamplifier.

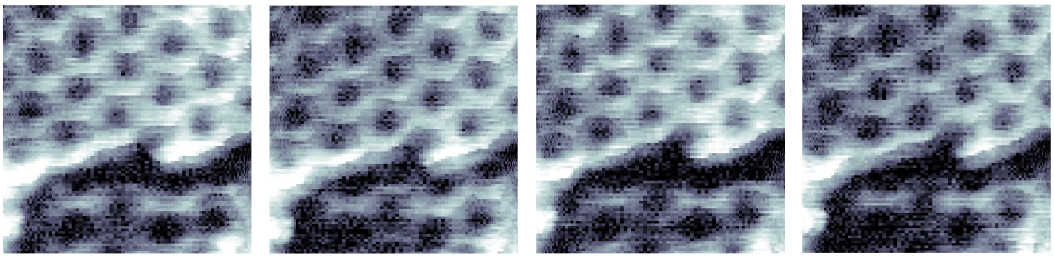

(a) fw/u (b) bw/u (c) fw/d (d) bw/d

Figure 6.10.: Raw data comparison of the 4 scanning directions with the FAST on the h-BN/Rh(111) surface including a step edge.

This finding gives rise to the question, if also small nanoparticles can be measured with the FAST module, without being affected by the tip in close vicinity and at high scan speeds. Therefore, size-selected Pd_{12} clusters are deposited on h-BN/Rh(111) and examined with the add on instrument. Figure 6.11 shows a FAST measurement of two clusters on h-BN/Rh(111) with different apparent heights. The bigger particle is most probably a result of Ostwald ripening processes occurring on the h-BN/Rh(111) surface. Atom detachment is more favourable on the present moiré structure than concerted motion due to the high binding energy of the clusters. The nanoparticles remain stable on the surface and no mobility is induced by the high speed tip motion at close vicinity due to the settings with high currents during the FAST measurements. This proves the possibility to examine size-selected clusters with the FAST module.

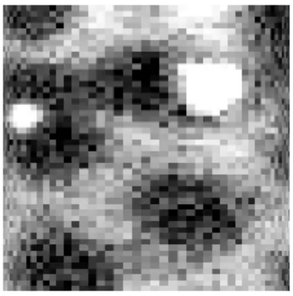

Bias:	-0.6 V
Current:	150 pA
Pixel dimensions:	50×50
Samples per pixel:	1250
X amplitude:	0.42 V
Y amplitude:	0.37 V
X frequency:	800 Hz
Y frequency:	8 Hz

Figure 6.11.: Raw data FAST image of a single and double layer high Pd cluster on h-BN/Rh(111) with corresponding scanning parameters.

Additionally, a conventional STM measurement is performed on the same clusters, which is shown in figure 6.12. The moiré superstructure shows a flat topography with steep holes and a flat bottom. The measured depth depends on the diameter of the troughs and therefore on the film quality. Thus, the cluster height is determined by referencing the maximum of the particle to the rims of the h-BN/Rh(111) surface. An upshift of 1.3 Å in the height values is necessary to correct for the depth of the h-BN holes [45], which is higher than the calculated depth of 0.6 Å using ab initio DFT [59]. The difference might be related to electronic effects. The upshift corrected height of the two clusters is 1.8 Å and 3.3 Å. Even if the correction of the cluster height is debatable, the difference in height of 1.5 Å is reasonable and close to the atomic radius of Pd. Those two clusters are undoubtedly one and two atomic layers high.

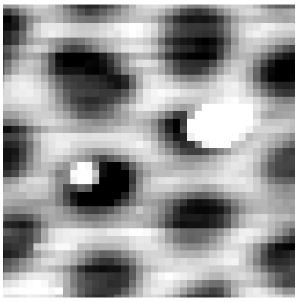

Figure 6.12.: Conventional STM image of a single and double layer high Pd cluster on h-BN/Rh(111) [150 pA, -0.6 V, 10×10 nm^2].

In the following, the maximum achievable resolution with the add-on instrument is examined. Therefore, a clean Rh(111) single crystal surface is investigated with the conventional variable temperature STM and the FAST module. Atomic resolution is achievable in both cases, as shown in figures 6.13 and 6.14, illustrating the measurement results. These high resolution images could only be achieved by a significant noise reduction of the conventional STM. Atomic resolution is now also possible with the preamplifier set to a low amplification factor and a high bandwidth of 80 kHz. The drift in the small STM image in figure 6.13b rules out artefacts caused by external frequencies and is another proof for the validity of the images.

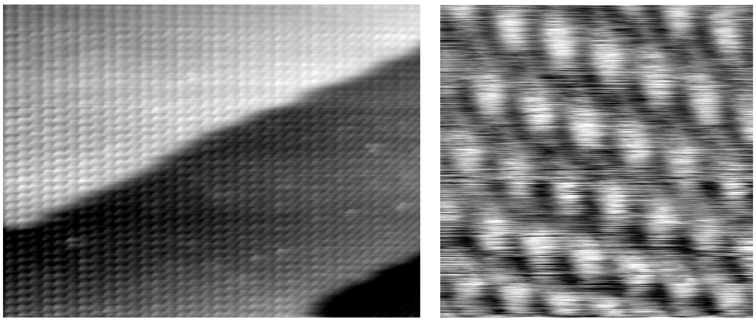

(a) 100×75 nm^2 (b) 2×2 nm^2

Figure 6.13.: Atomic resolution on Rh(111) with the conventional STM [1 nA, 0.3 V].

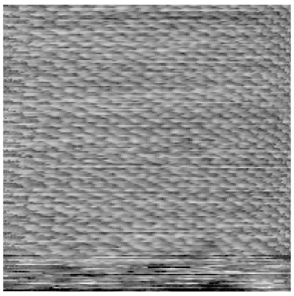

Bias:	0.3 V
Current:	1 nA
Pixel dimensions:	200 × 200
Samples per pixel:	312
X amplitude:	0.50 V
Y amplitude:	0.75 V
X frequency:	801 Hz
Y frequency:	2 Hz

Figure 6.14.: Atomic resolution on Rh(111) with the FAST module with corresponding scanning parameters.

7. Mobility of Pd clusters on h-BN/Rh(111)

The challenge to fully exploit the time resolution of the FAST module for the investigation of surface dynamics lies in the fact that the preparation of the surface to be investigated takes time, as well as setting up the FAST measurement. Typically, one can therefore well investigate reversible processes at thermodynamic equilibrium, such as diffusion events. Ideal systems for this kind of investigations are confined dynamics, such as the atom scale diffusion of small Pd clusters or atoms trapped in the h-BN moiré troughs. However, as soon as irreversible processes come into play, as for example the capture of diffusing species at defects, the surface becomes inactive before the FAST measurements can be started. Irreversible processes can be investigated as well by triggering the events in a controlled way. This can be a change in temperature, but this takes again some time to settle thermal drift, the dosage of reactive gases, as for example the growth of graphene on Rh(111) [46] or Ni(111) [198, 199], or altering electrochemical potentials when working in liquids.

Since FAST measurements are performed at high frequencies, where the preamplifier works with lower amplification in order to increase the bandwidth, the tunneling currents have in general to be set to elevated values. Since this might influence the observed surface processes, systematic experiments on tunneling current and field dependencies have been performed as well.

7.1. Time resolved diffusion of a Pd particle trapped in a h-BN/Rh(111) trough

Initial experiments with the FAST module focus on reversible dynamics. These enable FAST measurements over a longer period of time compared to triggered studies, that would allow only one experiment per cluster deposition.

To begin with, Pd_{12}/h-BN/Rh(111) is chosen as a model system. The moiré superstructure creates rings of in-plane dipoles that can trap molecules and atoms [66, 201]. Thus, ripening processes of the Pd clusters are suppressed to a large extent and size-selectivity is preserved over a longer period of time. The objective is to study the dynamics of nanoparticles, being trapped within the troughs of the h-BN/Rh(111) moiré superstructure, with the enhanced time resolution of the FAST module. Previous studies have shown that Pd_{19} is stable on the before mentioned surface at room temperature [45]. For this reason, the cluster size is further reduced to Pd_{12}, which is known to diffuse on graphene/Rh(111). There are two Pd_{12}

isomers, being one and two atomic layers high with distinct footprints. The most stable isomer is the two layer high structure with a 7-atom hexagonally shaped footprint. In general, the binding of the cluster to the support is dominated by the number of atoms in the footprint [130, 51]. Therefore, the two layer isomer, which should have a higher diffusivity due to a smaller footprint, is investigated in the confined space of a h-BN/Rh(111) trough. Figure 7.1 shows a STM measurement of the two Pd_{12} isomers on the superstructure. The mobility of the clusters are supposed to be controllable via temperature.

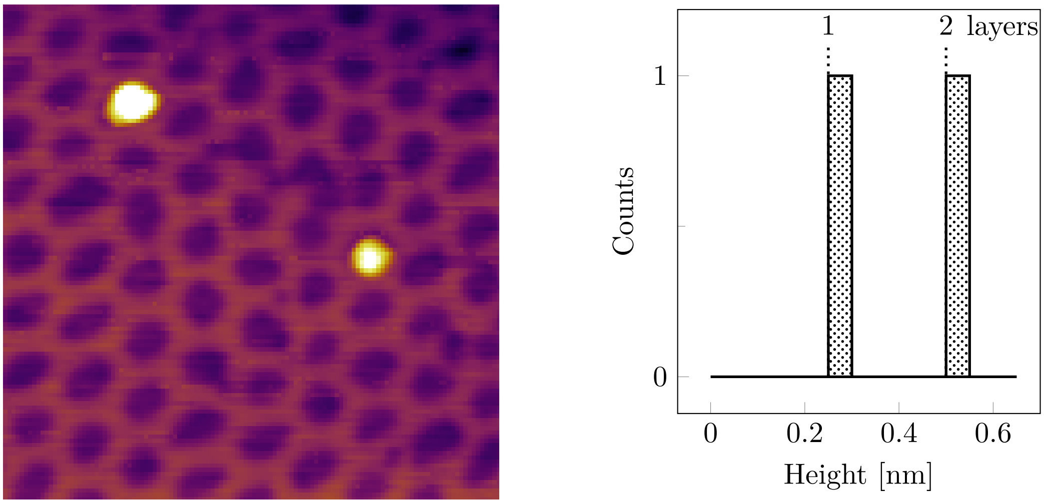

Figure 7.1.: STM measurement depicting the two Pd_{12} isomers on h-BN/Rh(111) [150 pA, -2.0 V, 30 × 30 nm^2].

Experiments with the FAST module show no mobility of Pd_{12} in the troughs of h-BN/Rh(111) at room temperature, as it is also the case for Pd_{19} [45]. Furthermore, dynamics cannot be induced by heating up the sample to 375 K in the variable temperature STM. However, a Pd_{12} cluster disintegrates during a FAST measurement, leaving behind a smaller residue, which diffuses within a h-BN/Rh(111) trough. The FAST sequence of the disintegration process is shown in figure 7.2 with the corresponding scan parameters listed in table 7.1.

Table 7.1.: Scan parameters for time resolved diffusion of a particle formed by decomposition of Pd_{12} trapped in a h-BN/Rh(111) trough.

Bias:	-0.6 V	X amplitude:	0.37 V
Current:	150 pA	Y amplitude:	0.37 V
Pixel dimensions:	50 × 50	X frequency:	800 Hz
Samples per pixel:	1250	Y frequency:	8 Hz

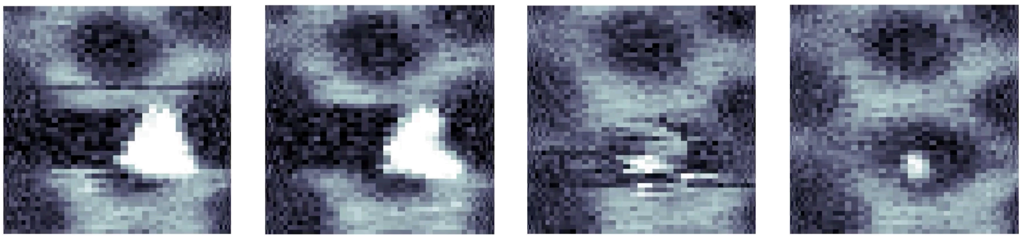
(a) 0 ms (b) 125 ms (c) 250 ms (d) 375 ms

Figure 7.2.: Disintegration sequence of a Pd_{12} cluster during a FAST measurement.

First of all, the scan parameters are optimized. The current setpoint in the FAST measurements should be chosen as low as possible to reduce potential influences on the particles motion, but the images should still have a high S/N. Therefore, the current setpoint is varied in the range from 50 pA to 1 nA and the changes in the S/N are illustrated in figure 7.3. Besides the altered current setpoint, the parameters listed in table 7.1 are applied.

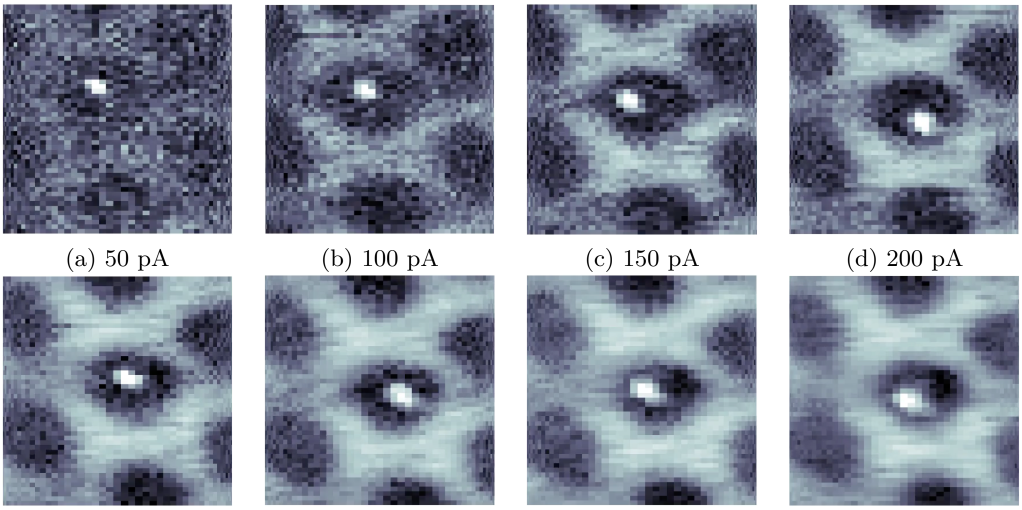
(a) 50 pA (b) 100 pA (c) 150 pA (d) 200 pA

(e) 300 pA (f) 400 pA (g) 500 pA (h) 1 nA

Figure 7.3.: Comparison of FAST raw data images measured at varying current setpoints of the particle formed by decomposition of Pd_{12} on h-BN/Rh(111).

The noise level increases by lowering the current setpoint, in particular for the contrast of the h-BN/Rh(111) moiré superstructure. This can be explained by the operation of the FAST module in the quasi constant height mode. Apart from the sinusoidal driving voltage in Z-direction, correcting the overall tilt of the surface in X-direction, the Z-regulation is still controlled by the slow conventional STM. Thus, the height adjustment is only performed several times per frame with the FAST module, instead of every data point with a conventional STM electronics.

As a consequence, the highest LDOS of the scan area defines the distance between tip and surface. Therefore, the signal contribution of the support decreases at lower current setpoints, because the tip is scanning at greater distances to the surface in the quasi constant height mode. A reasonable S/N can be obtained for current setpoints above 150 pA. The vast majority of the FAST data is measured with current setpoints of 150 pA and 300 pA to reduce the risk of potential influences of the fast scanning tip on the diffusion behaviour of the particle.

The next step is to find an optimum ratio of pixel density and frame rate, limited by the 80 kHz bandwidth of the preamplifier. Two raw data images with 50×50 and 100×100 pixels and corresponding scan parameters are shown for comparison in figure 7.4. It is obvious that there is no gain in information by the higher pixel density in the raw data, instead the time resolution is reduced by a factor of two. For this reason, a FAST setting with a rather low but sufficient pixel density for the localization of the diffusing residue is chosen to enable a high frame rate.

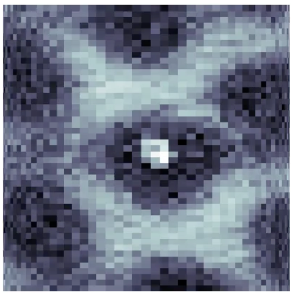

Bias:	-0.6 V
Current:	150 pA
Pixel dimensions:	50×50
Samples per pixel:	1250
X amplitude:	0.42 V
Y amplitude:	0.37 V
X frequency:	800 Hz
Y frequency:	8 Hz

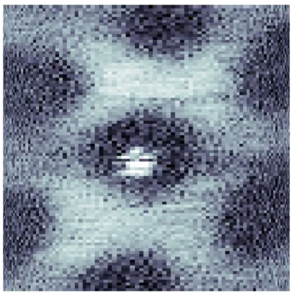

Bias:	-0.6 V
Current:	150 pA
Pixel dimensions:	100×100
Samples per pixel:	625
X amplitude:	0.42 V
Y amplitude:	0.37 V
X frequency:	800 Hz
Y frequency:	4 Hz

Figure 7.4.: Comparison of FAST raw data images with varying pixel densities of the particle formed by decomposition of Pd_{12} on h-BN/Rh(111).

The particles motion could be monitored over a time span of 3 hours and is apparently trapped effectively within the trough of the h-BN/Rh(111) moiré superstructure. This is an unique example for systematic studies on fast cluster dynamics under an STM tip. An exemplary time series of 2.5 s in total with increments of 125 ms is illustrated in figure 7.5. The respective measurement parameters are listed in table 7.1. The images in figure 7.5 are smoothed with a Savitzky-Golay filter using a third order polynomial over 5 adjacent data points and subsequently interpolated by a factor of two to increase the pixel density. Apparently, no specific sites are discernible for the particles motion.

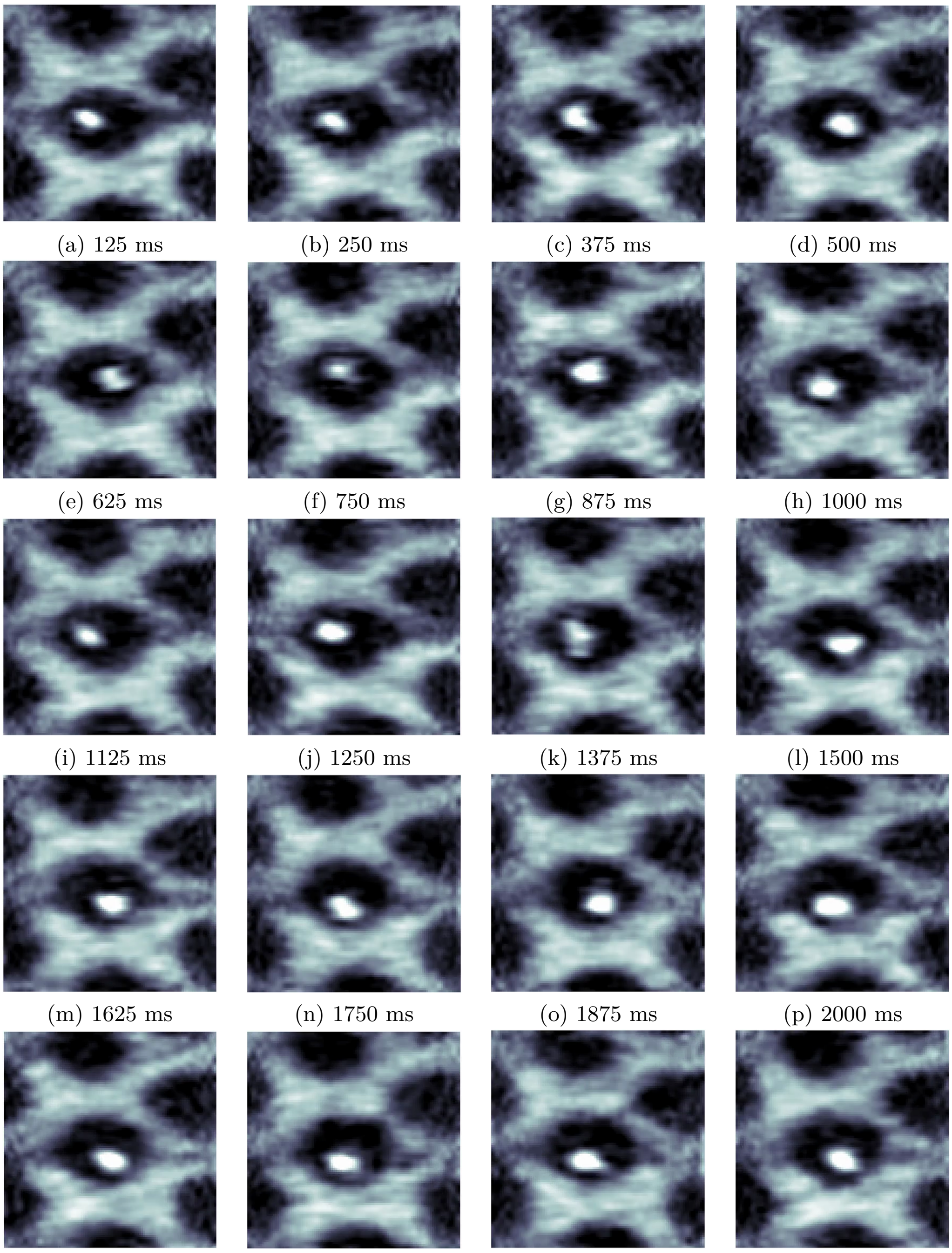

(a) 125 ms (b) 250 ms (c) 375 ms (d) 500 ms

(e) 625 ms (f) 750 ms (g) 875 ms (h) 1000 ms

(i) 1125 ms (j) 1250 ms (k) 1375 ms (l) 1500 ms

(m) 1625 ms (n) 1750 ms (o) 1875 ms (p) 2000 ms

(q) 2125 ms (r) 2250 ms (s) 2375 ms (t) 2500 ms

Figure 7.5.: Video footage of the intracellular motion of a particle formed by decomposition of Pd_{12} on the h-BN/Rh(111) surface.

In the following, the spatial distribution of the diffusing nanoparticle is analysed thoroughly. The residue is never observed in close proximity to the rim of the trough. This finding can be explained by the repelling character of the rims in the h-BN/Rh(111) moiré superstructure, which is also preventing the residue from diffusing outside of the trough [66]. Moreover, the particle is rarely located in the center of the moiré cell. This is in agreement with combined STM and molecular dynamics (MD) studies on the Xe adsorption on h-BN/Rh(111), stating a pronounced adsorption energy maximum close to the rim of the nanomesh pore [68]. The preference for this off-center position is also found for the phthalocyanine molecules H_2Pc and CuPc on h-BN/Rh(111) by means of STM and DFT calculations [202]. Furthermore, Mn atoms deposited on the moiré superstructure are as well located in close proximity to the rims of the pores as shown in STM studies [69].

An in-depth analysis of the particles geometric center per frame reveals a hexagonal pattern with lateral distances of ~2.5 Å, as illustrated in figure 7.7a. The measured distance between the sites is comparable to the lattice constant of Pd(111) with 2.75 Å and the h-BN film with 2.50 Å [57, 61, 59]. At first glance, the sixfold symmetry can be explained by the hexagonal shape of the moiré trough, leading to six preferential sites [202]. However, the orientation of the particles hexagonal pattern is rotated by 30° with respect to the hexagonal moiré pattern and the boron nitride lattice. A ball and stick model of the h-BN/Rh(111) nanomesh unit cell is illustrated in figure 7.6b. Here, the centers of the h-BN/Rh(111) troughs are located in the four corners of the unit cell. The rotation of the hexagonal pattern by 30° in combination with the lateral distances of ~2.5 Å lead to the assumption that the geometric center of the particle is located on top of the six nitrogen atoms surrounding the center of the h-BN/Rh(111) trough, as depicted in figure 7.6c. However, DFT calculations state that Au atoms and clusters adsorb strongly on top of the B atoms [201, 203]. Assuming a triangular shaped Pd_3 cluster (roughly in line with the apparent size of the investigated cluster in the STM), a flat arrangement with all three Pd atoms stabilized on top of B atoms leads exactly to a configuration that is centered around N atom positions.

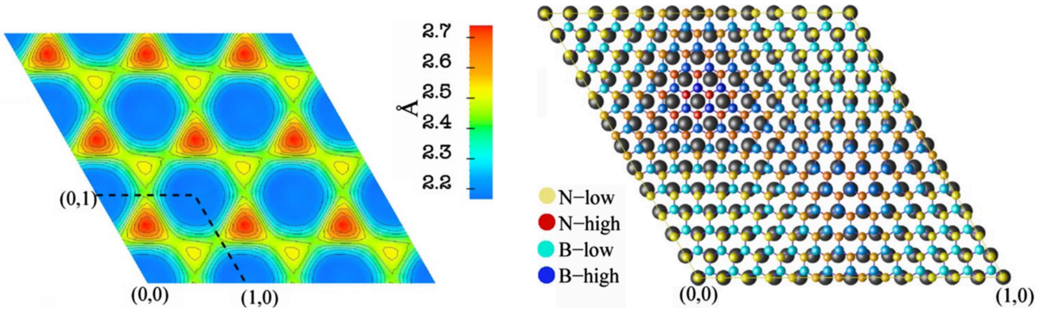

(a) Contour map of the N atoms in the 3 × 3 nanomesh unit cell.

(b) Ball and stick model of the h-BN/Rh(111) unit cell with one metal layer. The colors indicate the height of the B and N atoms.

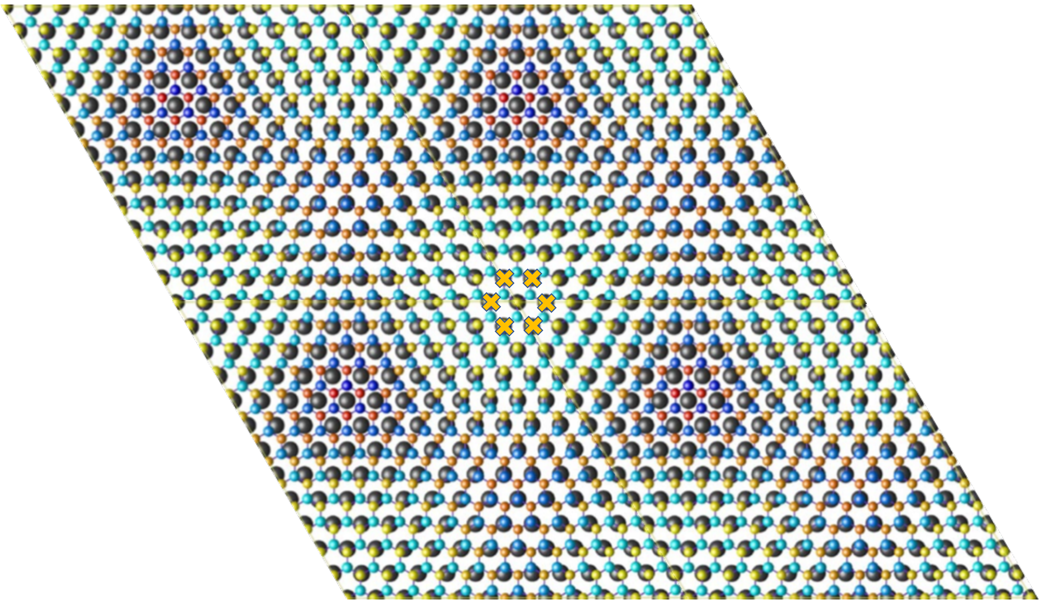

(c) Ball and stick model of a h-BN/Rh(111) trough with one metal layer and the locations of the particles geometric center (orange crosses).

Figure 7.6.: Simulations of h-BN/Rh(111) indicating the relative orientation of the atomic BN lattice with respect to the observed wire structure [59].

The uniform population in figure 7.7a leads to the assumption that all sites are thermodynamically equivalent. For further data processing, the h-BN/Rh(111) trough is partitioned into six compartments, facilitating an automated assignment of the particle to the six hexagonally arranged preferential locations. Figure 7.7b shows the temporal evolution of the nanoparticles position trapped in the moiré superstructure.

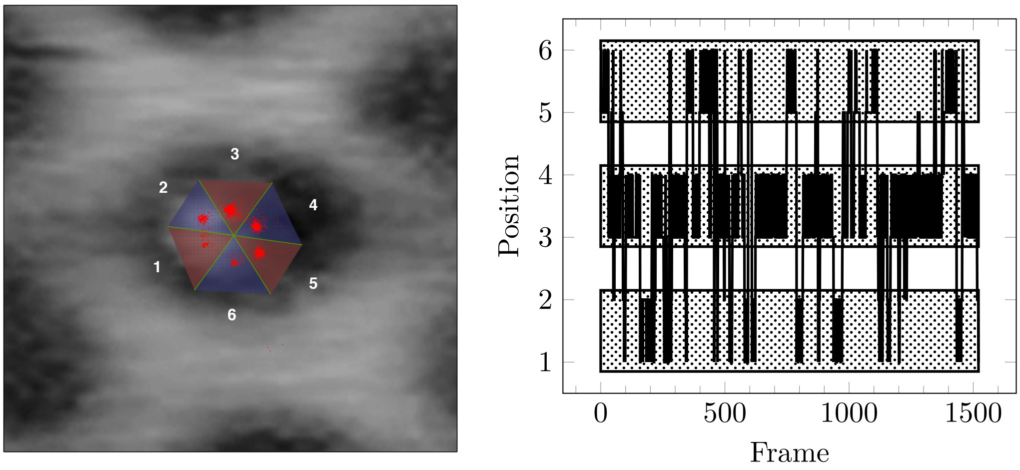

(a) Preferential sites

(b) Temporal progression

Figure 7.7.: Spatial and temporal analysis of the residues geometric center formed by decomposition of Pd_{12} on h-BN/Rh(111) [300 pA, -0.6 V].

The apparent residence time of the particle is in the order of the frame rate. Interestingly, a movement of the residue is only observed to adjacent sites. A closer inspection of the diffusion behaviour in figure 7.7b reveals a hierarchical movement. The particles motion can be divided into two different time scales: the diffusion within site pairs in the order of the frame rate and between site pairs, which is occuring less frequently. An investigation of the latter is realized by combining the three distinct site pairs in figure 7.8a. The analysis of the particles motion between the site pairs reveals a residence time of 14.63 ± 1.85 frames.

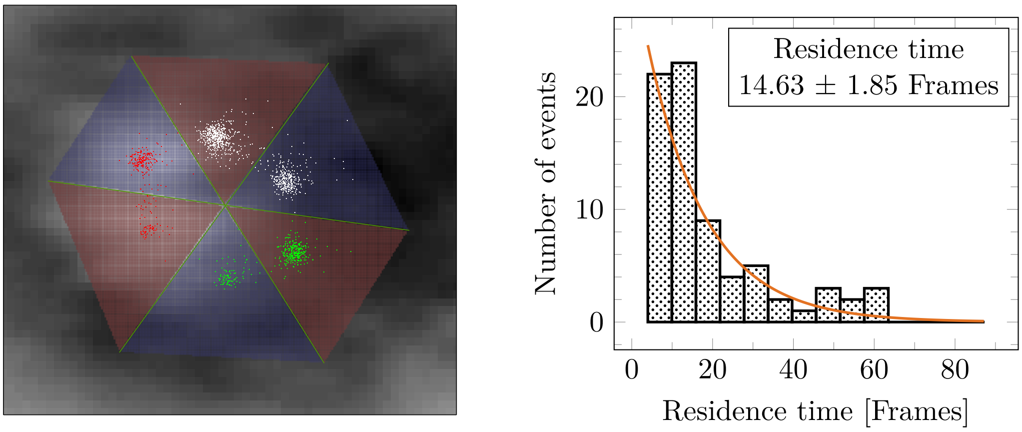

(a) Assignment of the site pairs

(b) Temporal analysis

Figure 7.8.: Spatial and temporal analysis of the residues geometric center formed by decomposition of Pd_{12} on h-BN/Rh(111) [300 pA, -0.6 V].

In general, the Pd nanoparticles diffusion on the moiré superstructure can be described as follows. The h-BN/Rh(111) trough possesses six thermodynamically equivalent sites. The nanoparticles diffusion kinetics is explainable by two distinct activation barriers between these six locations. This may be induced by the threefold symmetry of the BN-lattice. The sites of a pair are separated by a low activation barrier, resulting in a residence time of the residue in the order of the frame rate. However, the activation barrier for the nanoparticle to move between the three site pairs is higher with a residence time of 14.63 ± 1.85 frames. Thus, the diffusion of the residue occurs on two different time scales.

The FAST measurements are performed at elevated current setpoints, which allow for a high bandwidth preamplifier setting. As a consequence, the tip is operating in close proximity to the surface and could have an impact on the particles motion. Potential disruptive influences of external factors are discussed in the following. Besides varying the bias and current setpoint, the parameters listed in table 7.1 are applied. Changes would be hard to distinguish by considering all diffusion events, as these are in the order of the frame rate. Therefore, a potential change in the particles residence time between the three site pairs is investigated. Figure 7.9 shows consecutive FAST measurements at the same current setpoint of 300 pA with varying bias settings of +0.5 V, -0.6 V and ±1.0 V. No significant influence on the particles diffusion behaviour is discernible. However, FAST measurements at higher positive and negative bias voltages lead to increasingly fuzzy images, making an automated assignment of the residues position unfeasible. Here, an influence of the tip is observable similar for both signs. This finding at elevated bias voltages leads to the assumption that the effect is most probably field-induced.

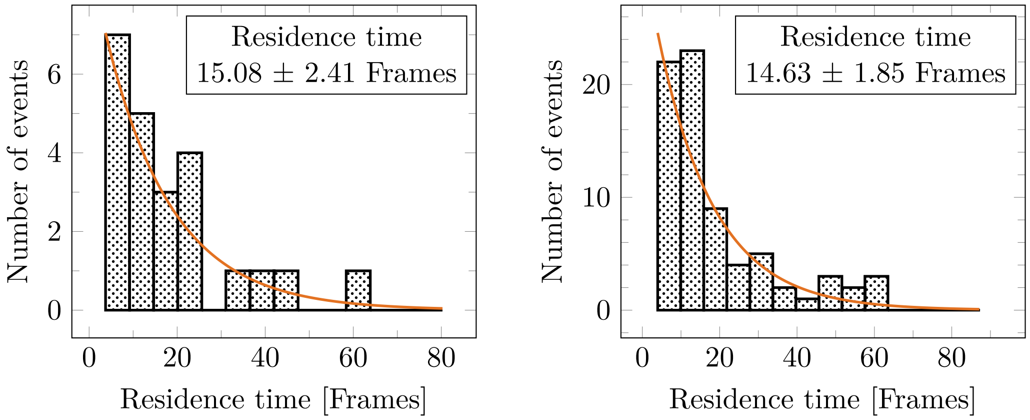

(a) [300 pA, +0.5 V]

(b) [300 pA, -0.6 V]

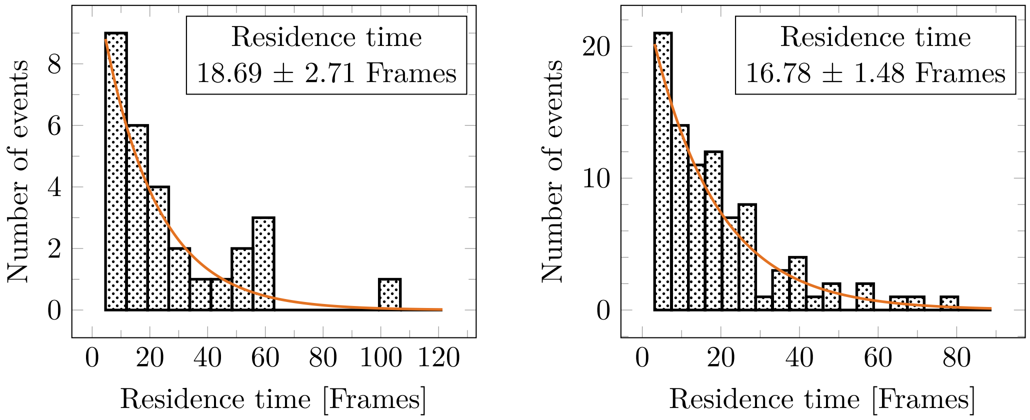

(c) [300 pA, +1.0 V]

(d) [300 pA, -1.0 V]

Figure 7.9.: Residence times on the site pairs of the residues geometric center formed by decomposition of Pd_{12} on h-BN/Rh(111) at various bias settings.

Moreover, the current setpoint is varied during the FAST measurements, altering the tip sample distance. Figure 7.10 illustrates the ascertained residence times. All data show the same diffusion behaviour for the nanoparticle, except figure 7.10a. It is worth noting, however, that the video at a current setpoint of 200 pA is shorter than the others and is therefore more prone to errors because of a limited dataset. For this reason, it is assumed that the tip-cluster distance is not an issue. In literature, tip enhanced diffusion is observed for tunnelling currents above 10 nA [179].

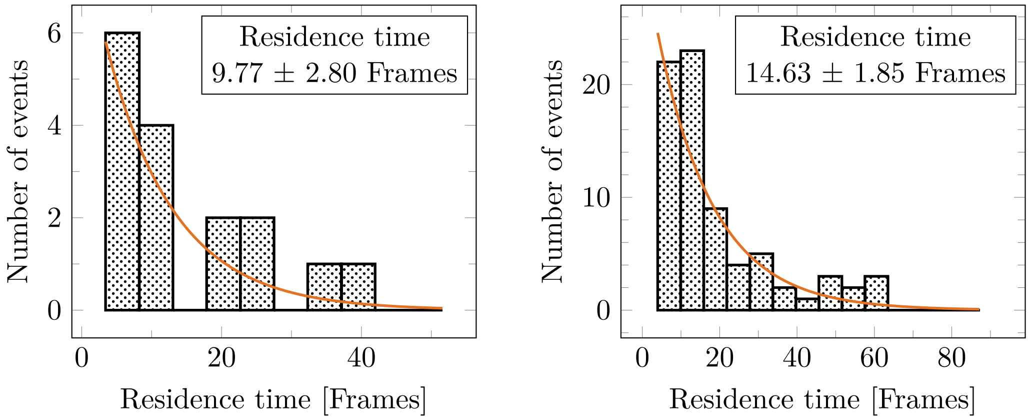

(a) [200 pA, -0.6 V]

(b) [300 pA, -0.6 V]

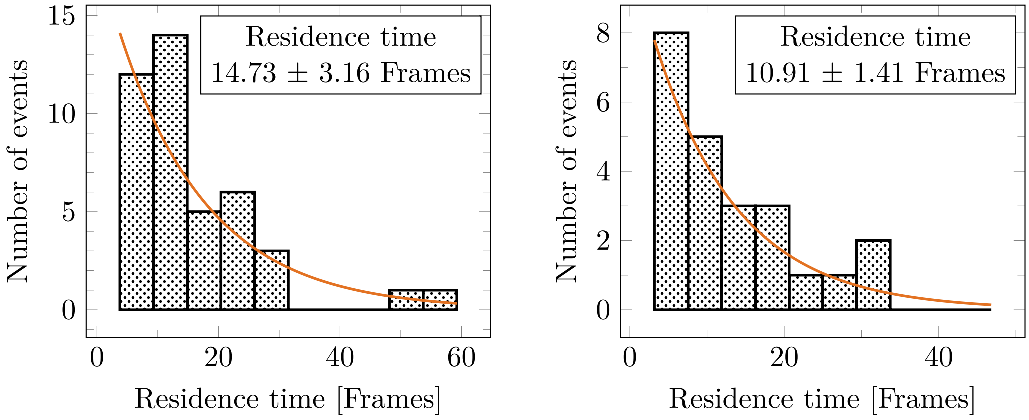

(c) [500 pA, -0.6 V]

(d) [1000 pA, -0.6 V]

Figure 7.10.: Residence times on the site pairs of the residues geometric center formed by decomposition of Pd_{12} at various current setpoints.

Furthermore, it is investigated if a preferred motion of the particle is induced in the slow scanning direction of the FAST module. Therefore, the vertical displacement of the residue is analysed between the up and down images and vice versa. No preferred motion of the residue can be observed in the first two hours of the FAST measurements, but interestingly a shift of ~1.5 pixels, corresponding to ~0.15 Å, becomes apparent after 2.5 hours. This effect is still remaining after going back to the initial FAST settings, which leads to the assumption that the tip state can have an influence in the particles motion. Figure 7.11 shows two exemplary datasets before and after the appearance of the vertical displacement. Therefore, it should be noted that a slight influence of the particles motion can be observed depending on the tip state and FAST data should always be checked for tip interactions. The previously shown studies on the particles diffusion behaviour do not contain data, which show a vertical displacement depending on the slow scanning direction.

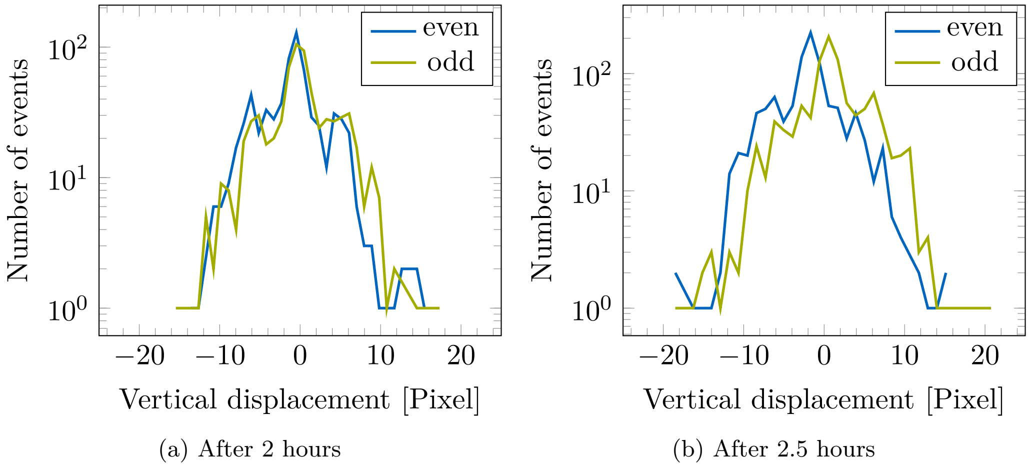

(a) After 2 hours

(b) After 2.5 hours

Figure 7.11.: Investigation of the vertical displacement in the slow scan direction.

Finally, it can be concluded that the diffusion behaviour of the particle is not altered at bias voltages in the range of ±1.0 V. FAST measurements at higher positive and negative voltages lead to an increasingly fuzzy image appearance, which is most probably field-induced. Furthermore, current setpoints up to 1 nA do not have an influence on the motion of the particle. Thus, tip-sample distance is not an issue. Nevertheless, the tip state can have a slight influence on the particle motion, depending on the tip state.

7.2. Visualized circular motion of Pd atoms within h-BN/Rh(111)

Encouraged by the diffusing decomposition product discussed in section 7.1, further experiments focus on smaller nanoparticles than Pd_{12}, which turned out to be stable on h-BN/Rh(111) up to 375 K. For this purpose, the cluster source is optimized for smaller Pd cluster sizes down to single atoms. Therefore, the ion optics, the bender and quadrupole mass filter settings are adjusted accordingly. A mass scan with the new cluster source settings is shown in figure 7.12. Each intensity maximum belongs to one specific cluster size, in this case Pd atoms to Pd_6. The distinct cluster sizes are baseline separated by the quadrupole mass filter settings, ensuring the deposition of the nanoparticles in a size-selected manner. The laser evaporation source intrinsically produces a huge number of Pd atoms, because the clusters are formed by coalescence of atoms from a plasma. The other particle sizes are produced in comparable yields. Soft-landing requires a control of the particles kinetic energy, especially for small cluster sizes or atoms due to energy and momentum conservation requirements [204, 205, 46]. The predicted displacement energy for B or N atoms of the support is about 20 eV with electrons [76, 77] and 50 eV with Rb atoms [78].

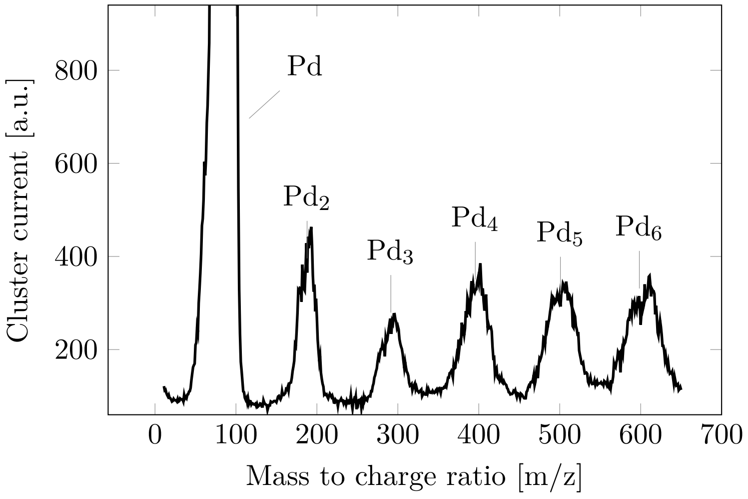

Figure 7.12.: Mass scan of cluster source optimized for small Pd clusters.

Pd atoms deposited on h-BN/Rh(111) at room temperature show a distribution of cluster sizes in STM images, as shown in figure 7.13. Thus, ripening must have occurred during the preparation period. The diffusion processes can be suppressed by cooling the sample to liquid nitrogen temperatures during cluster deposition and STM measurements, as illustrated in figure 7.14. These findings prove that soft-landing down to Pd atoms is feasible, because their mobility is temperature dependent. Therefore, one can conclude that the particles are not pinned to the sample surface. Furthermore, knock-on damage of the h-BN film is unlikely, because of the rather long diffusion pathways of the particles during ripening at room temperature.

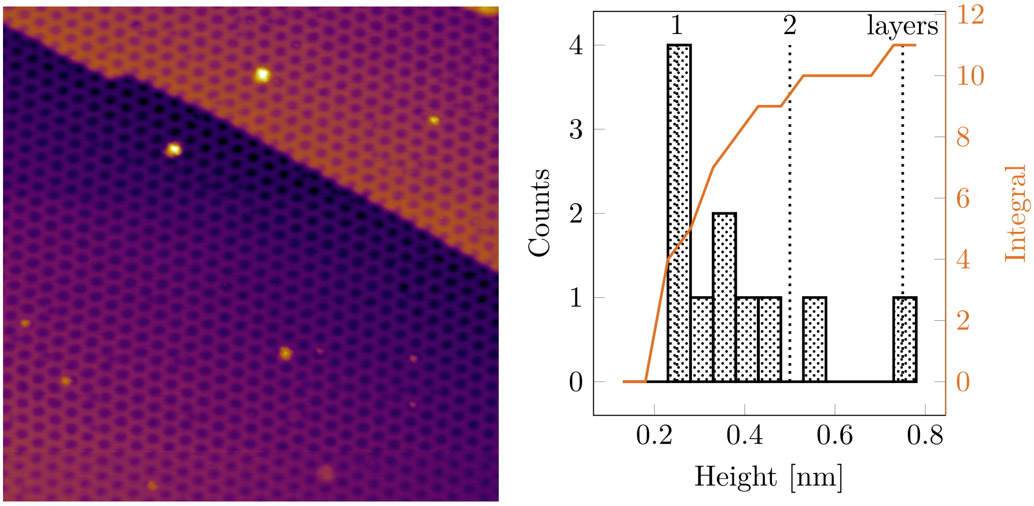

Figure 7.13.: STM measurement at 295 K with corresponding height histogram of Pd atoms deposited on h-BN/Rh(111) [1 pA, -0.6 V, 100 × 100 nm^2].

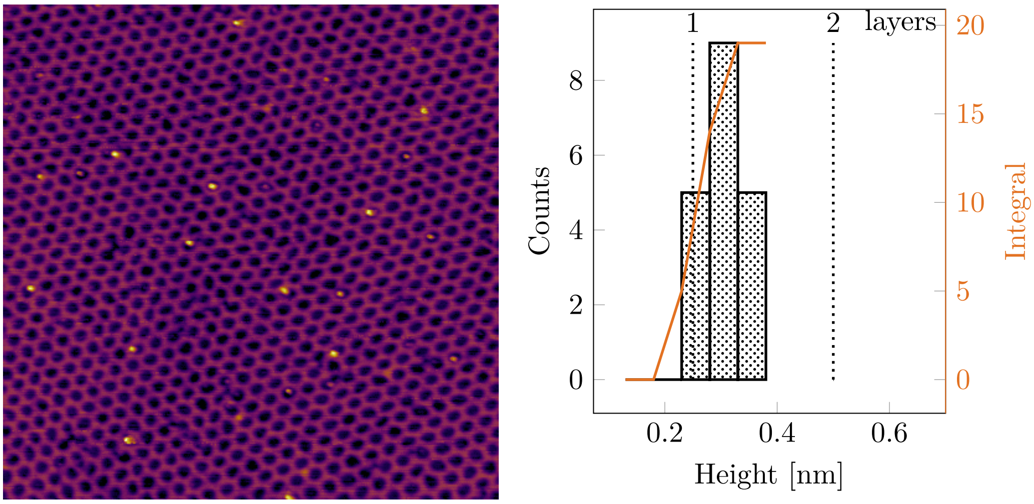

Figure 7.14.: STM measurement at 118 K with corresponding height histogram of Pd atoms deposited on h-BN/Rh(111) [1 pA, -0.6 V, 100 × 100 nm^2]

Pd_4 and Pd_3 clusters can be deposited in a size-selected manner on h-BN/Rh(111) at room temperature and show no ripening behaviour in the height distributions. FAST measurements show that the clusters are also immobile in the troughs of the moiré superstructure at room temperature and after heating up to 380 K.

On the contrary, single Pd atoms show a pronounced ripening in STM measurements at room temperature. Thus, diffusion processes must have already occurred during the preparation period, which can be suppressed by cooling the sample down to 118 K. The deposited cluster charges match the particle density at low temperature, which leads to the assumption that the observed particles are indeed Pd atoms. Furthermore, the cool-down of a room temperature sample to liquid nitrogen temperatures proves that the small species visible in the STM measurements are in fact Pd atoms and not adsorbates resulting from the UHV background. Here, the cluster distribution resembles the room temperature measurement. A mobility of the deposited Pd atoms cannot be induced by dosage of D_2 or CO during STM measurements. Furthermore, the cluster height distribution remains unchanged when dosing the gases in the preparation chamber during the cluster deposition. Thus, the particles are either already saturated with adsorbates from the cluster source background before entering the preparation chamber or unaffected by the two gases.

However, the mobility of the Pd atoms, deposited at cool conditions, can be controlled by the temperature in the STM. In a certain temperature regime, the motion should take place inside of the repelling rims of the h-BN/Rh(111) moiré superstructure, until the thermal energy is high enough and the Pd atoms can overcome the potential barrier of the troughs. Figure 7.15 shows a STM measurement at 168 K. Ring-like structures appear in the troughs of the h-BN/Rh(111) surface, which in some cases also contain brighter spots.

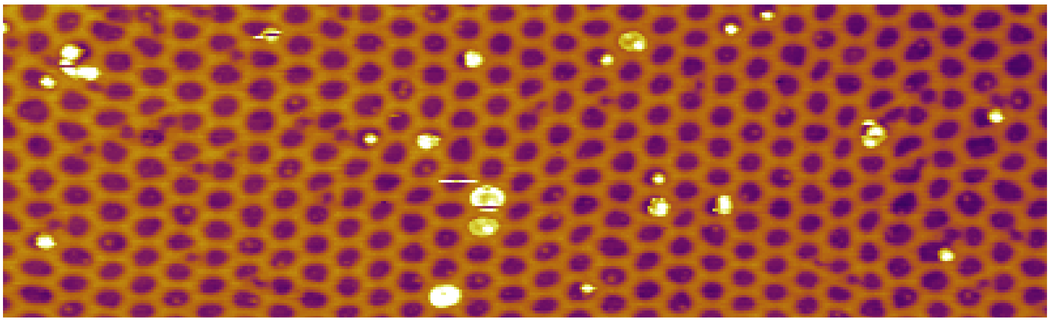

Figure 7.15.: Pd_1/h-BN/Rh(111) [50 pA, -0.6 V, 29×100 nm^2, 168 K].

One explanation for this finding could be a bistable adsorption complex as found for Mn, Co and Fe atoms on the moiré superstructure, which weakens the interaction of the h-BN layer with the underlying metal substrate. A reversible switching between the before mentioned ring state and the appearance of a conventional adatom should be possible [69]. However, STM images show that the circular structure remains within tip induced diffusion events in various moiré troughs at low currents, as illustrated in figure 7.16. The observed mobility makes the before mentioned ring state rather unlikely. Furthermore, the ring-like structure cannot be a defect artefact, which would be immobile.

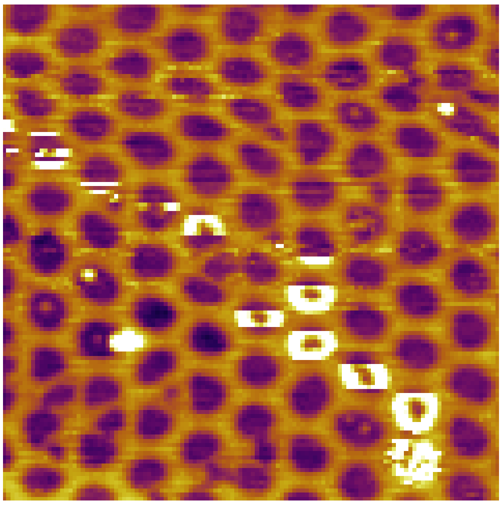

Figure 7.16.: Tip-induced diffusion of the Pd atom ring structures on h-BN/Rh(111) in conventional STM measurements [1 pA, -0.6 V, 30 × 30 nm^2, 168 K].

Moreover, the present ring-like structure resembles combined STM and MD studies of Xe adsorbed on h-BN/Rh(111). Dependent on the substrate temperature, the Xe atoms can be either mobile in the troughs leading to apparent ring-like structures in the comparatively slow STM measurements or static at 5 K forming rings out of 12 Xe atoms [68]. This leads to the assumption that the motion of the Pd atoms is too fast for the temporal resolution of the conventional STM, whereas some Pd atoms remain immobile on the image, which are most probably trapped in defects of the moiré superstructure.

FAST measurements are performed to overcome the limitations in time resolution of the conventional variable temperature STM and to get a further insight on the motion of the particle. Figure 7.17 shows a series of consecutive images recorded with the FAST module. The measurement parameters are listed in table 7.2. The assumed circular motion of the particles trapped in the troughs of the h-BN/Rh(111) moiré superstructure can be confirmed due to the increased temporal resolution of 125 ms with the add-on instrument.

Table 7.2.: Scan parameters for Pd atoms on h-BN/Rh(111).

Bias:	-0.6 V	X amplitude:	0.42 V
Current:	200 pA	Y amplitude:	0.37 V
Pixel dimensions:	50 × 50	X frequency:	800 Hz
Samples per pixel:	1250	Y frequency:	8 Hz

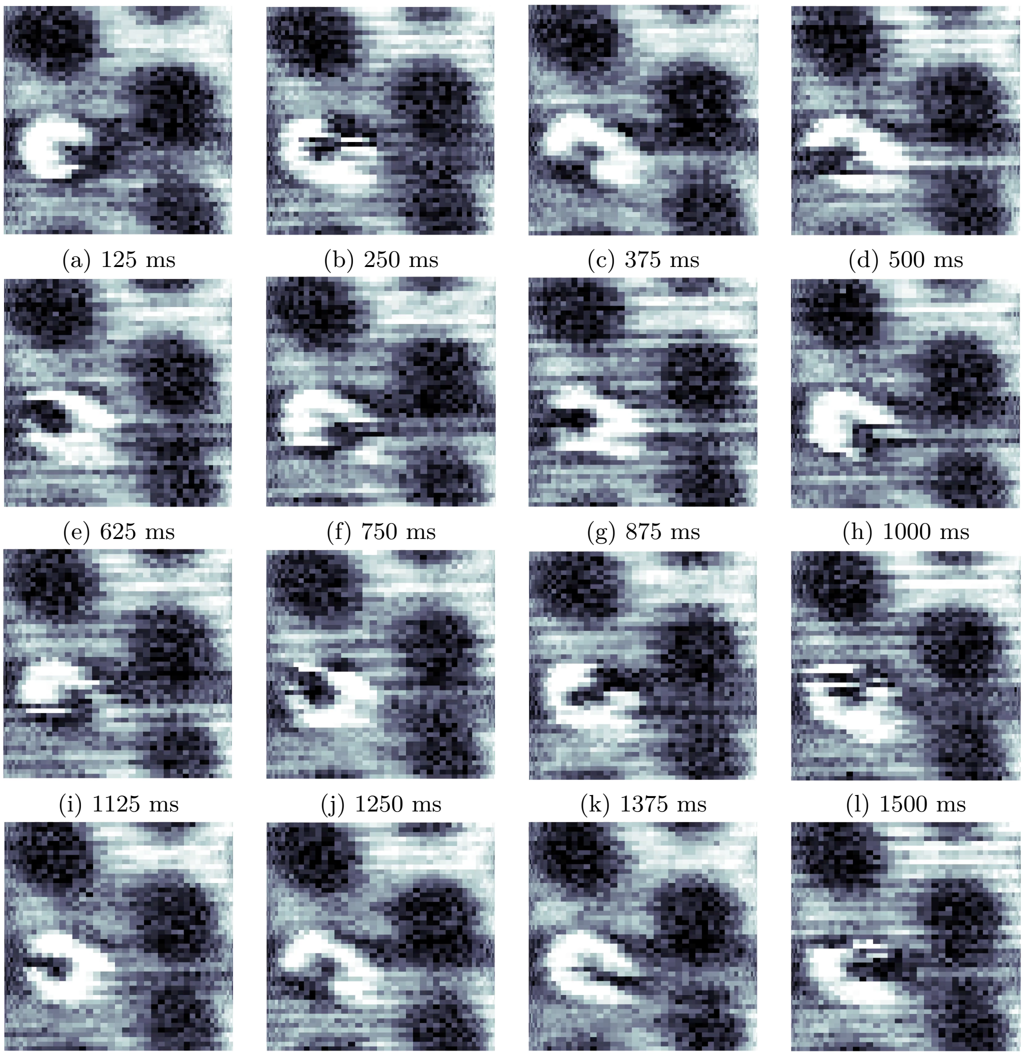

(a) 125 ms (b) 250 ms (c) 375 ms (d) 500 ms

(e) 625 ms (f) 750 ms (g) 875 ms (h) 1000 ms

(i) 1125 ms (j) 1250 ms (k) 1375 ms (l) 1500 ms

(m) 1625 ms (n) 1750 ms (o) 1875 ms (p) 2000 ms

Figure 7.17.: Time resolved diffusion of a Pd atom in a h-BN/Rh(111) trough at 167 K [6×6 nm^2].

The FAST measurements can provide the evidence that the apparent rings in the conventional STM image are caused by a circular motion of the Pd atoms in the troughs of the h-BN/Rh(111) moiré superstructure. However, the particle is still observed in a C-shape. The fact that a full circle is never observed in single frame of the FAST measurement, shows that the residence time of the particle is shorter than frame rate with 125 ms. On the other hand, the residence time of the Pd atom is at least one cycle in the slow scanning direction being 1.2 ms. The motion of the Pd atom is anti-clockwise with an estimated angular frequency of 2 Hz, assuming the particle is moving with a constant velocity. Though these numbers should be treated with caution, as the apparent angular frequency of the particle could also be the beat frequency, if the temporal resolution of the FAST module is not sufficient. Nevertheless, this observation is an excellent example of a possible application of the FAST module.

8. Summary & conclusion

This study links structural dynamics of nanoparticles with their catalytic reactivity. Therefore, a model system with supported size-selected clusters is chosen to enable the combination of local and integral measurement techniques. This system consists of truly monodisperse Pd nanoparticles that are soft-landed on h-BN/Rh(111). The moiré superstructure guarantees that every cluster is confined by the same chemical environment. Part of this dissertation is the implementation and characterization of two measurement techniques in an existing UHV setup that allow studies on the correlation of catalytic activity and dynamics on size-selected clusters.

The catalytic reactivity of the nanoparticles is investigated on the integral scale via highly sensitive thermal desorption studies. For this purpose, the STM sample holder with integrated heater is investigated in front of a modified Feulner cone setup [41]. This particular design reduces background contributions and increases the sensitivity of the device by guiding the desorbing molecules to the ionization part of the mass spectrometer. The high sensitivity is indispensable for reactivity studies with low atom coverages down to single-digit percentages of a monolayer of truly monodisperse clusters on the small and highly complex STM sample holder. Furthermore, an evaluation routine is established in chapter 4, which enables the quantification of TPD spectra by calibration with the ion currents of the well-known Rh(111) - (1×1) - D and Rh(111) - (2×2) - C_2H_3 overlayers. Measurements on the catalytic activity of Pd nanoparticles are described in chapter 5. Initially, the CO oxidation is investigated with unselected $Pd_{\approx 19}$ clusters on h-BN/Rh(111). The sensitivity of the modified Feulner cone setup is sufficient to detect the desorption peak of $C^{18}O_2$ at 380 K. The observed desorption behaviour is comparable to that observed for CO oxidation experiments on Pd(111) [42]. Subsequent desorption cycles lead to a gradual shift of the peak position to lower temperatures which is in line with experiments on evaporated 2.5 nm Pd particles supported on alumina [101]. Possible explanations for this behaviour are oxygen accumulation or the formation of carbonaceous deposits from the background. The cluster ripening has been investigated before and after the TPD measurements by STM. Indeed, the clusters ripen upon heating to 600 K, but this ripening cannot be discriminated from the one obtained in absence of the reactants. Moreover, co-adsorption experiments with D_2 and C_2H_4 on the size-selected Pd_{19}/h-BN/Rh(111) system are performed. Less than 0.15% clusters with respect to the Rh surface atoms are present which ultimately prove the sensitivity of the modified TPD setup. The hydrogenation reaction, occuring at 180 K, and the H-D exchange, occuring at 300 K, could be discriminated by monitoring the desorbing hydrocarbons. The results are in accordance to literature on Pd nanoparticles evaporated on Al_2O_3/

NiAl(110) [43, 44]. During consecutive TPD measurements the peaks evolve: The signal intensity for the hydrogenation reaction decreases, whereas the desorption yield of the H-D exchange increases. The ratio remains constant after several TPD measurements. This can be explained by the lower number of highly coordinated sites available for hydrogen ad-atoms due to the formation of carbonaceous deposits [112]. Complementary STM measurements indicate a ripening of the Pd clusters, even under these mild reaction conditions to 500 K. However, the sintering is not induced by the presence of the adsorbates, as the cluster distribution appears as after thermal annealing experiments [45, 46].

Next to integral measurements on the reactivity of Pd clusters, the underlying processes have to be investigated on the local scale for a complete description of catalytic activity. While maintaining atomic resolution, temporal resolutions up to 8 frames/s have been achieved routinely. With this time scale, many surface processes with activation barriers between 0.3 and 0.7 eV can be accessed within the temperature range between 150 K and 800 K that can be reached with a variable temperature STM. For this purpose, the Omicron VT AFM has been equipped within this thesis with an add-on instrument that allows to investigate the cluster dynamics under reaction conditions. The implementation is described in detail in chapter 6 and comprises, inter alia, hardware modifications of the conventional STM electronics, a thorough eigenfrequency characterization of the microscope, a LabVIEW based control software in combination with a sophisticated processing routine for huge data sets. A quick switching between conventional STM and FAST measurements can be performed on the fly. Initially, the add-on instrument is characterized by measuring the static h-BN/Rh(111) surface with its well-known long range periodicity. First measurements with stable single and double layer high Pd clusters on the moiré superstructure show the potential of this technique to measure dynamics of nanoparticles even at the required critical current setpoints of $\geq$150 pA. Additionally, the add-on instrument is capable of atomic resolution as demonstrated on bare Rh(111). Chapter 7 focuses on the mobility of Pd nanoparticles on h-BN/Rh(111), whose rings of in-plane dipoles can trap molecules and atoms [66]. This spacial confinement protects particles from long range migration and trapping on defects and enables the investigation of equilibrium processes, facilitating measurements with the FAST module. Two examples of longer time series are discussed in detail, in particular the diffusion of small clusters and that of atoms. While double layer high Pd_{12} clusters turned out to be still too immobile, even at temperatures up to 375 K, mobile single layer high fragments could be generated in situ, which diffuse within a moiré trough and could be monitored over a time span of 3 hours with a time resolution of 125 ms. A thorough analysis of the spatial distribution of the particles geometric center reveals a pronounced six fold symmetry with lateral distances of 2.5 Å that is rotated by 30° with respect to the h-BN/Rh(111) nanomesh. An evaluation of the residence times indicates the occurrence of diffusion events on two different time scales. The jump frequency is much higher within three distinct pairs of the hexagonal arranged sites with a residence time in the order of the frame rate. However, the diffusion between those three pairs is much slower with a residence time of about 15 frames. In addition, the diffusion behaviour of the particle could be systematically analyzed. It is not altered at current setpoints up to 1 nA and at bias voltages in the range of ±1.0 V. Higher positive and negative voltages lead to an increasingly fuzzy image appearance, which is most probably field-induced. A second example focusses on the mobility of Pd atoms in the troughs of the h-BN/Rh(111) nanomesh. These atoms are highly mobile on the surface, as can be seen by a broad cluster size distribution at room temperature. The ripening processes can be suppressed by cooling to 118 K during deposition and STM measurements. Ring-like structures appear in conventional STM measurements after heating up to 168 K. Only the enhanced temporal resolution of the FAST technique can reveal the circular motion of the particles trapped in the troughs of the moiré superstructure.

A. Appendix

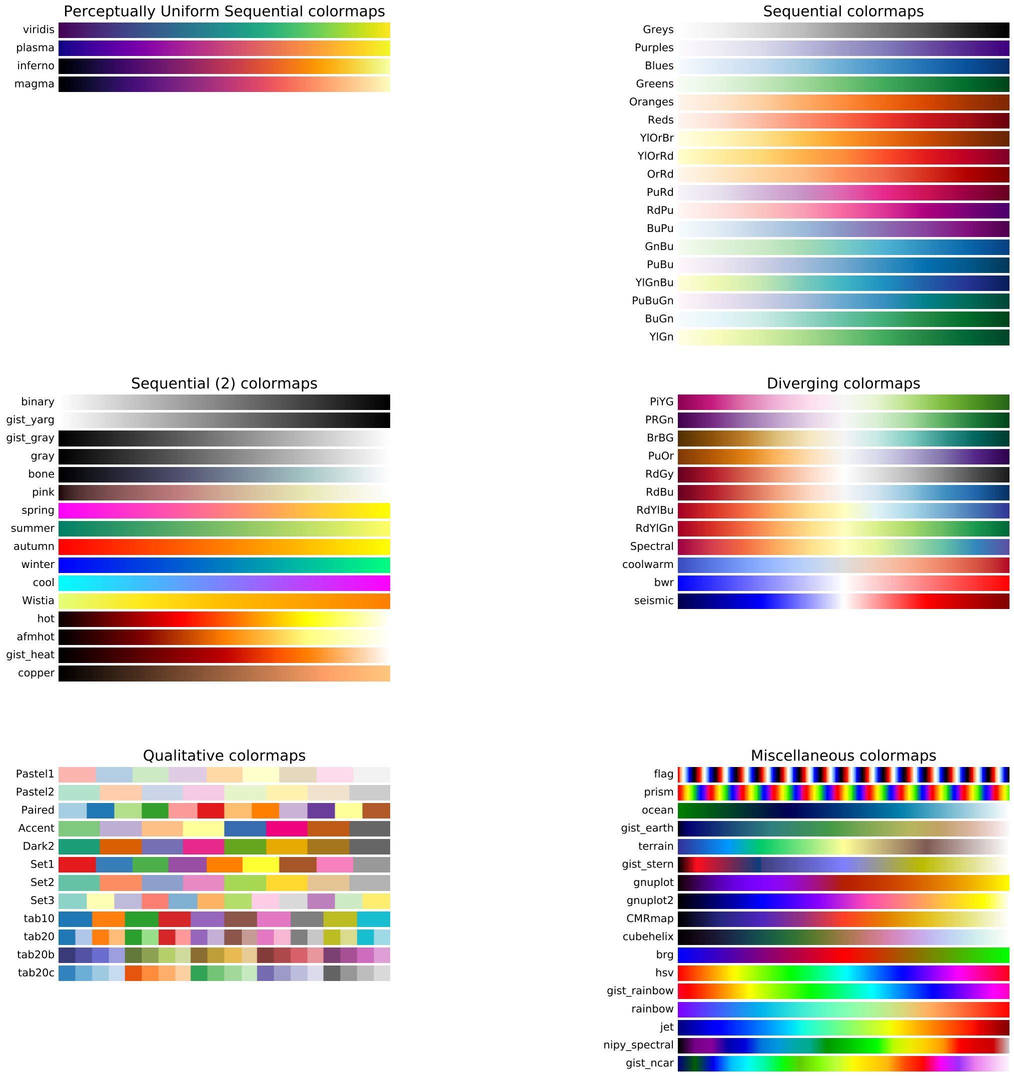

Figure A.1.: Colormap options in the matplotlib plotting library.

Bibliography

[1] I. Dincer, “Renewable energy and sustainable development: a crucial review,” *Renewable and Sustainable Energy Reviews*, vol. 4, no. 2, pp. 157–175, 2000.

[2] I. Chorkendorff and J. W. Niemantsverdriet, *Concepts of Modern Catalysis and Kinetics.* Weinheim: Wiley-VCH Verlag GmbH & Co. KGaA, 2nd ed., 2007.

[3] R. Schlögl, “Heterogeneous Catalysis,” *Angewandte Chemie International Edition*, vol. 54, no. 11, pp. 3465–3520, 2015.

[4] G. Ertl, “Reactions at Surfaces: From Atoms to Complexity (Nobel Lecture),” *Angewandte Chemie International Edition*, vol. 47, no. 19, pp. 3524–3535, 2008.

[5] B. M. Bhanage and M. Arai, “Catalyst product separation techniques in Heck reaction,” *Catalysis Reviews*, vol. 43, no. 3, pp. 315–344, 2001.

[6] Yin and J. Liebscher, “Carbon-Carbon Coupling Reactions Catalyzed by Heterogeneous Palladium Catalysts,” *Chemical Reviews*, vol. 107, no. 1, pp. 133–173, 2007.

[7] C. R. Henry, “Surface studies of supported model catalysts,” *Surface Science Reports*, vol. 31, no. 7-8, pp. 231–325, 1998.

[8] I. Langmuir, “Part II.—“Heterogeneous reactions”. Chemical reactions on surfaces,” *Trans. Faraday Soc.*, vol. 17, no. 1897, pp. 607–620, 1922.

[9] M. Boudart, “Model catalysts: reductionism for understanding,” *Topics in Catalysis*, vol. 13, no. 1, p. 147, 2000.

[10] C. R. Henry, “2D-Arrays of Nanoparticles as Model Catalysts,” *Catalysis Letters*, vol. 145, no. 3, pp. 731–749, 2015.

[11] G. A. Somorjai, H. Frei, and J. Y. Park, “Advancing the Frontiers in Nanocatalysis, Biointerfaces, and Renewable Energy Conversion by Innovations of Surface Techniques,” *Journal of the American Chemical Society*, vol. 131, no. 46, pp. 16589–16605, 2009.

[12] U. Heiz and U. Landman, eds., *Nanocatalysis.* Nanoscience and Technology, Berlin, Heidelberg: Springer Berlin Heidelberg, 2007.

[13] K. Bromann, C. Félix, H. Brune, W. Harbich, R. Monot, J. Buttet, and K. Kern, "Controlled Deposition of Size-Selected Silver Nanoclusters," *Science*, vol. 274, no. 5289, pp. 956–958, 1996.

[14] U. Heiz, F. Vanolli, L. Trento, and W.-D. Schneider, "Chemical reactivity of size-selected supported clusters: An experimental setup," *Review of Scientific Instruments*, vol. 68, no. 5, pp. 1986–1994, 1997.

[15] U. Heiz, A. Vayloyan, and E. Schumacher, "A new cluster source for the generation of binary metal clusters," *Review of Scientific Instruments*, vol. 68, no. 10, pp. 3718–3722, 1997.

[16] U. Heiz, A. Sanchez, S. Abbet, and W. D. Schneider, "Catalytic oxidation of carbon monoxide on monodispersed platinum clusters: Each atom counts," *Journal of the American Chemical Society*, vol. 121, no. 13, pp. 3214–3217, 1999.

[17] U. Heiz, A. Sanchez, S. Abbet, and W.-D. Schneider, "Tuning the oxidation of carbon monoxide using nanoassembled model catalysts," *Chemical Physics*, vol. 262, no. 1, pp. 189–200, 2000.

[18] A. Sanchez, S. Abbet, U. Heiz, W.-D. Schneider, H. Häkkinen, R. N. Barnett, and U. Landman, "When Gold Is Not Noble: Nanoscale Gold Catalysts," *The Journal of Physical Chemistry A*, vol. 103, no. 48, pp. 9573–9578, 1999.

[19] B. Yoon, H. Häkkinen, U. Landman, A. S. Wörz, J.-M. Antonietti, S. Abbet, K. Judai, and U. Heiz, "Charging effects on bonding and catalyzed oxidation of CO on Au_8 clusters on MgO," *Science*, vol. 307, no. 5708, pp. 403–7, 2005.

[20] D. Goodman, "Model catalysts: from imagining to imaging a working surface," *Journal of Catalysis*, vol. 216, no. 1-2, pp. 213–222, 2003.

[21] A. Piednoir, E. Perrot, S. Granjeaud, A. Humbert, C. Chapon, and C. Henry, "Atomic resolution on small three-dimensional metal clusters by STM," *Surface Science*, vol. 391, no. 1-3, pp. 19–26, 1997.

[22] K. H. Hansen, T. Worren, S. Stempel, E. Lægsgaard, M. Bäumer, H.-J. Freund, F. Besenbacher, and I. Stensgaard, "Palladium Nanocrystals on Al_2O_3: Structure and Adhesion Energy," *Physical Review Letters*, vol. 83, no. 20, pp. 4120–4123, 1999.

[23] P. L. Hansen, J. B. Wagner, S. Helveg, J. R. Rostrup-Nielsen, B. S. Clausen, and H. Topsøe, "Atom-resolved imaging of dynamic shape changes in supported copper nanocrystals.," *Science*, vol. 295, no. 5562, pp. 2053–5, 2002.

[24] G. S. Parkinson, Z. Novotny, G. Argentero, M. Schmid, J. Pavelec, R. Kosak, P. Blaha, and U. Diebold, "Carbon monoxide-induced adatom sintering in a Pd–Fe3O4 model catalyst," *Nature Materials*, vol. 12, no. 8, pp. 724–728, 2013.

[25] Y. Ding, M. Iannuzzi, and J. Hutter, "Investigation of Boron Nitride Nanomesh Interacting with Water," *The Journal of Physical Chemistry C*, vol. 115, no. 28, pp. 13685–13692, 2011.

[26] J. Tsuji, *Palladium Reagents and Catalysts*, vol. 9. Chichester, UK: John Wiley & Sons, Ltd, 2004.

[27] N. Itoh, E. Tamura, S. Hara, T. Takahashi, A. Shono, K. Satoh, and T. Namba, "Hydrogen recovery from cyclohexane as a chemical hydrogen carrier using a palladium membrane reactor," *Catalysis Today*, vol. 82, no. 1-4, pp. 119–125, 2003.

[28] B. Brandt, J.-h. Fischer, W. Ludwig, J. Libuda, F. Zaera, S. Schauermann, and H.-j. Freund, "Isomerization and Hydrogenation of cis-2-Butene on Pd Model Catalyst," *The Journal of Physical Chemistry C*, vol. 112, no. 30, pp. 11408–11420, 2008.

[29] S. S. Stahl, "Palladium-Catalyzed Oxidation of Organic Chemicals with O_2," *Science*, vol. 309, no. 5742, pp. 1824–1826, 2005.

[30] Y. Nishihata, J. Mizuki, T. Akao, H. Tanaka, M. Uenishi, M. Kimura, T. Okamoto, and N. Hamada, "Self-regeneration of a Pd-perovskite catalyst for automotive emissions control," *Nature*, vol. 418, no. 6894, pp. 164–167, 2002.

[31] D. T. Sawyer and L. V. Interrante, "Electrochemistry of dissolved gases," *Journal of Electroanalytical Chemistry*, vol. 2, no. 4, pp. 310–327, 1961.

[32] K. Umakoshi, A. Ichimura, I. Kinoshita, and S. Ooi, "The dinuclear palladium(II) complex of pyridine-2-thiol. Synthesis, structure, and electrochemistry," *Inorganic Chemistry*, vol. 29, no. 20, pp. 4005–4010, 1990.

[33] Y.-F. Yang, Y.-H. Zhou, and C.-S. Cha, "Electrochemical reduction of oxygen on small palladium particles supported on carbon in alkaline solution," *Electrochimica Acta*, vol. 40, no. 16, pp. 2579–2586, 1995.

[34] R. Pattabiraman, "Electrochemical investigations on carbon supported palladium catalysts," *Applied Catalysis A: General*, vol. 153, no. 1-2, pp. 9–20, 1997.

[35] F. P. Zamborini, S. M. Gross, and R. W. Murray, "Synthesis, Characterization, Reactivity and Electrochemistry of Palladium Monolayer Protected Clusters," *Langmuir*, vol. 17, no. 2, pp. 481–488, 2001.

[36] R. Singh, A. Singh, and Anindita, "Electrocatalytic activity of binary and ternary composite films of Pd, MWCNT and Ni, Part II: Methanol electrooxidation in 1M KOH," *International Journal of Hydrogen Energy*, vol. 34, no. 4, pp. 2052–2057, 2009.

[37] P. G. Simmonds, G. R. Shoemake, and J. E. Lovelock, “Palladium-hydrogen system. Efficient interface for gas chromatography-mass spectrometry,” *Analytical Chemistry*, vol. 42, no. 8, pp. 881–885, 1970.

[38] F. Favier, E. C. Walter, M. P. Zach, T. Benter, and R. M. Penner, “Hydrogen sensors and switches from electrodeposited palladium mesowire arrays.,” *Science*, vol. 293, no. 5538, pp. 2227–31, 2001.

[39] S. Mubeen, T. Zhang, B. Yoo, M. A. Deshusses, and N. V. Myung, “Palladium Nanoparticles Decorated Single-Walled Carbon Nanotube Hydrogen Sensor,” *The Journal of Physical Chemistry C*, vol. 111, no. 17, pp. 6321–6327, 2007.

[40] N. T. S. Phan, M. Van Der Sluys, and C. W. Jones, “On the Nature of the Active Species in Palladium Catalyzed Mizoroki–Heck and Suzuki–Miyaura Couplings – Homogeneous or Heterogeneous Catalysis, A Critical Review,” *Advanced Synthesis & Catalysis*, vol. 348, no. 6, pp. 609–679, 2006.

[41] P. Feulner and D. Menzel, “Simple ways to improve ”flash desorption” measurements from single crystal surfaces,” *Journal of Vacuum Science and Technology*, vol. 17, no. 2, p. 662, 1980.

[42] H. Conrad, G. Ertl, and J. Küppers, “Interactions between oxygen and carbon monoxide on a Pd(111) surface,” *Surface Science*, vol. 76, no. 2, pp. 323–342, 1978.

[43] S. Shaikhutdinov, M. Heemeier, M. Bäumer, T. Lear, D. Lennon, R. Oldman, S. Jackson, and H.-J. Freund, “Structure–Reactivity Relationships on Supported Metal Model Catalysts: Adsorption and Reaction of Ethene and Hydrogen on Pd/Al_2O_3/NiAl(110),” *Journal of Catalysis*, vol. 200, no. 2, pp. 330–339, 2001.

[44] A. Doyle, S. K. Shaikhutdinov, and H.-J. Freund, “Alkene chemistry on the palladium surface: nanoparticles vs single crystals,” *Journal of Catalysis*, vol. 223, no. 2, pp. 444–453, 2004.

[45] Y. Fukamori, M. König, B. Yoon, B. Wang, F. Esch, U. Heiz, and U. Landman, “Fundamental insight into the substrate-dependent ripening of monodisperse Clusters,” *ChemCatChem*, vol. 5, no. 11, pp. 3330–3341, 2013.

[46] M. König, *Scanning Probe Microscopy of size-selected, supported clusters: The cluster-support interaction.* PhD thesis, 2015.

[47] S. Horch, H. T. Lorensen, S. Helveg, E. Lægsgaard, I. Stensgaard, K. W. Jacobsen, J. K. Nørskov, and F. Besenbacher, “Enhancement of surface self-diffusion of platinum aroms by adsorbed hydrogen,” *Nature*, vol. 398, no. 6723, pp. 134–136, 1999.

[48] R. Bliem, J. van der Hoeven, A. Zavodny, O. Gamba, J. Pavelec, P. E. de Jongh, M. Schmid, U. Diebold, and G. S. Parkinson, "An Atomic-Scale View of CO and H_2 Oxidation on a Pt/Fe_3O_4 Model Catalyst," *Angewandte Chemie International Edition*, vol. 54, no. 47, pp. 13999–14002, 2015.

[49] D. W. Pohl and R. Möller, ""Tracking" tunneling microscopy," *Review of Scientific Instruments*, vol. 59, no. 6, pp. 840–842, 1988.

[50] B. S. Swartzentruber, "Direct Measurement of Surface Diffusion Using Atom-Tracking Scanning Tunneling Microscopy," *Physical Review Letters*, vol. 76, no. 3, pp. 459–462, 1996.

[51] Y. Fukamori, *Static and dynamic characterization of size-selected cluster diffusion and ripening on periodically wettable surfaces.* PhD thesis, 2016.

[52] A. Bryant, D. P. E. Smith, and C. F. Quate, "lmaging in Real Time with the Tunneling Microscope," *Applied Physics Letters*, vol. 48, no. February, p. 832, 1986.

[53] F. Esch, C. Dri, A. Spessot, C. Africh, G. Cautero, D. Giuressi, R. Sergo, R. Tommasini, and G. Comelli, "The FAST module: An add-on unit for driving commercial scanning probe microscopes at video rate and beyond," *Review of Scientific Instruments*, vol. 82, no. 5, 2011.

[54] C. Dri, F. Esch, C. Africh, and G. Comelli, "How to select fast scanning frequencies for high-resolution fast STM measurements with a conventional microscope," *Measurement Science and Technology*, vol. 23, no. 5, p. 055402, 2012.

[55] M. Bieletzki, *Charakterisierung dünner MgO-Filme auf Ag(001) und massenselektierter Cluster auf HOPG mittels Rastersondentechnik.* PhD thesis, 2009.

[56] V. Pishchik, L. A. Lytvynov, and E. R. Dobrovinskaya, *Sapphire.* Springer, 2009.

[57] M. Corso, W. Auwärter, M. Muntwiler, A. Tamai, T. Greber, and J. Osterwalder, "Boron nitride nanomesh.," *Science*, vol. 303, no. 5655, pp. 217–20, 2004.

[58] S. Berner, M. Corso, R. Widmer, O. Groening, R. Laskowski, P. Blaha, K. Schwarz, A. Goriachko, H. Over, S. Gsell, M. Schreck, H. Sachdev, T. Greber, and J. Osterwalder, "Boron Nitride Nanomesh: Functionality from a Corrugated Monolayer," *Angewandte Chemie International Edition*, vol. 46, no. 27, pp. 5115–5119, 2007.

[59] R. Laskowski, P. Blaha, T. Gallauner, and K. Schwarz, "Single-Layer Model of the Hexagonal Boron Nitride Nanomesh on the Rh(111) Surface," *Physical Review Letters*, vol. 98, no. 10, p. 106802, 2007.

[60] R. Laskowski, P. Blaha, and K. Schwarz, “Bonding of hexagonal BN to transition metal surfaces: An ab initio density-functional theory study,” *Physical Review B*, vol. 78, no. 4, p. 045409, 2008.

[61] O. Bunk, M. Corso, D. Martoccia, R. Herger, P. Willmott, B. Patterson, J. Osterwalder, J. van der Veen, and T. Greber, “Surface X-ray diffraction study of boron-nitride nanomesh in air,” *Surface Science*, vol. 601, pp. L7–L10, jan 2007.

[62] I. Brihuega, C. H. Michaelis, J. Zhang, S. Bose, V. Sessi, J. Honolka, M. Alexander Schneider, A. Enders, and K. Kern, “Electronic decoupling and templating of Co nanocluster arrays on the boron nitride nanomesh,” *Surface Science*, vol. 602, no. 14, pp. L95–L99, 2008.

[63] A. B. Preobrajenski, A. S. Vinogradov, M. L. Ng, E. Ćavar, R. Westerström, A. Mikkelsen, E. Lundgren, and N. Mårtensson, “Influence of chemical interaction at the lattice-mismatched h-BN/Pt (111) interfaces on the overlayer morphology,” *Physical Review B - Condensed Matter and Materials Physics*, vol. 75, no. 24, pp. 1–8, 2007.

[64] Y. Lin and J. W. Connell, “Advances in 2D boron nitride nanostructures: nanosheets, nanoribbons, nanomeshes, and hybrids with graphene,” *Nanoscale*, vol. 4, no. 22, p. 6908, 2012.

[65] R. Laskowski and P. Blaha, “Ab initio study of h-BN nanomeshes on Ru(001), Rh(111), and Pt(111),” *Physical Review B*, vol. 81, no. 7, p. 075418, 2010.

[66] H. Dil, J. Lobo-Checa, R. Laskowski, P. Blaha, S. Berner, J. Osterwalder, and T. Greber, “Surface Trapping of Atoms and Molecules with Dipole Rings,” *Science*, vol. 319, no. 5871, pp. 1824–1826, 2008.

[67] P. Bacle, A. P. Seitsonen, M. Iannuzzi, and J. Hutter, “Chemical Reactions on Metal-supported Hexagonal Boron Nitride Investigated with Density Functional Theory,” *CHIMIA International Journal for Chemistry*, vol. 68, no. 9, pp. 596–601, 2014.

[68] R. Widmer, D. Passerone, T. Mattle, H. Sachdev, and O. Gröning, “Probing the selectivity of a nanostructured surface by xenon adsorption,” *Nanoscale*, vol. 2, no. 4, p. 502, 2010.

[69] F. D. Natterer, F. Patthey, and H. Brune, “Ring State for Single Transition Metal Atoms on Boron Nitride on Rh(111),” *Physical Review Letters*, vol. 109, no. 6, p. 066101, 2012.

[70] J. Zhang, V. Sessi, C. H. Michaelis, I. Brihuega, J. Honolka, K. Kern, R. Skomski, X. Chen, G. Rojas, and A. Enders, “Ordered layers of Co clusters on BN template layers,” *Physical Review B*, vol. 78, no. 16, p. 165430, 2008.

[71] H. Ma, T. Brugger, S. Berner, Y. Ding, M. Iannuzzi, J. Hutter, J. Osterwalder, and T. Greber, “Nano-ice on Boron Nitride Nanomesh: Accessing Proton Disorder,” *ChemPhysChem*, vol. 11, no. 2, pp. 399–403, 2010.

[72] W. Orellana and H. Chacham, “Stability of native defects in hexagonal and cubic boron nitride,” *Physical Review B*, vol. 63, no. 12, p. 125205, 2001.

[73] W. Auwärter, M. Muntwiler, J. Osterwalder, and T. Greber, “Defect lines and two-domain structure of hexagonal boron nitride films on Ni(111),” *Surface Science*, vol. 545, no. 1-2, pp. L735–L740, 2003.

[74] G. B. Grad, P. Blaha, K. Schwarz, W. Auwärter, and T. Greber, “Density functional theory investigation of the geometric and spintronic structure of h -BN/Ni(111) in view of photoemission and STM experiments,” *Physical Review B*, vol. 68, no. 8, p. 085404, 2003.

[75] F. Natterer, F. Patthey, and H. Brune, “Quantifying residual hydrogen adsorption in low-temperature STMs,” *Surface Science*, vol. 615, pp. 80–87, 2013.

[76] J. Kotakoski, C. H. Jin, O. Lehtinen, K. Suenaga, and A. V. Krasheninnikov, “Electron knock-on damage in hexagonal boron nitride monolayers,” *Physical Review B*, vol. 82, no. 11, p. 113404, 2010.

[77] H. Cun, M. Iannuzzi, A. Hemmi, S. Roth, J. Osterwalder, and T. Greber, “Immobilizing Individual Atoms beneath a Corrugated Single Layer of Boron Nitride,” *Nano Letters*, vol. 13, no. 5, pp. 2098–2103, 2013.

[78] L. H. de Lima, H. Y. Cun, A. Hemmi, T. Kälin, and T. Greber, “Note: An ion source for alkali metal implantation beneath graphene and hexagonal boron nitride monolayers on transition metals,” *Review of Scientific Instruments*, vol. 84, no. 12, p. 126104, 2013.

[79] D. A. Shirley, “High-Resolution X-Ray Photoemission Spectrum of the Valence Bands of Gold,” *Physical Review B*, vol. 5, no. 12, pp. 4709–4714, 1972.

[80] J. Végh, “The Shirley background revised,” *Journal of Electron Spectroscopy and Related Phenomena*, vol. 151, no. 3, pp. 159–164, 2006.

[81] J. Végh, “The Shirley-equivalent electron inelastic scattering cross-section function,” *Surface Science*, vol. 563, no. 1-3, pp. 183–190, 2004.

[82] J. Végh, “On analyzing the intrinsic processes through the Shirley background correction procedure,” *Surface Science*, vol. 577, no. 2-3, pp. 220–228, 2005.

[83] J. T. Yates, E. D. Williams, and W. H. Weinberg, “Does chemisorbed carbon monoxide dissociate on rhodium?,” *Surface Science*, vol. 91, no. 2-3, pp. 562–570, 1980.

[84] S. Schwegmann, H. Over, V. De Renzi, and G. Ertl, "The atomic geometry of the O and CO + O phases on Rh(111)," *Surface Science*, vol. 375, no. 1, pp. 91–106, 1997.

[85] S. Schwegmann and H. Over, "Comment on "STM study of oxygen on Rh(111)" by H. Xu and K.Y.S. Ng," *Surface Science*, vol. 393, no. 1-3, pp. 179–180, 1997.

[86] S. Marchini, C. Sachs, and J. Wintterlin, "STM investigation of the (2x2)O and (2x1)O structures on Rh(111)," *Surface Science*, vol. 592, no. 1-3, pp. 58–64, 2005.

[87] P. Thiel, J. Yates, and W. Weinberg, "The interaction of oxygen with the Rh(111) surface a," *Surface Science*, vol. 82, no. 1, pp. 22–44, 1979.

[88] P. A. Thiel, E. D. Williams, J. T. Yates, and W. H. Weinberg, "The chemisorption of CO on Rh(111)," *Surface Science*, vol. 84, no. 1, pp. 54–64, 1979.

[89] D. Castner, B. Sexton, and G. Somorjai, "LEED and thermal desorption studies of small molecules (H_2, O_2, CO, CO_2, NO, C_2H_4, C_2H_2 and C) chemisorbed on the rhodium (111) and (100) surfaces," *Surface Science*, vol. 71, no. 3, pp. 519–540, 1978.

[90] J. Yates, P. Thiel, and W. Weinberg, "The chemisorption of hydrogen on Rh(111)," *Surface Science*, vol. 84, no. 2, pp. 427–439, 1979.

[91] J. Colonell, T. Curtiss, and S. Sibener, "Coverage dependence of the kinetics for H_2 desorption from Rh(111)," *Surface Science*, vol. 366, no. 1, pp. 19–28, 1996.

[92] M. Fukuoka, M. Okada, M. Matsumoto, S. Ogura, K. Fukutani, and T. Kasai, "Location of hydrogen adsorbed on Rh(111) studied by low-energy electron diffraction and nuclear reaction analysis," *Physical Review B - Condensed Matter and Materials Physics*, vol. 75, no. 23, pp. 1–9, 2007.

[93] Stanford Research Systems, *Operating Manual and Programming Reference Models RGA100, RGA200 and RGA300 Residual Gas Analyzer.* 2009.

[94] L. H. Dubois, D. G. Castner, and G. A. Somorjai, "The chemisorption of acetylene and ethylene on Rh(111): A low energy electron diffraction (LEED), high resolution electron energy loss (ELS), and thermal desorption mass spectrometry (TDS) study," *The Journal of Chemical Physics*, vol. 72, no. 9, pp. 5234–5240, 1980.

[95] R. Koestner, M. Van Hove, and G. Somorjai, "A LEED crystallography study of the (2×2)-C_2H_3 structure obtained after ethylene adsorption on Rh(111)," *Surface Science*, vol. 121, no. 2, pp. 321–337, 1982.

[96] F. Muntean, “Transmission study for r.f.-only quadrupoles by computer simulation,” *International Journal of Mass Spectrometry and Ion Processes*, vol. 151, no. 2-3, pp. 197–206, 1995.

[97] P. H. Dawson, *Quadrupole Mass Spectrometry and its Applications.* Elsevier, 1976.

[98] T. Engel and G. Ertl, “A molecular beam investigation of the catalytic oxidation of CO on Pd (111),” *The Journal of Chemical Physics*, vol. 69, no. 3, p. 1267, 1978.

[99] X. Guo and J. T. Yates, “Dependence of effective desorption kinetic parameters on surface coverage and adsorption temperature: CO on Pd(111),” *The Journal of Chemical Physics*, vol. 90, no. 11, pp. 6761–6766, 1989.

[100] R. Meyer, D. Lahav, T. Schalow, M. Laurin, B. Brandt, S. Schauermann, S. Guimond, T. Klüner, H. Kuhlenbeck, J. Libuda, S. Shaikhutdinov, and H.-J. Freund, “CO adsorption and thermal stability of Pd deposited on a thin FeO(111) film,” *Surface Science*, vol. 586, no. 1-3, pp. 174–182, 2005.

[101] I. Stará and V. Matolín, “The influence of particle size on CO adsorption on Pd/alumina model catalysts,” *Surface Science*, vol. 313, no. 1-2, pp. 99–106, 1994.

[102] I. Stará, V. Nehasil, and V. Matolín, “The influence of particle size on CO oxidation on Pd/alumina model catalyst,” *Surface Science*, vol. 331-333, no. pt A, pp. 173–177, 1995.

[103] S. M. Lang, I. Fleischer, T. M. Bernhardt, R. N. Barnett, and U. Landman, “Low-Temperature CO Oxidation Catalyzed by Free Palladium Clusters: Similarities and Differences to Pd Surfaces and Supported Particles,” *ACS Catalysis*, vol. 5, no. 4, pp. 2275–2289, 2015.

[104] S. Kunz, F. F. Schweinberger, V. Habibpour, M. Röttgen, C. Harding, M. Arenz, and U. Heiz, “Temperature Dependent CO Oxidation Mechanisms on Size-Selected Clusters,” *The Journal of Physical Chemistry C*, vol. 114, no. 3, pp. 1651–1654, 2010.

[105] S. Shaikhutdinov, M. Heemeier, J. Hoffmann, I. Meusel, B. Richter, M. Bäumer, H. Kuhlenbeck, J. Libuda, H.-J. Freund, R. Oldman, S. Jackson, C. Konvicka, M. Schmid, and P. Varga, “Interaction of oxygen with palladium deposited on a thin alumina film,” *Surface Science*, vol. 501, no. 3, pp. 270–281, 2002.

[106] X. Xu and D. W. Goodman, “An infrared and kinetic study of CO oxidation on model silica-supported palladium catalysts from 10-9 to 15 torr,” *Journal of Physical Chemistry*, vol. 97, pp. 7711–7718, 1993.

[107] A. H. M. A. Wasey, S. Chakrabarty, G. P. Das, and C. Majumder, “h -BN Monolayer on the Ni(111) Surface: A Potential Catalyst for Oxidation,” *ACS Applied Materials & Interfaces*, vol. 5, no. 21, pp. 10404–10408, 2013.

[108] E. Stuve, R. Madix, and C. Brundle, “The adsorption and reaction of ethylene on clean and oxygen covered Pd(100),” *Surface Science*, vol. 152-153, no. 100, pp. 532–542, 1985.

[109] W. T. Tysoe, G. L. Nyberg, and R. M. Lambert, “Structural, kinetic, and reactive properties of the palladium(111)-ethylene system,” *The Journal of Physical Chemistry*, vol. 88, no. 10, pp. 1960–1963, 1984.

[110] T. Sekitani, T. Takaoka, M. Fujisawa, and M. Nishijima, “Interaction of ethylene with the hydrogen-preadsorbed palladium (110) surface: hydrogenation and hydrogen-deuterium-exchange reactions,” *The Journal of Physical Chemistry*, vol. 96, no. 21, pp. 8462–8468, 1992.

[111] L. Burkholder, D. Stacchiola, and W. T. Tysoe, “Kinetic and reactive properties of ethylene on clean and hydrogen-covered Pd(111),” *Surface Review and Letters*, vol. 10, no. 06, pp. 909–916, 2003.

[112] S. Shaikhutdinov, M. Frank, M. Bäumer, S. Jackson, R. Oldman, J. Hemminger, and H.-J. Freund, “Effect of carbon deposits on reactivity of supported Pd model catalysts,” *Catalysis Letters*, vol. 80, no. 3-4, pp. 115–122, 2002.

[113] M. Bäumer and H.-J. Freund, “Metal deposits on well-ordered oxide films,” *Progress in Surface Science*, vol. 61, no. 7-8, pp. 127–198, 1999.

[114] D. Stacchiola, S. Azad, L. Burkholder, and W. T. Tysoe, “An Investigation of the Reaction Pathway for Ethylene Hydrogenation on Pd(111),” *The Journal of Physical Chemistry B*, vol. 105, no. 45, pp. 11233–11239, 2001.

[115] X. Guo and R. Madix, “Selective Hydrogenation and H-D Exchange of Unsaturated Hydrocarbons on Pd(100)-P(1x1)-H(D),” *Journal of Catalysis*, vol. 155, no. 2, pp. 336–344, 1995.

[116] N. Vasquez and R. Madix, “Reactivity of Unsaturated Linear C6 Hydrocarbons on Pd(111) and H(D)/Pd(111),” *Journal of Catalysis*, vol. 178, no. 1, pp. 234–252, 1998.

[117] D. Stacchiola, L. Burkholder, and W. T. Tysoe, “Ethylene adsorption on Pd(111) studied using infrared reflection-absorption spectroscopy,” *Surface Science*, vol. 511, no. 1-3, pp. 215–228, 2002.

[118] A. M. Doyle, S. K. Shaikhutdinov, S. D. Jackson, and H.-J. Freund, “Hydrogenation on Metal Surfaces: Why are Nanoparticles More Active than Single Crystals?,” *Angewandte Chemie International Edition*, vol. 42, no. 42, pp. 5240–5243, 2003.

[119] M. S. Daw and S. M. Foiles, “Theory of subsurface occupation, ordered structures, and order-disorder transitions for hydrogen on Pd(111),” *Physical Review B*, vol. 35, no. 5, pp. 2128–2136, 1987.

[120] L. P. Wang, W. T. Tysoe, R. M. Ormerod, R. M. Lambert, H. Hoffmann, and F. Zaera, “Determination of the Bonding and Orientation of Ethylene on Pd(111) by Near-Edge X-ray Absorption Fine Structure and Photoelectron Spectroscopy,” *The Journal of Physical Chemistry*, vol. 94, pp. 4236–4239, may 1990.

[121] M. Frank, R. Kühnemuth, M. Bäumer, and H.-J. Freund, “Oxide-supported Rh particle structure probed with carbon monoxide,” *Surface Science*, vol. 427-428, pp. 288–293, 1999.

[122] M. Frank and M. Bäumer, “From atoms to crystallites: adsorption on oxide-supported metal particles,” *Physical Chemistry Chemical Physics*, vol. 2, no. 17, pp. 3723–3737, 2000.

[123] A. Binder, M. Seipenbusch, M. Muhler, and G. Kasper, “Kinetics and particle size effects in ethene hydrogenation over supported palladium catalysts at atmospheric pressure,” *Journal of Catalysis*, vol. 268, no. 1, pp. 150–155, 2009.

[124] R. Behm, K. Christmann, and G. Ertl, “Adsorption of hydrogen on Pd(100),” *Surface Science*, vol. 99, no. 2, pp. 320–340, 1980.

[125] G. Gdowski, T. Felter, and R. Stulen, “Effect of surface temperature on the sorption of hydrogen by Pd(111),” *Surface Science Letters*, vol. 181, no. 3, pp. L147–L155, 1987.

[126] D. Farías, M. Patting, and K. H. Rieder, “Helium Diffraction Investigations of the Transition of Chemisorbed Hydrogen into Subsurface Sites on Palladium Surfaces,” *physica status solidi (a)*, vol. 159, no. 1, pp. 255–262, 1997.

[127] H. Okuyama, W. Siga, N. Takagi, M. Nishijima, and T. Aruga, “Path and mechanism of hydrogen absorption at Pd(100),” *Surface Science*, vol. 401, no. 3, pp. 344–354, 1998.

[128] W. Ludwig, A. Savara, R. J. Madix, S. Schauermann, and H.-J. Freund, “Subsurface Hydrogen Diffusion into Pd Nanoparticles: Role of Low-Coordinated Surface Sites and Facilitation by Carbon,” *The Journal of Physical Chemistry C*, vol. 116, no. 5, pp. 3539–3544, 2012.

[129] B. D. Kay, C. H. F. Peden, and D. W. Goodman, “Kinetics of hydrogen absorption by Pd(110),” *Physical Review B*, vol. 34, no. 2, pp. 817–822, 1986.

[130] B. Wang, B. Yoon, M. König, Y. Fukamori, F. Esch, U. Heiz, and U. Landman, “Size-selected monodisperse nanoclusters on supported graphene:

Bonding, isomerism, and mobility," *Nano Letters*, vol. 12, no. 11, pp. 5907–5912, 2012.

[131] A. S. Crampton, M. D. Rötzer, F. F. Schweinberger, B. Yoon, U. Landman, and U. Heiz, "Ethylene hydrogenation on supported Ni, Pd and Pt nanoparticles: Catalyst activity, deactivation and the d-band model," *Journal of Catalysis*, vol. 333, pp. 51–58, jan 2016.

[132] G. Binnig, H. Rohrer, C. Gerber, and E. Weibel, "Tunneling through a controllable vacuum gap," *Applied Physics Letters*, vol. 40, no. 2, pp. 178–180, 1982.

[133] G. Binnig, H. Rohrer, C. Gerber, and E. Weibel, "Surface Studies by Scanning Tunneling Microscopy," 1982.

[134] G. Binnig, H. Rohrer, C. Gerber, and E. Weibel, "7x7 Reconstruction on Si(111) Resolved in Real Space," *Physical Review Letters*, vol. 50, no. 2, pp. 120–123, 1983.

[135] S. Hosaka, T. Hasegawa, S. Hosoki, and K. Takata, "Fast scanning tunneling microscope for dynamic observation," *Review of Scientific Instruments*, vol. 61, no. 4, pp. 1342–1343, 1990.

[136] C. Ludwig, B. Gompf, W. Glatz, J. Petersen, W. Eisenmenger, M. Möbus, U. Zimmermann, and N. Karl, "Video-STM, LEED and X-ray diffraction investigations of PTCDA on graphite," *Zeitschrift für Physik B Condensed Matter*, vol. 86, pp. 397–404, oct 1992.

[137] R. Kliese, B. Röttger, D. Badt, and H. Neddermeyer, "Real-time STM investigation of the initial stages of oxygen interaction with Si(100)2×1," *Ultramicroscopy*, vol. 42-44, no. PART 1, pp. 824–831, 1992.

[138] H. J. Mamin, H. Birk, P. Wimmer, and D. Rugar, "High-speed scanning tunneling microscopy: Principles and applications," *Journal of Applied Physics*, vol. 75, pp. 161–168, jan 1994.

[139] R. Curtis, T. Mitsui, and E. Ganz, "An ultrahigh vacuum high speed scanning tunneling microscope," *Review of Scientific Instruments*, vol. 68, no. 7, p. 2790, 1997.

[140] C. Y. Nakakura, V. M. Phanse, G. Zheng, G. Bannon, E. I. Altman, and K. P. Lee, "A high-speed variable-temperature ultrahigh vacuum scanning tunneling microscope," *Review of Scientific Instruments*, vol. 69, no. 9, pp. 3251–3258, 1998.

[141] G. Schitter and M. J. Rost, "Scanning probe microscopy at video-rate," *Materials Today*, vol. 11, pp. 40–48, 2008.

[142] A. van Houselt and H. J. W. Zandvliet, “Colloquium: Time-resolved scanning tunneling microscopy,” *Reviews of Modern Physics*, vol. 82, no. 2, pp. 1593–1605, 2010.

[143] M. J. Rost, L. Crama, P. Schakel, E. Van Tol, G. B. E. M. Van Velzen-Williams, C. F. Overgauw, H. Ter Horst, H. Dekker, B. Okhuijsen, M. Seynen, A. Vijftigschild, P. Han, A. J. Katan, K. Schoots, R. Schumm, W. Van Loo, T. H. Oosterkamp, and J. W. M. Frenken, “Scanning probe microscopes go video rate and beyond,” *Review of Scientific Instruments*, vol. 76, no. 5, pp. 1–9, 2005.

[144] F. Besenbacher, F. Jensen, E. Lægsgaard, K. Mortensen, and I. Stensgaard, “Visualization of the dynamics in surface reconstructions,” *Journal of Vacuum Science and Technology B*, vol. 9, no. 2, pp. 874–878, 1991.

[145] T. R. Linderoth, S. Horch, E. Lægsgaard, I. Stensgaard, and F. Besenbacher, “Surface Diffusion of Pt on Pt(110): Arrhenius Behavior of Long Jumps,” *Physical Review Letters*, vol. 78, no. 26, pp. 4978–4981, 1997.

[146] T. R. Linderoth, S. Horch, E. Lægsgaard, I. Stensgaard, and F. Besenbacher, “Dynamics of Pt adatom and dimers on Pt(110)-(1×2) observed directly by STM,” *Surface Science*, vol. 402-404, pp. 308–312, 1998.

[147] T. Linderoth, S. Horch, L. Petersen, S. Helveg, E. Lægsgaard, I. Stensgaard, and F. Besenbacher, “Novel Mechanism for Diffusion of One-Dimensional Clusters: Pt/Pt(110)-(1×2),” *Physical Review Letters*, vol. 82, no. 7, pp. 1494–1497, 1999.

[148] T. Linderoth, S. Horch, L. Petersen, S. Helveg, M. Schønning, E. Lægsgaard, I. Stensgaard, and F. Besenbacher, “Energetics and dynamics of Pt dimers on Pt(110)-(1×2),” *Physical Review B*, vol. 61, no. 4, pp. R2448–R2451, 2000.

[149] L. Petersen, M. Schunack, B. Schaefer, T. R. Linderoth, P. B. Rasmussen, P. T. Sprunger, E. Lægsgaard, I. Stensgaard, and F. Besenbacher, “A fast-scanning, low- and variable-temperature scanning tunneling microscope,” *Review of Scientific Instruments*, vol. 72, no. 2, pp. 1438–1444, 2001.

[150] E. Laegsgaard, L. Österlund, P. Thostrup, P. B. Rasmussen, I. Stensgaard, and F. Besenbacher, “A high-pressure scanning tunneling microscope,” *Review of Scientific Instruments*, vol. 72, no. 9, pp. 3537–3542, 2001.

[151] R. Schaub, E. Wahlström, A. Rønnau, E. Lægsgaard, I. Steensgard, and F. Besenbacher, “Oxygen-Mediated Diffusion of Oxygen Vacancies on the TiO_2(110) Surface,” *Science*, vol. 299, no. 5605, pp. 377–379, 2003.

[152] S. Wendt, R. Schaub, J. Matthiesen, E. Vestergaard, E. Wahlström, M. Rasmussen, P. Thostrup, L. Molina, E. Lægsgaard, I. Stensgaard, B. Hammer,

and F. Besenbacher, “Oxygen vacancies on $TiO_2(110)$ and their interaction with H_2O and O_2: A combined high-resolution STM and DFT study,” *Surface Science*, vol. 598, no. 1-3, pp. 226–245, 2005.

[153] S. Wendt, J. Matthiesen, R. Schaub, E. K. Vestergaard, E. Laegsgaard, F. Besenbacher, and B. Hammer, “Formation and splitting of paired hydroxyl groups on reduced $TiO_2(110)$,” *Physical review letters*, vol. 96, no. 6, p. 066107, 2006.

[154] L. Kuipers, M. S. Hoogeman, and J. W. M. Frenken, “Step dynamics on Au(110) studied with a high-temperature, high-speed scanning tunneling microscope,” *Physical Review Letters*, vol. 71, no. 21, pp. 3517–3520, 1993.

[155] L. Kuipers, M. S. Hoogeman, J. W. M. Frenken, and H. van Beijeren, “Step and kink dynamics on Au(110) and Pb(111) studied with a high-speed STM,” *Physical Review B*, vol. 52, no. 15, pp. 11387–11397, 1995.

[156] L. Kuipers, R. W. M. Loos, H. Neerings, J. ter Horst, G. J. Ruwiel, A. P. de Jongh, and J. W. M. Frenken, “Design and performance of a high-temperature, high-speed scanning tunneling microscope,” *Review of Scientific Instruments*, vol. 66, no. 9, pp. 4557–4565, 1995.

[157] M. Hoogeman, D. Schlößer, J. Sanders, L. Kuipers, and J. Frenken, “Surface energetics and thermal roughening of Ag(115) studied with STM movies,” *Physical Review B*, vol. 53, no. 20, pp. R13299–R13302, 1996.

[158] M. S. Hoogeman, D. G. van Loon, R. W. M. Loos, H. G. Ficke, E. de Haas, J. J. van der Linden, H. Zeijlemaker, L. Kuipers, M. F. Chang, M. A. J. Klik, and J. W. M. Frenken, “Design and performance of a programmable-temperature scanning tunneling microscope,” *Review of Scientific Instruments*, vol. 69, no. 5, pp. 2072–2080, 1998.

[159] R. van Gastel, E. Somfai, W. van Saarloos, and J. Frenken, “A giant atomic slide-puzzle,” *Nature*, vol. 408, no. 6813, pp. 665–665, 2000.

[160] R. Van Gastel, E. Somfai, S. B. Van Albada, W. Van Saarloos, and J. W. M. Frenken, “Nothing moves a surface: Vacancy mediated surface diffusion,” *Physical Review Letters*, vol. 86, no. 8, pp. 1562–1565, 2001.

[161] R. van Gastel, E. Somfai, S. van Albada, W. van Saarloos, and J. Frenken, “Vacancy diffusion in the Cu(001) surface I: an STM study,” *Surface Science*, vol. 521, no. 1, pp. 10–25, 2002.

[162] E. Somfai, R. Van Gastel, S. B. Van Albada, W. Van Saarloos, and J. W. M. Frenken, “Vacancy diffusion in the Cu(001) surface II: Random walk theory,” *Surface Science*, vol. 521, no. 1-2, pp. 26–33, 2002.

[163] R. van Gastel, J. Frenken, B. Swartzentruber, E. Somfai, and W. van Saarloos, “Diffusion of vacancies in metal surfaces: theory and experiment,” in *Chemical Physics of Solid Surfaces*, vol. 11, pp. 351–370, 2003.

[164] R. Van Gastel, M. F. Roşu, M. J. Rost, L. Niesen, and J. W. M. Frenken, “Diffusion and incorporation of a surfactant: In on (vicinal) Cu(001),” *Surface Science*, vol. 555, no. 1-3, pp. 11–19, 2004.

[165] J. Wintterlin, J. Trost, S. Renisch, R. Schuster, T. Zambelli, and G. Ertl, “Real-time STM observations of atomic equilibrium fluctuations in an adsorbate system: O/Ru(0001),” *Surface Science*, vol. 394, no. 1-3, pp. 159–169, 1997.

[166] S. Renisch, R. Schuster, J. Wintterlin, and G. Ertl, “Dynamics of Adatom Motion under the Influence of Mutual Interactions: O/Ru(0001),” *Physical Review Letters*, vol. 82, no. 19, pp. 3839–3842, 1999.

[167] J. Méndez, S. H. Kim, J. Cerdá, J. Wintterlin, and G. Ertl, “Coadsorption phases of CO and oxygen on Pd(111) studied by scanning tunneling microscopy,” *Physical Review B - Condensed Matter and Materials Physics*, vol. 71, no. 8, pp. 1–13, 2005.

[168] M. Vogt, A. Lachenwitzer, O. Magnussen, and R. Behm, “In-situ STM study of the initial stages of corrosion of Cu(100) electrodes in sulfuric and hydrochloric acid solution,” *Surface Science*, vol. 399, no. 1, pp. 49–69, 1998.

[169] O. M. Magnussen, M. Zitzler, B. Gleich, M. Vogt, and R. Behm, “In-situ atomic-scale studies of the mechanisms and dynamics of metal dissolution by high-speed STM,” *Electrochimica Acta*, vol. 46, no. 24-25, pp. 3725–3733, 2001.

[170] O. M. Magnussen, W. Polewska, L. Zitzler, and R. J. Behm, “In situ video-STM studies of dynamic processes at electrochemical interfaces,” *Faraday Discussions*, vol. 121, no. 7, pp. 43–52, 2002.

[171] W. Polewska, R. J. Behm, and O. M. Magnussen, “In-situ video-STM studies of Cu electrodeposition on Cu(100) in HCl solution,” *Electrochimica Acta*, vol. 48, no. 20-22, pp. 2915–2921, 2003.

[172] T. Tansel and O. M. Magnussen, “Video STM studies of adsorbate diffusion at electrochemical interfaces,” *Physical Review Letters*, vol. 96, no. 2, pp. 2–5, 2006.

[173] H. Matsushima, A. Taranovskyy, C. Haak, Y. Gründer, and O. M. Magnussen, “Reconstruction of Cu(100) Electrode Surfaces during Hydrogen Evolution,” *Journal of the American Chemical Society*, vol. 131, no. 30, pp. 10362–10363, 2009.

[174] H. Matsushima, C. Haak, A. Taranovskyy, Y. Gründer, and O. M. Magnussen, “In situ video STM studies of the hydrogen-induced reconstruction of Cu(100): potential and pH dependence,” *Physical Chemistry Chemical Physics*, vol. 12, no. 42, p. 13992, 2010.

[175] Y. C. Yang, A. Taranovskyy, and O. M. Magnussen, “Thiolate-induced metal adatom trapping at solid-liquid interfaces,” *Angewandte Chemie - International Edition*, vol. 51, no. 8, pp. 1966–1969, 2012.

[176] Y. C. Yang, A. Taranovskyy, and O. M. Magnussen, “In situ video-STM studies of methyl thiolate surface dynamics and self-assembly on Cu(100) electrodes,” *Langmuir*, vol. 28, no. 40, pp. 14143–14154, 2012.

[177] Y.-C. Yang and O. M. Magnussen, “Thiolate-induced surface reconstruction of Cu(100) electrodes studied by in situ Video-STM,” *Journal of Electroanalytical Chemistry*, vol. 716, pp. 80–86, 2014.

[178] A. Taranovskyy, T. Tansel, and O. M. Magnussen, “Quantitative measurements of adsorbate-adsorbate interactions at solid-liquid interfaces,” *Physical Review Letters*, vol. 104, no. 10, pp. 1–4, 2010.

[179] T. Tansel, A. Taranovskyy, and O. M. Magnussen, “In situ video-STM studies of adsorbate dynamics at electrochemical interfaces,” *ChemPhysChem*, vol. 11, no. 7, pp. 1438–1445, 2010.

[180] S. Guézo, A. Taranovskyy, H. Matsushima, and O. M. Magnussen, “Surface Dynamics of Lead Adsorbates at the Cu(100)-Electrolyte Interface,” *The Journal of Physical Chemistry C*, vol. 115, no. 39, pp. 19336–19342, 2011.

[181] A. Taranovskyy, S. Guézo, H. Matsushima, Y. Gründer, and O. M. Magnussen, “Studies of electrochemical surface alloying and dealloying by in situ high-speed STM,” *Phys. Chem. Chem. Phys.*, vol. 14, no. 30, pp. 10579–10588, 2012.

[182] M. Labayen, C. Ramirez, W. Schattke, and O. M. Magnussen, “Quasi-collective motion of nanoscale metal strings in metal surfaces,” *Nature Materials*, vol. 2, no. 12, pp. 783–787, 2003.

[183] M. Labayen and O. M. Magnussen, “In situ Video-STM study of the potential-induced (1×1)-"hex" transition on Au(100) electrode surfaces in Cl^- containing solution,” *Surface Science*, vol. 573, no. 1, pp. 128–139, 2004.

[184] M. Labayen, C. Haak, and O. M. Magnussen, “Surface dynamics of nanoscale hex strings on Au(100) electrodes,” *Physical Review B - Condensed Matter and Materials Physics*, vol. 71, no. 24, pp. 1–4, 2005.

[185] Y.-C. Yang, K. Hecker, and O. M. Magnussen, “In situ video-scanning tunneling microscopy studies of the structure and dynamics of Cl adlayers on Au(100) electrodes,” *Electrochimica Acta*, vol. 112, pp. 881–886, 2013.

[186] B. S. Swartzentruber, A. Smith, and H. Jónsson, "Experimental and Theoretical Study of the Rotation of Si Ad-dimers on the Si(100) Surface," *Physical Review Letters*, vol. 77, no. 12, pp. 2518–2521, 1996.

[187] B. S. Swartzentruber, "Atomic-scale dynamics of atoms and dimers on the Si(001) surface," *Surface Science*, vol. 386, no. 1-3, pp. 195–206, 1997.

[188] J. M. Carpinelli and B. S. Swartzentruber, "Detailed energetic interactions of adsorbed Si dimers on Si(001)," *Surface Science*, vol. 411, no. 1-2, pp. L828–L833, 1998.

[189] X. R. Qin, B. S. Swartzentruber, and M. G. Lagally, "Diffusional kinetics of SiGe dimers on Si(100) using atom-tracking scanning tunneling microscopy," *Physical Review Letters*, vol. 85, no. 17, pp. 3660–3663, 2000.

[190] M. L. Grant, B. S. Swartzentruber, N. C. Bartelt, and J. B. Hannon, "Diffusion kinetics in the Pd/Cu(001) surface alloy.," *Physical review letters*, vol. 86, no. 20, pp. 4588–91, 2001.

[191] M. Krueger, B. Borovsky, and E. Ganz, "Diffusion of adsorbed Si dimers on Si(001)," *Surface Science*, vol. 385, no. 1, pp. 146–154, 1997.

[192] E. Hill, B. Freelon, and E. Ganz, "Diffusion of hydrogen on the Si(001) surface investigated by STM atom tracking," *Physical Review B*, vol. 60, no. 23, pp. 15896–15900, 1999.

[193] T. Sato, S.-i. Kitamura, and M. Iwatsuki, "Initial adsorption process of Si atoms on an Si(111)7 × 7 surface studied by scanning tunneling microscopy," *Surface Science*, vol. 445, no. 1, pp. 130–137, 2000.

[194] M. Aketagawa, K. Takada, Y. Minao, Y. Oka, and J.-D. Lee, "Tracking and stepping control of the tip position of a scanning tunneling microscope by referring to atomic points and arrays on a regular crystalline surface," *Review of Scientific Instruments*, vol. 70, no. 4, pp. 2053–2059, 1999.

[195] P. Rerkkumsup, M. Aketagawa, K. Takada, Y. Togawa, N. T. Thinh, and Y. Kozuma, "Highly stable atom-tracking scanning tunneling microscopy," *Review of Scientific Instruments*, vol. 75, no. 4, pp. 1061–1067, 2004.

[196] P. Rahe, J. Schütte, W. Schniederberend, M. Reichling, M. Abe, Y. Sugimoto, and A. Kühnle, "Flexible drift-compensation system for precise 3D force mapping in severe drift environments," *Review of Scientific Instruments*, vol. 82, no. 6, p. 063704, 2011.

[197] C. Africh, L. Köhler, F. Esch, M. Corso, C. Dri, T. Bucko, G. Kresse, and G. Comelli, "Effects of lattice expansion on the reactivity of a one-dimensional oxide," *Journal of the American Chemical Society*, vol. 131, no. 9, pp. 3253–3259, 2009.

[198] L. L. Patera, F. Bianchini, G. Troiano, C. Dri, C. Cepek, M. Peressi, C. Africh, and G. Comelli, "Temperature-driven changes of the graphene edge structure on Ni(111): Substrate vs hydrogen passivation," *Nano Letters*, vol. 15, no. 1, pp. 56–62, 2015.

[199] L. L. Patera, F. Bianchini, C. Africh, C. Dri, G. Soldano, M. M. Mariscal, M. Peressi, and G. Comelli, "Real-time imaging of adatom-promoted graphene growth on nickel," *Science*, vol. 359, no. 6381, pp. 1243–1246, 2018.

[200] A. Savitzky and M. J. E. Golay, "Smoothing and Differentiation of Data by Simplified Least Squares Procedures.," *Analytical Chemistry*, vol. 36, no. 8, pp. 1627–1639, 1964.

[201] H. P. Koch, R. Laskowski, P. Blaha, and K. Schwarz, "Adsorption of gold atoms on the h-BN/Rh(111) nanomesh," *Physical Review B*, vol. 84, no. 24, p. 245410, 2011.

[202] M. Iannuzzi, F. Tran, R. Widmer, T. Dienel, K. Radican, Y. Ding, J. Hutter, and O. Gröning, "Site-selective adsorption of phthalocyanine on h-BN/Rh(111) nanomesh," *Phys. Chem. Chem. Phys.*, vol. 16, no. 24, pp. 12374–12384, 2014.

[203] H. P. Koch, R. Laskowski, P. Blaha, and K. Schwarz, "Adsorption of small gold clusters on the h-BN/Rh(111) nanomesh," *Physical Review B*, vol. 86, no. 15, p. 155404, 2012.

[204] S. J. Carroll, S. Pratontep, M. Streun, R. E. Palmer, S. Hobday, and R. Smith, "Pinning of size-selected Ag clusters on graphite surfaces," *Journal of Chemical Physics*, vol. 113, no. 18, pp. 7723–7727, 2000.

[205] S. J. Carroll, P. D. Nellist, R. E. Palmer, S. Hobday, and R. Smith, "Shallow Implantation of "Size-Selected" Ag Clusters into Graphite," *Physical Review Letters*, vol. 84, no. 12, pp. 2654–2657, 2000.